UNIVERSITY OF CALIFORNIA
SANTA CRUZ

BASAL SEISMICITY OF THE WHILLANS ICE PLAIN, WEST ANTARCTICA: INSIGHTS INTO MULTI-SCALE BASAL HETEROGENEITY, STICK-SLIP SLIDING, AND ICE STREAM BASAL PROCESSES

A dissertation submitted in partial satisfaction
of the requirements for the degree of

DOCTOR OF PHILOSOPHY

in

EARTH SCIENCES

by

Catherine Grace Barcheck

December 2018

This Dissertation of Catherine Grace Barcheck is approved:

_____
Professor Susan Y. Schwartz, chair

_____
Professor Slawek Tulaczyk

_____
Professor Thorne Lay

_____
Lori Kletzer
Vice Provost and Dean of Graduate Studies

Table of Contents

List of Figures

List of Tables

Abstract

Basal seismicity of the Whillans Ice Plain, West Antarctica: Insights into multi-scale basal heterogeneity, stick-slip sliding, and ice stream basal processes

by

Catherine Grace Barcheck

Conditions at the base of an ice stream control the ability of basal material to resist ice sliding, which affects ice stream mass balance. Yet, basal properties are notoriously hard to constrain. Tiny magnitude ~-2 to -1 stick-slip basal icequakes occurring near or on the basal sliding surface hold valuable information about this basal environment. In this dissertation, I investigate spatiotemporal patterns in these basal icequakes occurring beneath the Whillans Ice Plain (WIP), in West Antarctica, and interpret these patterns to gain insight into basal material heterogeneity and temporally evolving basal conditions.

In Chapter 2, I determine where basal icequakes happen beneath the entire WIP. I find spatially variable seismicity rates, with basal seismicity most common in a ~40 km wide area surrounding a dynamically important region where ice-plain-wide unstable slip nucleates. This result implicates icequake-generating bed conditions in large-scale ice stream stick-slip. Additionally, I propose that basal icequakes occur where basal erosion exposes over-consolidated till to the ice base.

In Chapter 3, I use back-projection to detect basal icequakes beneath a small seismic network near the nucleation region. Here, basal icequakes occur in streaks elongated along ice flow and in conjunction with low-amplitude (~2m) undulating basal topography. These patterns suggest the presence of mega-scale glacial lineations (MSGL), elongate bedforms common on paleo-ice stream beds. One icequake streak may occur in a shallow trough beside an MSGL, suggesting that these

icequakes occur in erosion-impacted lows between MSGL where over-consolidated till or stiff sediment outcrops contact the ice base.

In Chapter 4, I analyze an improved basal icequake catalog generated by cross correlating icequakes detected in Chapter 3. I estimate icequake moment magnitudes of M_w = -2.1 to -1.2 and fault rupture areas of 1-100 m^2 for several large basal icequakes. Families of nearly-identical repeating basal icequakes continue for ice sliding distances of typically <0.5 m, and most <0.2 m. If this distance also represents the approximate size of an icequake-generating fault, then basal icequake faults have dimensions of cm to m. I explore evidence for ice-bed interface healing between unstable slip events. Lastly, I discuss four possible mechanisms for basal seismicity.

To my parents, Alison and Rick, who taught me to see the world around me and be curious.

Acknowledgments

So many people deserve thanks for helping me succeed during graduate school. Completing this Ph.D. has been a challenging and rewarding interdisciplinary adventure, because I chose to interweave two rarely-overlapping yet highly synergistic fields of Earth sciences: glaciology and seismology. This dissertation would not exist without the collaborative spirit of my two co-advisors, Susan Schwartz and Slawek Tulaczyk. A seismologist and a glaciologist, together they were early believers in the using the power of seismology as a tool for studying the cryosphere, and they have dedicated many years to helping me figure out how to do just that. Thank you for all of your feedback and help over the years, for your enthusiasm and support, and for helping me become fluent in the languages of two different fields of study. Thank you also to Thorne Lay, the final member of my dissertation reading committee, for your useful feedback over the years and for your excellent explanations of so many interesting great earthquakes during seismo coffee. And thank you to Emily Brodsky, for always being interested to talk about icequakes large and small, and for many good conversations.

Thanks especially to my parents: to my mother, who has always believed I could do anything I set my mind to, and to my father, who taught me to design and think through process, to anticipate problems well in advance, and to see the big picture. Many thanks also to Patrick Fulton, who has been a foundational support for me, both personally and scientifically, over these graduate school years.

Thank you to Doug Wiens, who sent me to Antarctica for the first time and encouraged my curiosity about all those weird seismic signals in Antarctica. Thank you for all the opportunities you gave me.

A huge number of people deserve thanks for their contributions to the Antarctic field work component of this dissertation. I am especially grateful to Dan

Sampson, Esteban Chaves, Sarah Neuhaus, and Marino Protti, who were absolutely critical to successful collection of the seismic data. Also a big thank you for fieldwork assistance goes to Marci Beitch, Matt Siegfried, Neil Foley, Carolyn Begeman, Brad Lipovsky, Doug Bloomquist, Ken Mankoff, Slawek Tulaczyk, Susan Schwartz, and the entire WISSARD science and logistical support team. A big thanks to PASSCAL and UNAVCO for providing seismic and GPS instrumentation and support, and to the University of Nebraska, Lincoln hot water drilling group. Thanks for logistical support goes to Julie Raine, the Antarctic Support Contract, the US Antarctic Program, Kenn Borek Air, and the New York Air National Guard, and surely others I have failed to remember.

Thank you also to Jake Walter, who placed the first seismometer in 2010 at site S08, which turned out to be fantastically seismically active. Chapters 3 and 4 showcase seismic data collected at the same location several years later and would not have been possible without this serendipitous choice.

Thanks to Jake Walter and also co-author Paul Winberry for generously sharing seismic and GPS data that formed the basis of Chapter 2, and for helpful feedback on that manuscript.

To the undergraduate students I have worked with at UCSC, thank you for all your hard work and for letting me be a part of your time at UC Santa Cruz: Krista Meyers, Chloe Boucher, Matt Williams, Tyler Paladino. I can't wait to see what you do next.

The graduate student community at UCSC has been a vital part of my time in graduate school. I will always be grateful to the cohort of graduate students I began graduate school with; over the years we have all driven each other to be better scientists and better people, and I look forward to hearing about your future successes. A sincere thank you goes to all the GEODES leaders I have

worked with over the years. The thoughtfulness and dedication of each and every one of you is truly inspiring, and I'm perpetually amazed by what GEODES has accomplished. To all the members of my two lab groups over the years, both the polar scientists and the seismologists, thank you for providing a supportive environment in which to ask dumb questions and get excited about the answers. And thanks to all my dear dear friends in Santa Cruz. Your friendship throughout grad school has been so important.

Finally, I would like to acknowledge the generosity of my funding sources for graduate school: The National Science Foundation, the ARCS Foundation, ExxonMobil, SigmaXi, the UCSC Environmental Studies department, and the UCSC Division of Physical and Biological Sciences.

The text of this dissertation includes the following previously published material:

> Barcheck, C.G., Tulaczyk, S., Schwartz, S.Y., Walter, J.I., and Winberry, J.P., 2018, Implications of basal micro-earthquakes and tremor for ice stream mechanics: Stick-slip basal sliding and till erosion: Earth and Planetary Science Letters, v. 486, p. 54-60, doi: 10.1016/j.epsl.2017.12.046.

(Chapter 2, herein; Appendix A, herein)

Additionally, the content of Chapter 3 has been revised, shortened, and submitted to Geology. Susan Schwartz and Slawek Tulaczyk are co-authors. As of submission of this dissertation, this material is in review.

Chapter 1

Introduction: Whillans Ice Plain stick-slip and basal seismicity

Ice streams are the fast-flowing (0.1-1 km/year) ice drainages that move ice from the thick ice sheet interior towards the ice sheet edges and the ocean. Fast flowing ice streams are the main conduits by which ice moves from the interior of an ice sheet across the grounding line, where it contributes to sea level (*Bennett*, 2003). Understanding the physical processes that enable this fast ice flow is critical for accurate predictive modeling of ice sheet evolution and resulting sea-level change in the near future, a pursuit that is highly societally relevant.

Ice streams are driven by gravity, with the driving stress proportional to the slope of the ice surface (*Cuffey and Paterson*, 2010). The ice responds to this driving stress with both internal viscous deformation of the ice and sliding of the ice atop its substrate, or "bed". Internal deformation is resisted by the viscosity of the ice, and basal sliding is resisted by both the mechanical properties and the roughness of the ice stream bed. This dissertation is focused on constraining controls on the sliding component of ice stream movement using the unique tool of glacial seismology.

The conditions at the base of ice streams control the extent to which the basal material can resist ice sliding, which in turn impacts ice stream flow velocity and ice discharge rates into the ocean. Ice stream beds are thought to be a generally weak mosaic of lubricating subglacial water and soft, deformable till, with an outsized amount of basal resistance contributed by localized "sticky spots" (*Alley*, 1993; *Stokes et al.*, 2007). The spatial and temporal scales at which basal material heterogeneity, thermal conditions, hydrology, geomorphology, and resulting basal traction (resistance to ice sliding) vary beneath ice streams is largely unresolved due to difficult access and lack of observational methods sensitive to basal properties at necessary spatial scales. The impact of meter- to km-scale basal heterogeneity on ice stream sliding and large-scale flow dynamics is unknown, though it is reasonable to assume that ice streams with low driving stress and weak beds may be highly sensitive to small local changes in basal conditions and resistance. Understanding the scale and causes of basal heterogeneity and basal traction is also critical for extrapolating basal conditions observed by borehole point measurements to a larger ice stream area.

In this dissertation, I use observations of small seismic events at the base of the Whillans Ice Stream, in West Antarctica, to learn about the conditions at the ice base and the scales at which basal conditions vary. Basal icequakes (Figure 1.1) are small seismic events happening at or near the interface between ice and bed. The mechanical cause of these small seismic signals is generally unknown, though they are usually generated by shear dislocation across an interface, like typical tectonic earthquakes. Focal mechanisms of basal icequakes typically show double-couple slip sub-parallel to the ice base (*Anandakrishnan and Alley*, 1994; *Anandakrishnan and Bentley*, 1993; *Blankenship et al.*, 1987; *Roeoesli et al.*, 2016; *Smith et al.*, 2015; *Zoet et al.*, 2012), indicating that ice stream basal sliding

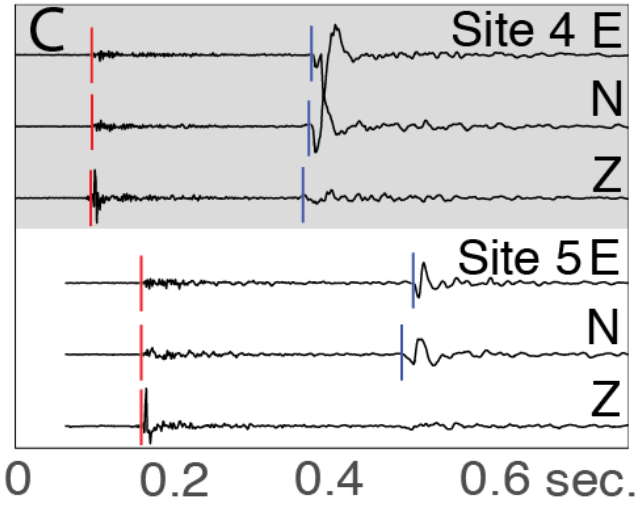

Figure 1.1: Example seismograms of a basal icequake from the Whillans Ice Plain recorded at two proximal seismometers, <750 m apart. Sampling rate is 1000 Hz, and data are high-pass filtered above 1 Hz. Red vertical lines indicate P-wave arrivals, and blue vertical lines indicate S-wave arrivals. Note shear-wave splitting evident at Site 5.

includes some component of stick-slip over brittle materials, even in areas of fast-moving ice thought to be underlain by soft, deformable till.

These small earthquakes occurring on or near the sliding interface of ice streams hold information about the environment in which they occur and are a valuable high temporal and spatial resolution method for analyzing heterogeneous basal conditions. For example, icequake-generating material must be velocity-weakening (*Lipovsky and Dunham*, 2016), and basal icequake behavior has been related to spatial variation in till mechanical properties (*Smith*, 2006; *Smith et al.*, 2015), temporal variation in subglacial water pressure (*Roeoesli et al.*, 2016), and basal erosion (*Zoet et al.*, 2013a). The first observations of icequakes beneath large Antarctic ice streams date from the 1980s, when a specially designed seismic network captured seismic waves from a handful of small icequakes ocurring near the base of the Whillans Ice Stream (WIS) (*Blankenship et al.*, 1987). Sev-

eral subsequent experiments recorded similar basal events beneath other portions of the WIS and nearby Kamb Ice Stream (KIS) (*Anandakrishnan and Bentley*, 1993; *Anandakrishnan and Alley*, 1994, 1997a), and beneath Rutford Ice Stream (*Smith*, 2006; *Adalgeirsdottir et al.*, 2008; *Smith et al.*, 2015). Basal icequakes have also been used to observe the propagation of tidal stresses upstream (*Anandakrishnan and Alley*, 1997b; *Adalgeirsdottir et al.*, 2008) and to measure shear wave anisotropy in ice streams (*Harland et al.*, 2013; *Smith et al.*, 2017). Many additional passive seismic experiments have been performed on alpine glaciers, but are not summarized here.

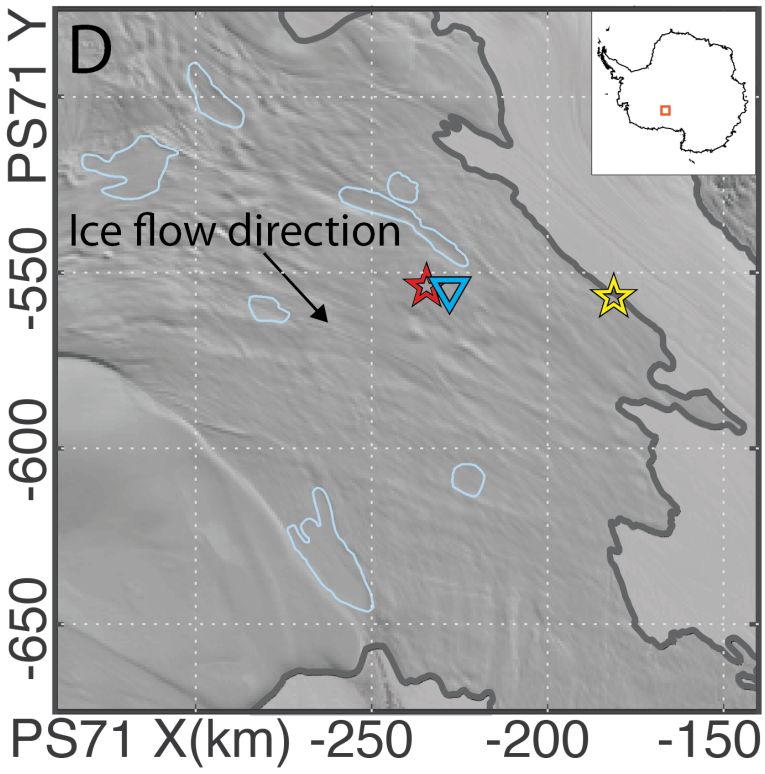

Figure 1.2: The Whillans Ice Plain. Location of seismic network discussed in Chapters 3 and 4 shown by blue triangle. Unstable slip nucleation areas are shown by red and yellow stars (*Pratt et al.*, 2014). Thick grey line is the grounding line from *Bindschadler et al.* (2011). Light blue outlines show subglacial lakes from *Fricker and Scambos* (2009).

This dissertation adds to the growing field of glacial seismology, and I use basal seismicity to paint a clearer picture of the basal slip interface of the Whillans Ice Plain (WIP), in West Antarctica (Figure 1.2). I study the details of spatial and temporal basal icequake patterns beneath the WIP to gain new insight into the ice stream basal environment. I am especially interested in the spatially heterogeneous nature of the ice stream basal boundary conditions at regional (10s of km) and local (< km) scales, and the relationship of that heterogeneity to the large-scale ice stream dynamics. In this dissertation, I combine observations of basal seismicity with the more common glaciological observational tools of on-ice GPS and ice-penetrating radar to create a refined picture of the WIP ice stream bed.

The Whillans Ice Plain (Figure 1.2) is a valuable location to study basal seismicity, heterogeneous local basal conditions, and effects on ice dynamics. The WIP is the wide, flat, lower portion of the Whillans Ice Stream, where it exits the narrow upper Whillans Ice Stream, merges with neighboring Mercer Ice Stream to the south, and forms a broad, flat "ice plain". The WIP has a very low surface slope ($\sim 0.4 \times 10^{-3}$) and consequently very low driving stresses of a few kPa (*Bindschadler et al.*, 1987). Its relatively fast motion (~270 m/yr in 2014 near the blue triangle in Figure 1.2) is therefore permitted by extremely low basal resistance resulting from sliding over a saturated layer of deformable till (*Alley et al.*, 1986; *Blankenship et al.*, 1986; *Luthra et al.*, 2016). A large area of the greater Whillans Ice Stream (WIS) has been slowing down since at least the mid-1980s (*Whillans et al.*, 2001; *Joughin et al.*, 2002, 2005; *Bindschadler et al.*, 2005; *Beem et al.*, 2014), making it an especially interesting area to investigate changes in basal conditions and any impact on ice flow. The lower reaches of neighboring Kamb Ice Stream (KIS) stagnated completely approximately 150 years ago (*Retzlaff and*

Bentley, 1993). Interestingly, the stagnant portions of KIS feature abundant basal seismicity, while the upper actively sliding reaches of both KIS and WIS are nearly aseismic (*Anandakrishnan and Alley*, 1997a). This suggests that basal seismicity may be a feature of stagnant or near-stagnant ice streams.

In addition to being one of the few decelerating Antarctic ice streams, the WIP is also known for its unique stick-slip style of motion (*Bindschadler et al.*, 2003): Instead of steady ice sliding, as is observed on other ice streams, the WIP is largely unmoving or sliding at very low velocities of several m/year. Once or twice a day, however, the ice suddenly accelerates over several minutes to speeds of 10,000-20,000 m/year, and then slows back down to velocities of several m/year over approximately 30 minutes (*Bindschadler et al.*, 2003). This entire process results in sliding of ~0.5m. These "unstable slip events" happen once or twice a day (Figure 1.3), though the frequency of events has been decreasing since they were first observed (*Winberry et al.*, 2014; *Siegfried et al.*, 2016). The unstable slip timing is strongly modulated by the tidal height beneath the adjacent and downstream Ross Ice Shelf (e.g. *Bindschadler et al.*, 2003; *Winberry et al.*, 2009b). Acceleration during slip is fast enough in some areas of the WIP to generate long period seismic energy recorded up to 1000km away (*Wiens et al.*, 2008; *Walter et al.*, 2011; *Pratt et al.*, 2014), and the total moment of an unstable slip event is equivalent to a Mw ~7 earthquake (*Wiens et al.*, 2008), though with a very long (30 minutes) source duration. WIP unstable slips are analogous to slow slips on a low-angle normal fault system, making them the most repeatable and easily observed large fault failure anywhere on Earth.

Additionally, the 'nucleation area' of the slip events–the portion of the ice plain that first accelerates unstably during a slip event–has been constrained by looking at the timing of slip acceleration using on-ice broadband seismic and

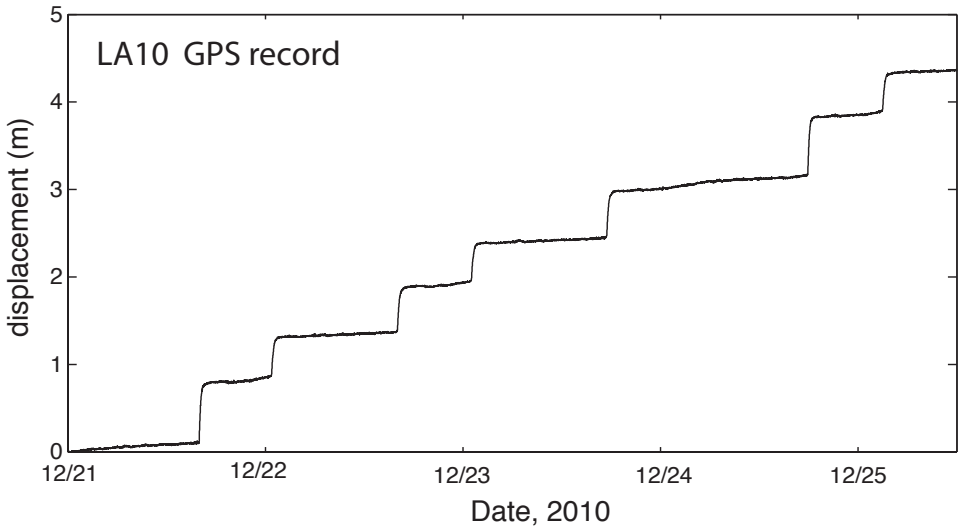

Figure 1.3: GPS displacement record from Lake 10 showing stick-slip motion.

GPS instruments (*Pratt et al.*, 2014). Depending on tidal height, the slip events nucleate either in the center of the ice plain, termed the "Central nucleation area" (*Barcheck et al.*, 2018) or "Central Sticky Spot" (*Winberry et al.*, 2014), or near the grounding zone to the south, termed the "grounding zone nucleation area" (red and yellow stars, Figure 1.2) (*Pratt et al.*, 2014; *Winberry et al.*, 2014). This previous work has shown the WIP unstable slip cycle to be complex, with multiple locations of unstable slip nucleation and a complicated relationship to the tidal amplitude beneath the downstream Ross Ice Shelf.

These investigations of the Whillans Ice Plain stick-slip cycle were largely completed using several remarkably widespread networks of broadband seismometers and GPS installed on the WIP in 2010-2011 (*Walter et al.*, 2011; *Winberry et al.*, 2011, 2014; *Pratt et al.*, 2014; *Walter et al.*, 2015). These experiments used broadband seismic and GPS observations to constrain the timing of unstable slip onset to determine where and how unstable slip begins. Fortunately, these seismic networks were recording at relatively high sample rates of 200-500 Hz, and some of

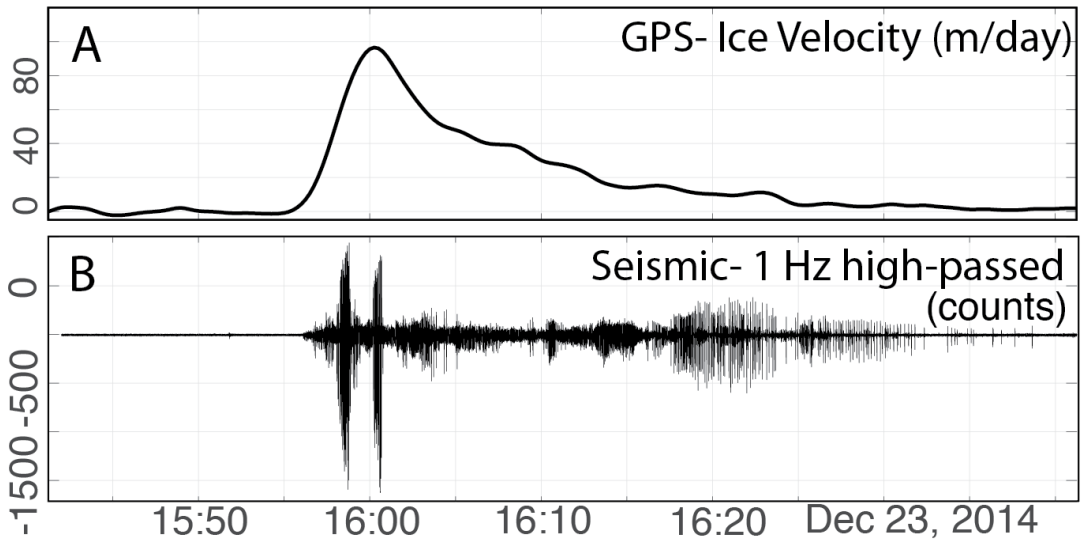

Figure 1.4: A: GPS velocity at the small seismic network discussed in Chapters 3 and 4. GPS displacement has been lowpass filtered below 300 seconds and differentiated to velocity. Sampling interval is 15 seconds. Units are m/day. B: High frequency seismicity recorded by the small seismic network during the unstable slip event shown in A. Seismic data are high pass filtered above 1 Hz. Each spike corresponds to an individual basal icequake, similar to what is shown in Figure 1.

the broadband seismic sites also recorded abundant high-frequency, low-amplitude local basal seismicity: Repeating basal icequakes with clear P and S waves were found during unstable slip events in addition to basal seismic "tremor", interpreted as basal icequakes repeating closely in time (*Winberry et al.*, 2013; *Lipovsky and Dunham*, 2016). However, where and how often these basal seismic signals occur beneath the WIP was not systematically quantified prior to this dissertation.

This dissertation builds on these previous investigations of the WIP large-scale stick-slip cycle and basal micro-seismicity. I further constrain basal micro-seismic behavior in both previously and newly collected data from the Whillans Ice Plain, and I use these results to reveal spatially and temporally variable WIP basal conditions and heterogeneity in ice stream basal material properties.

In Chapter 2, I dive into the large previously collected dataset of broadband seismic and GPS data (*Walter et al.*, 2011; *Winberry et al.*, 2011, 2014; *Pratt et al.*, 2014; *Walter et al.*, 2015), to investigate the ice-plain-wide patterns in basal micro-seismicity and explore the relationship of basal seismicity and tremor to the patterns of strain accumulation between unstable slip events. I find that a region surrounding the central nucleation area has the most basal icequake activity, though rates are highly heterogeneous, with seismometers < 5 km apart observing very different seismicity rates. Basal seismicity also transitions from discrete icequakes near the central nucleation area to basal tremor downstream. I use these patterns to infer regionally variable subglacial till properties, with more basal seismicity where larger areas of over-consolidated till outcrop to the ice base. This chapter explores broad patterns in basal heterogeneity shown by basal seismicity, at the ice-plain-wide scale of 10s of km. This work is summarized in *Barcheck et al.* (2018).

In Chapter 3, I zoom into a small seismic network installed at one of the most seismically active sites from Chapter 2. This small network was installed in austral summer 2012-13 as part of the Whillans Ice Stream Subglacial Access Research Drilling (WISSARD) project, and borehole seismometers were added in 2013-14. This chapter analyzes seismicity recorded during two consecutive austral summers: 2013-14 and 2014-15. Here, I explore spatial patterns in basal seismicity beneath this small seismic network and compare these patterns with inferred geomorphology beneath the ice. I develop an S-wave backprojection method to detect and locate basal icequakes during several weeks in each austral summer, revealing several prominent streaks of basal icequakes elongated in the ice flow direction. These streaks have comparable spacing and elongation to mega-scale glacial lineations (MSGL) found on paleo-ice-stream beds (*Spagnolo et al.*, 2014)

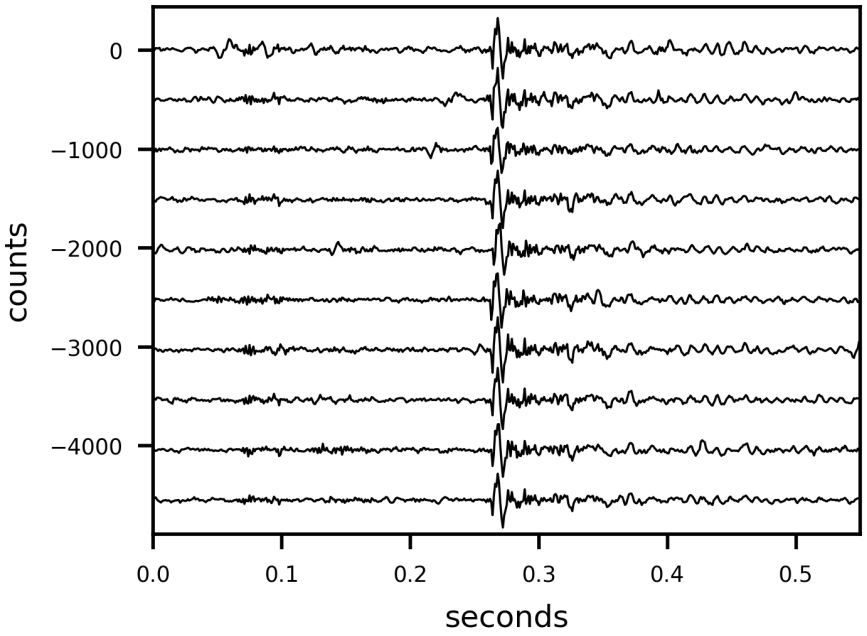

Figure 1.5: Seismograms from ten consecutive basal icequakes, aligned by cross correlation, and showing remarkable waveform similarity in repeats.

and beneath at least one active ice stream (*Smith*, 1997; *Smith and Murray*, 2009; *King et al.*, 2009). Evidence of MSGLs beneath my seismic network comes from a single available ice-penetrating radar line, which shows a low-amplitude, gently undulating bed superposed on a shallow regional slope. I again suggest that WIP basal icequakes happen where over-consolidated till or stiff sediment outcrops to the ice base, in this case in erosion-impacted troughs between MSGL.

Finally, Chapter 4 explores an improved catalog of WIP basal icequakes generated from the backprojection catalog from 2014-15. I use cross-correlation to refine the catalog and detect smaller basal icequake repeats. This catalog contains the most well-recorded "families" of nearly identical repeating basal icequakes. I look at temporal patterns in basal seismicity for the whole dataset, within each unstable slip event, and within individual families of repeating basal icequakes. I estimate the seismic moment, moment magnitude, rupture area, and stress drop

from the P waves of several of the largest and most well-recorded icequakes in the dataset, finding moment magnitudes in the -2 to -1 range and icequake fault rupture areas of ~1 – 100 m^2. I also quantify the amount of slip over which a family of nearly identical repeating icequakes (Figure 1.5) occurs as a metric of either an icequake patch dimension or an icequake patch evolution distance. Icequake families last for ice slip distances of typically less than 0.5 m, and most less than 0.2 m. An approximately exponentially decreasing trend in the number of families that occur over an increasing ice displacement suggests that there may also be an exponential distribution of icequake patch sizes at the ice base. I interpret these length scales as either the smallest scale of basal heterogeneity we can observe from the ice surface (~0.005 m), or a slip evolution distance. I explore evidence for healing of the ice-bed interface between unstable slip events. And lastly, I identify four potential mechanisms for basal seismicity. This chapter explores the smallest scale of bed heterogeneity that can be observed with basal seismicity, ~0.005-10 m.

Together, these studies investigate basal seismicity and bed conditions of the Whillans Ice Plain at a wide range of scales, from cm to 10s of km. I explore the implications of this seismicity for understanding conditions at the base of the ice, especially material heterogeneity, and the scales of heterogeneous basal conditions.

Chapter 2

Implications of basal micro-earthquakes and tremor for ice stream mechanics: Stick-slip basal sliding and till erosion

2.1 Abstract

The Whillans Ice Plain (WIP) is unique among Antarctic ice streams because it moves by stick-slip. The conditions allowing stick-slip and its importance in controlling ice dynamics remain uncertain. Local basal seismicity previously observed during unstable slip is a clue to the mechanism of ice stream stick-slip and a window into current basal conditions, but the spatial extent and importance of this basal seismicity are unknown. We analyze data from a 2010-11 ice-plain-wide seismic and GPS network to show that basal micro-seismicity correlates with large-scale patterns in ice stream slip behavior: Basal seismicity is common where

the ice moves the least between unstable slip events, with small discrete basal micro-earthquakes happening within 10s of km of the central stick-slip nucleation area and emergent basal tremor occuring downstream of this area. Basal seismicity is largely absent in surrounding areas, where inter-slip creep rates are high. The large seismically active area suggests that a frictional sliding law that can accommodate stick-slip may be appropriate for ice stream beds on regional scales. Variability in seismic behavior over inter-station distances of 1-10 km indicates heterogeneity in local bed conditions and frictional complexity. WIP unstable slips may nucleate when stick-slip basal earthquake patches fail over a large area. We present a conceptual model in which basal seismicity results from slip-weakening frictional failure of over-consolidated till as it is eroded and mobilized into deforming till.

2.2 Introduction

Basal conditions that promote or prevent fast ice stream flow are important for determining future stability of the West Antarctic Ice Sheet (e.g. *Bennett*, 2003). The largely unmapped basal interface of the ice streams that drain the West Antarctic Ice Sheet may be variably resistant, and the extent to which ice sheet models need to account for this complexity is largely unknown. Part of the reason for the lack in understanding of ice stream basal sliding behavior is the difficulty of accessing or imaging the ice base. Increasingly, however, seismicity from the bed of fast-moving glaciers and ice streams is used to inform our understanding of bed conditions and processes that control fast ice flow (*Anandakrishnan and Alley*, 1994; *Blankenship et al.*, 1987; *Podolskiy and Walter*, 2016; *Roeoesli et al.*, 2016; *Smith*, 2006; *Smith et al.*, 2015) and that affect ice stream contribution to sea-level rise.

Some basal micro-earthquakes near the bottom of ice streams and glaciers occur as double-couple slip between two elastic surfaces in the ice, till, or bedrock (*Anandakrishnan and Alley*, 1994; *Anandakrishnan and Bentley*, 1993; *Blankenship et al.*, 1987; *Roeoesli et al.*, 2016; *Smith et al.*, 2015; *Zoet et al.*, 2012). Fundamental controls on the timing, size, and frequency of occurrence of these basal micro-earthquakes remain largely unresolved, and their relevance for broader ice stream dynamics is unknown. Basal micro-earthquakes are common beneath the slow-moving, shutdown portion of the Kamb Ice Stream (KIS), but rare beneath fast-flowing, upstream KIS (*Anandakrishnan and Alley*, 1997a), suggesting a relationship between presence or absence of basal seismicity and ice stream flow regime (stagnant vs. streaming, respectively). Beneath Rutford Ice Stream, areas of the bed with lodged till (embedded in the substrate), as inferred by measurements of seismic impedance (*Smith*, 1997), have more basal micro-earthquakes than areas of the bed inferred to be actively deforming (*Smith*, 2006; *Smith et al.*, 2015). These inferences suggest that basal micro-earthquakes may indicate variation in certain bed conditions, for example till properties, that may impact flow velocity. Passive seismic observation of basal micro-earthquakes is therefore a useful technique to infer the spatial and temporal variability of basal conditions and, by extension, basal resistance to fast flow.

The Whillans Ice Plain (WIP), in West Antarctica, is an excellent area to investigate basal seismicity because seismic and GPS data have been collected over the last decade at numerous sites on the ice plain to study its stick-slip cycle (*Bindschadler et al.*, 2003; *Pratt et al.*, 2014; *Siegfried et al.*, 2016; *Walter et al.*, 2015, 2011; *Winberry et al.*, 2014, 2013, 2011, 2009b), its basal hydrologic cycle (e.g. *Fricker and Scambos*, 2009; *Siegfried et al.*, 2016), and its long-term slowdown and basal strengthening (*Joughin et al.*, 2005; *Beem et al.*, 2014). Typical

stable sliding of the WIP is punctuated once or twice daily by sudden unstable sliding events (accelerations) lasting 20-30 minutes and displacing the ice 10s of cm (*Bindschadler et al.*, 2003). Unstable slip events nucleate at one of two areas of the WIP, typically but not always depending on Ross Ice Shelf tidal height: the central nucleation area at high tide, or the grounding zone nucleation area at low tide (shown in Figure 2.2) (*Pratt et al.*, 2014; *Walter et al.*, 2015). The central nucleation area is thought to be underlain by low-porosity, but deforming, till (*Luthra et al.*, 2016). The current slowdown and positive mass balance of the Whillans Ice Stream is modulated by changes in the frequency of stick-slip events (*Winberry et al.*, 2014).

Basal micro-earthquakes beneath the WIP were previously observed as rapidly repeating nearly identical events during unstable slip events (*Winberry et al.*, 2013), but the spatial extent of basal seismicity is unknown. The earthquakes likely occur within the till or at the ice-till interface, with the preferred plane of rupture sub-parallel to the ice base (*Anandakrishnan and Bentley*, 1993; *Blankenship et al.*, 1987; *Roeoesli et al.*, 2016; *Smith*, 2006; *Smith et al.*, 2015). Basal ice may contain significant concentration of debris (*Kamb*, 2001) and may be locally exposed to sub-till sediment or bedrock material (*Rooney et al.*, 1987), both of which may affect basal sliding. If basal micro-earthquakes involve till or other sediments, then the mechanical behavior of the till or sediment is critically important in the basal micro-earthquake mechanism. Lower porosity till is stronger in shear (*Tulaczyk et al.*, 2000) and may be more likely to exhibit basal seismicity than deforming and high-porosity till that likely deforms aseismically (*Smith*, 2006, 1997; *Smith et al.*, 2015).

In this paper, we identify areas of the WIP that exhibit basal seismicity by analyzing several seismic datasets recorded during 2010-11 and originally used

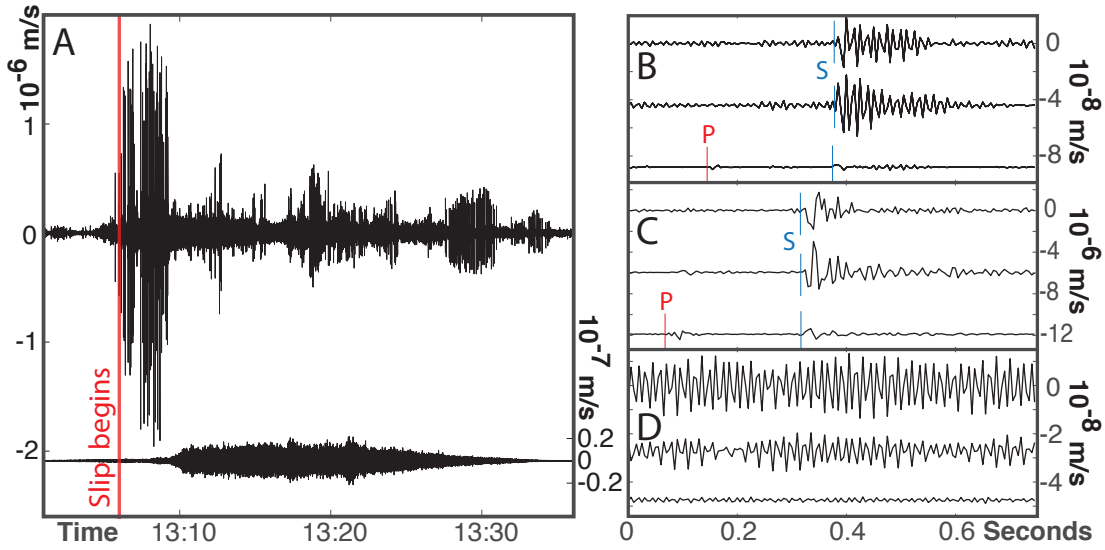

Figure 2.1: Example basal earthquake and tremor seismic data. A: Sample east component seismic records of individual basal micro-earthquakes (top) and basal tremor (bottom) at two different sites during the same slip event that begins at the red line. Note the different vertical scales. Slip time is from (*Pratt et al.*, 2014). B-C: Example basal micro-earthquakes from two different stations. Channels from top to bottom are E, N, Z. P and S waves are labeled. D: Basal tremor for same amount of time. Tremor seismicity is continuous instead of discrete basal micro-earthquakes. Basal micro-earthquakes are identified by a characteristic P and S wave shape, while tremor is identified as spectral gliding lines. (see Figure A.1)

to identify the stick-slip nucleation areas (*Walter et al.*, 2011, 2015; *Winberry et al.*, 2014; *Pratt et al.*, 2014). Basal seismicity (Figure 2.1) includes both individual basal micro-earthquakes (e.g. *Blankenship et al.*, 1987; *Anandakrishnan and Bentley*, 1993; *Smith*, 2006; *Winberry et al.*, 2013; *Smith et al.*, 2015) and basal tremor, which has been modeled as a seismic signal composed of interfering basal micro-earthquakes (*Lipovsky and Dunham*, 2016; *Winberry et al.*, 2013). We compare the spatial distribution of basal seismicity from these datasets to the locations where unstable sliding nucleates during the Whillans Ice Plain stick-slip cycle (stars in Figure 2.2 from *Pratt et al.* (2014)). We also compare basal seismicity locations with GPS-derived patterns of ice stream slip during and between

WIP unstable sliding events.

2.3 Data and methods: Seismic and GPS data

To assess where basal seismicity happens beneath the WIP, broadband seismic data from 55 locations were analyzed visually for presence of basal micro-earthquakes and tremor (Figure 2.1) during unstable slips in 2010-11. Data was collected during three separate deployments of seismometers and GPS, and between 25 and 79 slip events were analyzed for each seismic site depending on deployment length. Our analysis does not discriminate between high and low tide unstable slip events. Additional network details can be found in Supplementary Table A.1. Basal micro-earthquakes during unstable slip are visually identified as short-lived repeating seismic events with a distinct characteristic wave shape: P energy primarily on the vertical component, S energy mostly on the horizontal component, and lack of surface wave energy (Figure 2.1B, 2.1C). S minus P intervals of ~0.18-0.4 seconds indicate a hypocentral distance of 650-1440m (V_p=3840 m/s; V_s=1860 m/s (*Luthra et al.*, 2016)), consistent with near-nadir origins at the base of 650-800 m thick ice (*Fretwell et al.*, 2013). In contrast, crevasse-forming events have surface wave energy and a different waveshape and are ignored. Individual basal micro-earthquakes rarely show up at two neighboring seismometers in this dataset, meaning the sources are small and the seismic waves attenuate within a few km. If there are more than ~10 characteristic repeating basal micro-earthquakes during an unstable slip event, that event is marked as having basal micro-seismicity, though some seismic sites show 1000s of basal micro-earthquakes during a single unstable slip. Basal tremor is identified visually as gliding lines in east component spectrograms of seismic data during unstable slip events (e.g., Supplementary Figure A.1; (*Lipovsky and Dunham*, 2016)). Gliding lines occur

when the seismic signal recorded during basal tremor (Figure 2.1D) has a preferred frequency that changes with variations in ice sliding velocity, as shown in Supplementary Figure A.1. These gliding lines are interpreted as the spectral signal of repeating basal micro-earthquakes overlapping in time such that the number of earthquake S-wave arrivals per second becomes the frequency of the recorded seismic signal (*Lipovsky and Dunham*, 2016). Seismicity results are summarized in Figure 2.2A.

WIP downstream motion is partitioned into unstable sliding (resulting from acceleration during a slip event) and stable sliding (observed at the surface as "creep" between slip events) in varying amounts across the ice plain. Some sites stagnate between unstable slips and accrue a "slip deficit" relative to nearby sites that continue to creep. This variability is captured with GPS data by the geodetic coupling coefficient (called "seismic coupling" by *Winberry et al.* (2014)), which is the percent of total ice motion accommodated by unstable slip. Sites with the largest slip deficit between unstable slips have the highest geodetic coupling coefficient. These high geodetic coupling sites move little except during unstable slip, because of either locally higher basal drag or stress shielding by the higher basal drag areas. Geodetic coupling is calculated for 39 WIP GPS sites by fitting downstream displacement curves from each unstable slip to a hyperbolic tangent curve, following the method of *Larson et al.* (2004). Displacement during and before each unstable slip is determined from the fit, and geodetic coupling is the ratio between unstable displacement summed over all slips and all displacement since the previous slip (both stable and unstable) summed over all slips (Figure 2.2B; additional details in Supplement).

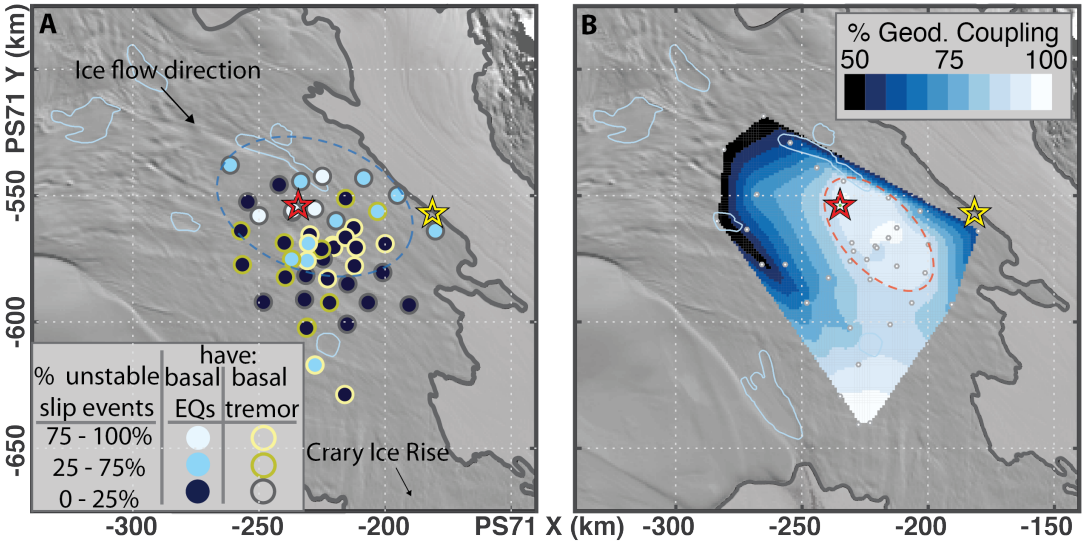

Figure 2.2: Results of seismic and GPS analysis. A: Circles are locations of seismometers deployed in 2010–2011. Colors show percentage of unstable slip events in the dataset recording basal micro-earthquakes (circle fill color) and basal tremor (circle outline color). Blue oval outlines main area with basal micro-earthquakes and tremor. B: Interpolated geodetic coupling, or the percent of total ice motion that occurs during unstable sliding. Grey dots are locations of GPS used. Red oval outlines high geodetic coupling patch. Both: red and yellow stars are the central (high tide) and grounding zone (low tide) nucleation areas, respectively (*Pratt et al.*, 2014). Light blue outlines indicate subglacial lakes (*Fricker and Scambos*, 2009). Thick grey line is the grounding line from *Bindschadler et al.* (2011).

2.4 Results

The percent of unstable slip events with basal micro-earthquakes and tremor varies across the WIP (Figure 2.2A). Basal micro-earthquakes occur commonly during unstable slip within ~40 km of the central nucleation area (blue oval, Figure 2.2A), though basal micro-earthquake occurrence rates vary significantly over distances of 1s-10s of km within this area. Seismicity is abundant at some of these sites during unstable slip, but individual basal micro-earthquakes are rarely observed at more than one seismometer. Basal micro-earthquakes occur rarely

further downstream than ~40 km from the central nucleation area, except at a site near the Crary Ice Rise and near the grounding zone nucleation area.

Figure 2.2A also shows that basal tremor occurs most often at sites slightly downstream from the central nucleation area. As shown in Figure 2.1, tremor is generally smaller amplitude than basal micro-earthquakes. Some of the seismic sites have only basal micro-earthquakes or tremor during unstable slip, while other sites have both or neither.

Figure 2.2B shows interpolated GPS-determined geodetic coupling. A central patch of high geodetic coupling (>80% of ice motion occurs during unstable slip events) is ~30 km across and extends ~50 km downstream of the central nucleation area (red oval, Figure 2.2B). This patch corresponds to the Central Sticky Spot of *Winberry et al.* (2014). The low-tide, grounding zone nucleation area is meanwhile characterized by low geodetic coupling. This area moves 10s of cm between unstable slip events. Geodetic coupling is highest at the two sites upstream of Crary Ice Rise, where ice is effectively stagnant between unstable slip events.

The central high coupling area overlaps with the high basal seismicity area, but it is narrower across flow and offset downstream (Figure 2.2, 2.3A). For all the seismic sites, there is no statistically significant correlation between calculated geodetic coupling and the percent of unstable slips with basal micro-earthquakes or tremor.

2.5 Discussion

2.5.1 Spatial patterns in seismicity and geodetic coupling

Sites that most often record distinct basal micro-earthquakes cluster around the central nucleation area, suggesting that conditions that cause stick-slip nu-

cleation are also associated with basal seismicity (Figure 2.2A). Within this seismically active area, the frequency of seismicity during unstable slip is variable in space, with seismometers that often record seismicity neighboring seismometers that rarely record seismicity. Bed conditions that cause basal micro–earthquakes, therefore, are highly heterogeneous and vary over length-scales of less than a few km (illustrated in Figure 2.3A).

The central nucleation area exhibits clear stick-slip behavior at two length scales: the scale of unstable slip nucleation (<10s of km, *Lipovsky and Dunham* (2017); *Pratt et al.* (2014)), and the smaller scale of asperities that generate basal micro-earthquakes. This smaller scale is uncertain but may be approximately 10 m^2 for tremor (*Lipovsky and Dunham*, 2016) and is certainly less than inter-station distances of ~1km. The overlap of these two scales of stick-slip behavior suggests that the bed conditions that cause basal micro–seismicity may in aggregate be the same conditions that cause nucleation of ice-plain-wide unstable slip. We propose that the central nucleation area sticks between unstable slips because it has higher basal traction, apparent in the high geodetic coupling, and different frictional basal properties than surrounding aseismic areas of the WIP bed. Basal micro-earthquakes may indicate the spatial extent of the higher basal traction and basal till conditions that promote stick-slip. This is consistent with the modeling results of *Lipovsky and Dunham* (2017), who show that large-scale heterogeneity in frictional properties is required to reproduce the shape of GPS displacement curves during ice-plain-wide unstable sliding.

Subglacial tremor typically occurs in a spatially distinct part of the WIP, in a halo of sites that overlap with but are mainly downstream of the central nucleation area and the sites with basal micro-earthquakes. Seismicity changes from relatively larger amplitude discrete basal micro-earthquakes upstream to

smaller amplitude tremor further downstream (Figure 2.2A), suggesting that the conditions causing basal seismicity change with distance downstream of the central nucleation area (*Lipovsky and Dunham*, 2016).

The area with high geodetic coupling is offset downstream of the central nucleation area (Figure 2.2B). This offset makes sense if we assume the central nucleation area is an area of higher basal traction. The WIP has very low driving stress because the surface slope is shallow (0.4×10^{-3}) (*Bindschadler et al.*, 1987). If the WIP becomes "stuck" on the higher basal traction area between unstable slips, the area just downstream is shielded from the longitudinal upstream push. It consequently moves little between unstable slips, and both areas accumulate a comparable slip deficit until pulled by the falling Ross Ice Shelf tide or until the central nucleation area is loaded to failure. This shielded area is observed as the downstream continuation of the high geodetic coupling patch.

Basal micro-earthquakes are also observed at the site nearest the grounding zone nucleation area, though sparse station coverage precludes thorough characterization of seismicity in that area (yellow star, Figure 2.2A). The presence of basal micro-earthquakes at sites near the grounding line suggests that the basal conditions causing basal micro-seismicity and stick-slip are present in that region as well. Given the lack of station coverage, we hesitate to interpret basal seismicity near the grounding zone nucleation area further. Surprisingly, there is little strain accumulation near the grounding zone nucleation area between unstable slip events despite the fast acceleration of unstable slip in this area (*Pratt et al.*, 2014; *Walter et al.*, 2015). There may instead be basal stress conditions that are transiently important as local tide falls (*Walter et al.*, 2015) that are not recorded in the sparse geodetic data.

The widespread presence of seismicity, both basal micro-earthquakes and tremor,

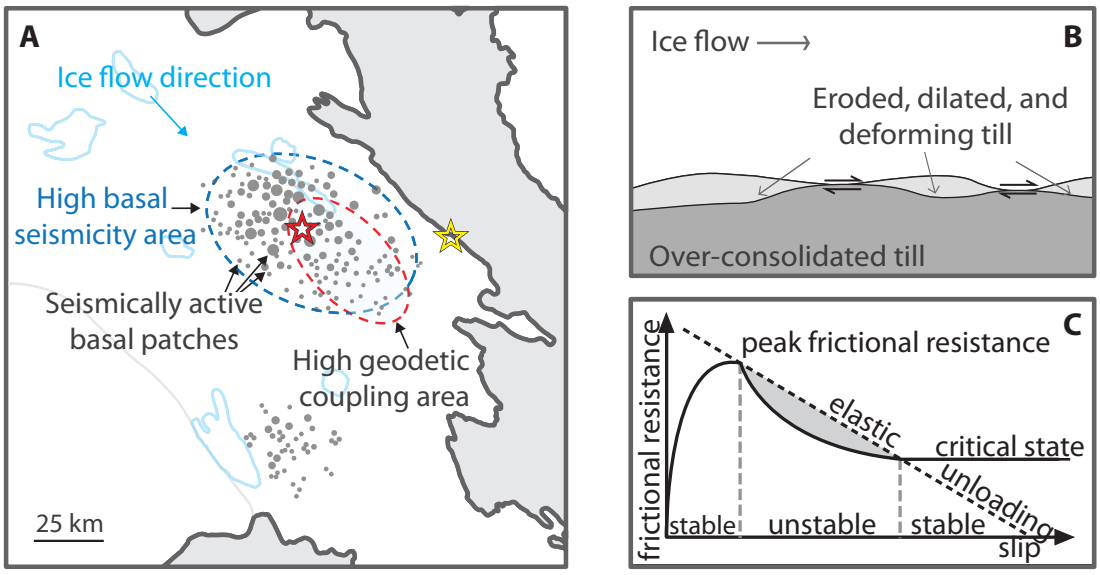

Figure 2.3: A: Conceptual model of basal till conditions schematically showing areas of seismogenic stick-slip (grey) and aseismic stable sliding (white) beneath the Whillans Ice Plain. Seismically active areas (grey) may be dominated by over-consolidated till. Ovals are from Figure 2.2, showing the approximate area that regularly records basal micro-earthquakes and tremor (blue), and the high geodetic coupling area (red). Unstable slip event nucleation at the central nucleation area (red star) may happen when enough stick-slip basal patches break simultaneously. B: Cross section of ice base showing conceptual model of over-consolidated till outcropping through high-porosity deforming till. Basal micro-earthquakes may occur by a slip-weakening mechanism between over-consolidated till and basal ice. Scale is unknown and intentionally left out. C: Schematic illustration of slip-weakening failure mechanism for basal micro-earthquakes in over-consolidated till. The fault is loaded elastically until peak frictional resistance is reached, after which frictional resistance decreases. In over-consolidated till, this corresponds to elastic loading of till grains in their over-consolidated configuration until frictional grain contacts start failing. Frictional resistance drops as grains move out of an over-consolidated packing and lose some frictional contacts. If the frictional resistance drops faster than the elastic unloading with slip (grey area), the excess elastic stress results in acceleration (unstable sliding) and emission of seismic waves. With continued slip, grains reach a steady state porosity and shear strength (critical state), and unstable sliding due to force imbalance is inhibited.

around the nucleation areas implies that a frictional description of ice-bed interactions that allows stick-slip may be appropriate for large portions of ice stream beds (Figure 2.3A). This is consistent with the modeling results of *Lipovsky and Dunham* (2017), who successfully reproduce the GPS displacement curves of the ice-plain-wide unstable slip events using an ice stream model with rate-and-state friction as a basal sliding law and large-scale heterogeneity in frictional bed properties. However, the specific mechanism for the much smaller basal seismicity remains unclear. We next propose a mechanism for these basal micro-earthquakes and tremor.

2.5.2 Constraints on a basal micro-earthquake mechanism

Basal micro-earthquakes and tremor have been successfully modeled as shear displacements near the ice-bed interface in several ice stream environments (*Anandakrishnan and Bentley*, 1993; *Blankenship et al.*, 1987; *Lipovsky and Dunham*, 2016; *Roeoesli et al.*, 2016; *Smith et al.*, 2015). For seismic energy to be radiated from a shearing fault, friction of the fault surface must be either slip-weakening (frictional resistance decreases as fault slip distance increases) or velocity-weakening (frictional resistance decreases with increased fault slip velocity). In either case, if the frictional resistance decreases (fault weakens) faster than elastic stress is released (elastic unloading), the unbalanced elastic stress causes transient inertial acceleration on the fault. This short-lived acceleration is 'unstable' sliding and can radiate seismic energy (e.g. *Scholz*, 2002).

Velocity-weakening friction is typically invoked to cause tectonic earthquakes using the framework of rate-and-state friction (e.g. *Scholz*, 1998), but the limited experimental evidence of till frictional properties suggests conflicting behavior: tills from different environments may be plastic (*Kamb*, 1991) but velocity-

strengthening (*Rathbun et al.*, 2008; *Tulaczyk et al.*, 2000), or velocity-weakening (*Iverson et al.*, 1998; *Iverson and Zoet*, 2015; *Thomason and Iverson*, 2008). The most relevant till sample comes from upstream Whillans Ice Stream, and this till exhibits a slight increase in yield strength as strain rate increases, or velocity-strengthening behavior (*Tulaczyk et al.*, 2000). Though the sample comes from 200 km upstream of the ice plain, this result makes simple velocity-weakening an unattractive mechanism for basal seismicity in this till and leads us to search elsewhere besides rate-and-state-friction for a mechanical explanation for basal micro-earthquakes and tremor in till. Ploughing of clasts embedded in the base of the ice through wet low diffusivity till can also cause velocity-weakening behavior (*Iverson*, 2010; *Thomason and Iverson*, 2008). We search for other mechanisms, though, because there is evidence of basal micro-seismicity when there is no apparent surface velocity (*Winberry et al.*, 2013), which is inconsistent with the ploughing model, and there is no obvious way ploughing can arrest slip and result in interseismic healing and stress accumulation to produce repeating basal icequakes and tremor.

A clue about the potential mechanism of basal micro-earthquakes in till comes from the Rutford Ice Stream, where *Smith* (2006) and *Smith et al.* (2015) showed that basal micro-earthquakes occur in areas of the bed with relatively lower porosity till, as inferred by active-source measurements of seismic impedance. Adopting this interpretative framework, we likewise suggest that the seismically active central nucleation area consists of a heterogeneous bed dominated by till with relatively lower porosity than the surrounding ice plain till, and therefore higher basal traction and greater likelihood to experience stick-slip motion and basal micro-earthquakes. This framework is consistent with the nearby active seismic results of *Luthra et al.* (2016) showing the till porosity near the stick-slip cen-

tral nucleation area is lower than that determined for a faster-moving upstream section of the Whillans Ice Stream (*Blankenship et al.*, 1986). Experimental evidence for velocity-strengthening behavior of Whillans Ice Stream till (*Tulaczyk et al.*, 2000), evidence that basal micro-earthquakes happen beneath the Rutford Ice Stream where till porosity is lower (*Smith*, 2006; *Smith et al.*, 2015), and evidence that the central nucleation area till may indeed have lower porosity than upstream till (*Luthra et al.*, 2016) together point to a basal micro-earthquake mechanism involving low porosity, stiff till that is likely velocity-strengthening.

2.5.3 A proposed slip-weakening mechanism for ice stream basal micro-earthquakes

We conjecture that the small basal micro-earthquakes and tremor happen during a slip-weakening failure of over-consolidated low porosity till as it is being subglacially eroded and converted into high-porosity, weak till. The higher porosity till may still be velocity-strengthening after dilation, consistent with laboratory tests on samples from upstream Whillans (*Tulaczyk et al.*, 2000). Over-consolidated till will be transiently slip-weakening (Figure 2.3C) (*Tulaczyk et al.*, 2000), and velocity-weakening behavior may not be required to generate basal seismicity. An over- consolidated sediment is one that has lower porosity and higher shear resistance than would be reached by compaction under the current effective normal stress. Over-consolidation of till indicates higher effective normal stress in the past, perhaps because of previously lower subglacial water pressure, thicker ice with no change in absolute subglacial water pressure, or erosion into till layers that used to be located deeper in the till package package and experienced greater overburden stress due to the combined weight of ice and sediment. Over-consolidation happens because till porosity reduction is largely maintained when

effective normal stress decreases again, provided the till is not sheared (*Tulaczyk et al.*, 2000). Importantly, the shear resistance of over-consolidated sediment deformed under a constant effective stress reaches a peak value at failure and then decreases with increasing shear strain towards a critical state value, often referred to as the ultimate shear strength (Figure 2.3C) (*Jeffreys and Been*, 2015; *Tulaczyk et al.*, 2000). Just like velocity-weakening, this "slip-weakening" during post-failure deformation of over-consolidated sediment can cause transient stress imbalances if it happens faster than the elastic unloading of the fault walls, resulting in local accelerations, unstable sliding, and seismic energy radiation (Figure 2.3C). This mechanism could also produce basal micro-earthquakes beneath other ice streams and glaciers that do not experience stick-slip at the scale of the Whillans ice-plain-wide unstable slip events.

In a fine-grained, water-saturated till, such as is found beneath the Whillans Ice Stream, slip-weakening during dilation of over-consolidated till may be complicated by dilatant strengthening. Dilatant strengthening occurs in over-consolidated fine-grained sediments when rearrangement of grains during shear causes an increase in shear zone porosity, a corresponding decrease in shear zone pore pressure, and consequent strengthening of the dilating shear zone. This strengthening is transient because it lasts only until ambient pore pressure can diffuse back into the shear band (*Moore and Iverson*, 2002). Dilatant strengthening does not preclude shear accelerations and unstable slip, though it can arrest them once they begin.

An illustrative example is reported in *Moore and Iverson* (2002, their Fig.2). The authors use a ring-shear device to experimentally produce a series of brief unstable sliding events in wet over-consolidated till. The unstable slips remain "slow", and the authors argue they are arrested by dilatant strengthening. These may be analogous to the slip-weakening mechanism that we propose: As the

over-consolidated till shears, its shear strength drops due to rearrangement of the tightly packed grain framework attained during over-consolidation. This decrease in shear resistance leads to unbalanced forces that cause acceleration. But the fast slip phase is also associated with rapid dilation, which causes a local drop in pore water pressures and a corresponding increase in effective stress and frictional shear resistance. At some point the dilatant hardening becomes dominant and slip is temporarily arrested or slowed until pore water flows back into the shear zone, eventually allowing another acceleration. As shown in *Moore and Iverson* (2002), it may require many episodes of shear followed by dilatant hardening for a sediment to reach critical state, which may explain our observations that basal micro-earthquakes and tremor can repeat up to many hundreds of times in the same location during a single ice stream-wide slip event lasting 20-30 min. At the same time, micro-earthquake source locations do not persist for more than a few slips, presumably because the subglacial sediment reaches critical state after many micro-earthquakes.

Slip-weakening friction is thought to be important in other geologic settings, for example the Nankai Subduction zone, though the mechanism is slightly different. The Nankai subduction zone features very low frequency earthquakes, a type of earthquake that is deficient in high frequencies, possibly due to lower rupture velocities. These slow earthquakes typically occur outside of the frictional limit of the seismogenic zone of subduction zones, for example in Nankai (*Obara and Ito*, 2005) and Costa Rica (*Walter et al.*, 2013). High clay content samples from the Nankai subduction zone exhibit velocity-strengthening behavior when a velocity increase is imposed during laboratory experiments. However, the samples also exhibit weakening over larger slip distances as slip continues after the velocity perturbation(s) (*Ikari et al.*, 2013). The velocity-strengthening behavior of

Nankai samples is inconsistent with the seismic observations of very low frequency earthquakes, but the earthquakes may be explained by the slip-weakening over larger slip (*Ikari et al.*, 2013; *Ito and Ikari*, 2015). Though the slip-weakening of Nankai material beyond the initial velocity-strengthening response is slightly different than slip-weakening of over-consolidated till, the observations from Nankai suggest that slip-weakening may cause seismogenic fault behavior.

2.5.4 Regional frictional properties and ice-plain-wide stick-slip

Considering our proposed slip-weakening mechanism of basal seismicity, we interpret that our observation of kilometer-scale heterogeneity in basal micro-earthquake and tremor activity results from small, localized, seismically active patches of over-consolidated till deep in the till package exposed by erosion and outcropping through a layer of aseismically deforming, high porosity, weak till. This is similar to a conceptual picture in (*Alley*, 1993), and there may be evidence for such outcrops in active seismic results from upstream Whillans Ice Stream (*Rooney et al.*, 1987). Figure 2.3B illustrates our conceptual picture of the ice-bed interface: basal micro-earthquakes occur by slip-weakening in the over-consolidated till where it contacts the ice bottom. As this over-consolidated till dilates and erodes, it is transported downstream, becoming part of the aseismically deforming till package. Ice stream motion causes horizontal transport of this high-porosity, aseismic till, estimated to be < 40 m^3 m^{-1} yr^{-1} beneath the WIP (*Hodson et al.*, 2016). Provided the basal sedimentary environment is erosive, till flux from upstream plus till generation by erosion is less than till advection downstream. Eventually, new over-consolidated till is exposed to maintain locally higher basal tractions and allow the WIP stick-slip cycle and probably basal

micro-earthquakes to persist for more than a decade (*Bindschadler et al.*, 2003; *Siegfried et al.*, 2016).

We additionally suggest that the overlap between the central nucleation area and the cluster of sites that most often record distinct basal micro-earthquakes indicates that the conditions that cause basal micro-earthquakes and tremor are the same conditions that nucleate the WIP-wide unstable slip events. Because over-consolidated, lower porosity till has a transiently higher peak shear strength than its normally consolidated equivalent, it can offer locally higher basal resistance to ice motion. If slightly stronger over-consolidated till is continuously exposed by erosion and in contact with the ice base over a large area, the ice stream can become transiently "stuck" on it with ice-plain-wide unstable slip events initiating when a large enough area of over-consolidated till is loaded to failure and starts to experience weakening. Then, ice-plain-wide unstable slip in surrounding aseismic areas of the ice plain can be sustained by velocity-weakening ploughing of clasts through non-over-consolidated deforming till, or some other velocity-weakening mechanism of till deformation (*Iverson*, 2010; *Lipovsky and Dunham*, 2017; *Thomason and Iverson*, 2008). Thus, the area of the WIP bed that features basal seismicity, the size of the high geodetic coupling patch, and the location of the central stick-slip nucleation area may all be controlled by the spatial distribution of varying till mechanical properties, for example the areal density or size of the outcrops of slip-weakening till that may interact to nucleate the large scale unstable slip.

We also note that *Lipovsky and Dunham* (2017) successfully model the ice-plain-wide unstable slip events using a rate-and-state frictional constitutive law for basal sliding. This suggests that the aggregate frictional properties of the ice plain at ~10 km scales may be reproduced by rate-and-state friction, but this does

not preclude a non-rate-and-state friction explanation for basal micro-earthquakes happening on localized meter-scale basal faults.

We propose that outcrops of over-consolidated till may be regions that catch on the ice bottom, generate basal micro-earthquakes, and if covering a wide enough area, can generate large scale stick-slip such as is observed for the WIP. If subglacial erosion in the nucleation area exposes larger areas of over- consolidated, stiff till, the WIP bed will continue to strengthen and we may observe changing basal seismicity. Regardless of the mechanism of basal strengthening, conditions that are currently causing basal strengthening and slowdown of the WIP (*Beem et al.*, 2014; *Joughin et al.*, 2005) may become more favorable in the future to form a slow-moving ice ridge in the middle of the ice plain with a narrower Whillans Ice Stream flowing to the north. Seismicity from the bed of an ice stream may therefore be indicative of changing bed properties that can trigger significant rearrangement of regional ice flow patterns and velocity fields over the coming decades and centuries.

2.6 Summary

We compare the spatial patterns of basal seismicity, tremor, and geodetic coupling with the inferred nucleation areas of the well-known WIP unstable sliding events. We find that while seismicity rates are heterogeneous between neighboring sites, there are informative regional patterns. Basal micro-earthquakes typically happen at a cluster of sites overlying the central nucleation area and the upstream end of a central highly geodetically coupled patch. Tremor generally occurs downstream of this cluster. The dominant type of seismicity changes from larger amplitude individual basal micro-earthquakes upstream to small amplitude tremor and seismically quiet bed further downstream, indicating changing basal

conditions.

These results confirm that the WIP bed is heterogeneous (e.g. *Alley*, 1993; *Rooney et al.*, 1987) and that ice sliding can be described using a frictional constitutive law at both the large scale of unstable sliding nucleation (*Lipovsky and Dunham*, 2017) and the small scale of basal-earthquake-generating asperities. We adopt the interpretive framework of *Smith* (2006) and *Smith et al.* (2015) in suggesting that basal micro-earthquakes beneath till-bedded ice streams occur in low porosity, stiff till. As a possible mechanism, we propose sudden, slip-weakening till deformation and failure on a plane in over-consolidated till. Because an over-consolidated till has a transiently higher peak shear strength than the same till at critical state, discrete basal micro-earthquakes and tremor in till may indicate areas of higher basal shear strength. This slip-weakening mechanism for small basal seismicity has potential implications for modeling of basal traction in ice sheet models.

The relative abundance or absence of basal micro-earthquakes yields information about the bed conditions and stresses at the bottom of the ice and the spatial extent of low porosity till that is eroding during ice motion. Further study with dense seismometer networks is required to understand the mechanism and relevance of basal seismicity to understanding fast ice flow

2.7 Acknowledgements

This work was supported by the National Science Foundation [grants ANT-1043784, ANT-1443525] as well as by logistical support from the United States Antarctic Program. We thank Lucas Beem, Douglas Fox, Kristin Poinar, Rickard Petterson, Nadine Quintana-Krupinski, Jake Walter, and John Woodward for their assistance with GPS fieldwork. We additionally thank Patrick Fulton, Thorne

Lay, and Neal Iverson, and an anonymous reviewer for their thoughtful comments on this manuscript.

Chapter 3

Icequake streaks revealed at the base of an Antarctic ice stream

3.1 Abstract

Records of small icequakes emanating from an active ice stream basal slip surface provide high spatial and temporal resolution insights into otherwise difficult to observe sub-km scale basal heterogeneity. We detect microseismicity beneath a ~3 km wide sensor network installed on the Whillans Ice Plain (WIP), in West Antarctica, and we use S-wave backprojection to detect and locate thousands of basal icequakes occurring over 14 and 21 days in January and December 2014, respectively. Event locations occur in several streaks that are several hundred meters wide, several hundred meters apart, and parallel to the ice flow direction. These streaks are similar in plan-view to mega-scale glacial lineations (MSGL) from paleo-ice stream beds. An adjacent ice-penetrating radar line shows a ~2m amplitude undulating basal surface, indicating the presence of MSGLs in the study area. We propose that the basal icequake streaks are linked to the geomor-

phic processes shaping these MSGLs. One icequake streak happens in a shallow trough beside a MSGL, suggesting MSGL formation can be at least locally erosive in troughs between MSGL ridges. We interpret that icequake streaks occur where a surface layer of soft, aseismic, deformable till is thinned between the ridges, exposing deeper, stiffer, more brittle material–possibly over-consolidated till. If the geomorphic evolution of the basal surface exposes a greater area of stiff material over time, this may contribute to long-term increase in basal resistance and WIP slowdown.

3.2 Introduction

The conditions at the base of ice streams affect their flow velocity and ice discharge rates into the ocean. Ice stream beds are thought to be a generally weak mosaic of lubricating subglacial water and deformable till, with an outsized amount of basal resistance contributed by localized 'sticky spots' (e.g. *Alley*, 1993; *Stokes et al.*, 2007) that have proven difficult to relate to paleo-ice stream bed geomorphic features (*Stokes*, 2018). The spatial and temporal scales at which basal material heterogeneity, thermal conditions, hydrology, geomorphology, and resulting basal traction vary beneath active ice streams is largely unresolved due to difficult access and scarcity of observational methods sensitive to basal properties at appropriate spatial scales. There is, however, abundant evidence for sub-km scale heterogeneity found in the striated and streamlined geomorphic records of former ice streams globally (see *Stokes* (2018), for a comprehensive review), suggesting that basal geomorphology may be responsible for some basal heterogeneity. The impact of meter- to km-scale basal geomorphic heterogeneity on the large-scale flow dynamics of ice streams is unknown, though it is reasonable to assume that ice streams with low driving stress and weak beds may be highly sensitive to

small local changes in basal conditions and resistance, such as may be caused by evolving basal geomorphology. Understanding the scale and causes of basal heterogeneity is also critical for extrapolating basal conditions observed by borehole point measurements to a larger ice stream area. Here, we investigate heterogeneity in basal conditions beneath a small area of the Whillans Ice Plain, in West Antarctica, using passive seismic observations of basal icequakes, and we relate the basal heterogeneity to inferred basal geomorphology.

Observation of micro-seismicity emanating from the sliding interface of ice streams is a valuable high temporal and spatial resolution method for analyzing heterogeneous basal conditions, for example spatial variation in till mechanical properties (*Smith et al.*, 2015) and temporal variation in subglacial water pressure (*Roeoesli et al.*, 2016). These small seismic signals (Figure 3.1C) are typically attributed to shear dislocation across the ice-till interface, similar to motion of typical seismogenic crustal faults. Focal mechanisms of basal icequakes show double-couple slip sub-parallel to the ice base (*Anandakrishnan and Alley*, 1994; *Anandakrishnan and Bentley*, 1993; *Blankenship et al.*, 1987; *Roeoesli et al.*, 2016; *Smith et al.*, 2015; *Zoet et al.*, 2012), indicating that ice stream basal sliding includes some component of stick-slip over brittle materials, even in areas of fast-moving ice thought to be underlain by soft, deformable till. Spatial patterns of basal icequake occurrence are only beginning to be studied and related to varying basal conditions (e.g. *Smith et al.*, 2015; *Roeoesli et al.*, 2016) and to the large-scale dynamics of ice streams (*Barcheck et al.*, 2018); and basal seismicity has not been considered in relation to soft sediment basal geomorphology before. These basal icequake seismic signals provide a valuable high-temporal-resolution constraint on the spatially heterogeneous nature of ice stream basal boundary conditions and the temporal relationship of that small-scale heterogeneity to the

large-scale ice stream dynamics.

A key location to study heterogeneous local basal conditions and effects on ice dynamics is the Whillans Ice Plain (WIP) in West Antarctica (Figure 3.1D). In addition to being known for accomplishing most of its sliding across the entire ice plain via daily unstable stick-slip events (*Bindschadler et al.*, 2003), the WIP has been slowing down since at least the mid-1980s (*Joughin et al.*, 2005; *Beem et al.*, 2014). The slowdown is thought to result from an increase in basal resistance driven by basal freeze-on, changes in subglacial hydrology, or differential erosion of bed materials (*Beem et al.*, 2014). The relative dominance of these different mechanisms of ice stream slowdown may be distinguishable in spatiotemporal patterns of basal seismicity, particularly in the "Central Sticky Spot" that controls the stick-slip cycle and possibly the long-term slowdown behavior of the ice stream (*Winberry et al.*, 2014).

Here, we investigate spatial patterns in basal seismicity and inferred bed heterogeneity beneath the Central Sticky Spot (Figure 3.1D), a 10s-of-km wide area where much of the strain accumulation happens between WIP unstable slip events (*Winberry et al.*, 2014; *Barcheck et al.*, 2018), and where unstable slip often nucleates (*Pratt et al.*, 2014). We use a small network of surface seismometers to constrain patterns in basal seismicity within a ~13km^2 area on the Central Sticky Spot (Figure 3.2A). We detect basal icequakes (Figure 3.1C) using an S-wave backprojection method, revealing elongate streaks of basal seismic activity during several weeks of recording in two consecutive austral summers. The spacing and elongation of the seismicity streaks are consistent with those of mega-scale glacial lineations (MSGL) from paleo-ice stream beds, and the probable presence of MSGL or other bedforms is supported by sparse radar evidence of a gently undulating ice stream bed with a few meters amplitude. One icequake streak appears

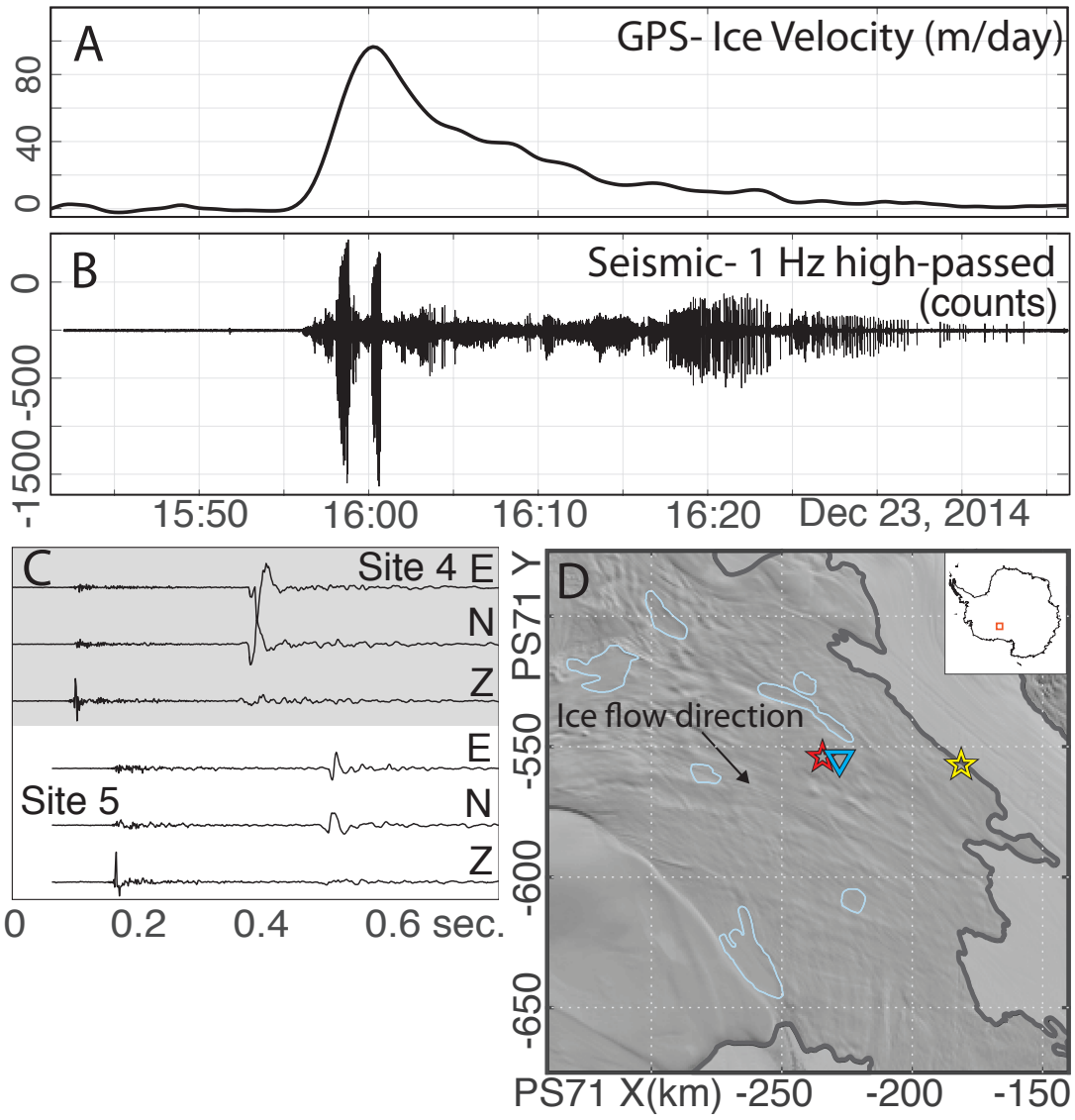

Figure 3.1: A: GPS-derived downstream ice velocity during a Whillans Ice Plain unstable sliding event. GPS position data with 15 second sampling interval are low-pass filtered below 300 seconds, and ice velocity is calculated as the slope of a line fit to 4 consecutive datapoints. B: Seismicity recorded at blue triangle in D during unstable slip event shown in A. Data are 1 Hz high-pass filtered. Each spike is an individual basal icequake. C: Example basal icequake shown at 2 proximal seismic sites, 750 m apart. D: Whillans Ice Plain. Location of seismic network shown by blue triangle. Unstable slip nucleation areas are shown by red and yellow stars (*Pratt et al.*, 2014). Thick grey line is the grounding line from (*Bindschadler et al.*, 2011). Light blue outlines show subglacial lakes from (*Fricker and Scambos*, 2009).

to be in a shallow local trough. This leads us to propose that MSGL evolution includes basal conditions that are at least locally erosive in MSGL troughs, and that WIP basal icequakes occur where soft, high porosity deformable till is thinned or removed and the ice base is instead sliding atop deeper, stiffer till or sediment. A major implication is that evolving subglacial geomorphology can affect basal conditions, especially by temporally changing heterogeneous exposure of the ice base to till of variable strength and frictional properties. These results also have implications for understanding the conditions that cause streaked seismicity in other geologic settings, such as in fault zones (e.g. *Rubin et al.*, 1999).

3.3 Basal Icequake Detection Method

Basal icequakes are small seismic events happening at or near the interface between ice and bed. We detect WIP basal icequakes for several weeks during two consecutive austral summers using a small network of 8-9 short period seismometers installed on the Central Sticky Spot (at location of blue triangle in Figure 3.1D), where the majority of WIP ice-plain-wide unstable slip events nucleate (red star in Figure 3.1D) (*Pratt et al.*, 2014). The network setup is shown in Figure 3.2A for January 2014 (red triangles) and December 2014 (blue triangles). We analyze 21 days of data in January 2014 and 14 days in December 2014.

Basal icequakes beneath the WIP typically have clear P and S waves (Figure 3.1C), with changes in P-wave arrival polarity across the network indicating a double-couple shear source. Many hundreds to thousands of basal icequakes occur during a WIP-wide unstable slip event that typically lasts about 30 minutes. Arrivals from different icequakes often overlap in time, making detection and association of arrivals challenging. We therefore use an S-wave backprojection technique to detect and locate basal icequakes.

First, we extract horizontal component seismic data and convert to a short term average over long term average data stream (STA/LTA). Then, the STA/LTA data streams are set to zero below a threshold determined to isolate local S wave arrivals; an example is shown in Appendix B. Next, a 50 m spaced grid of potential source locations is generated at the ice base, assumed to be 690 m below the seismometers based on ice thickness determined with ice penetrating radar (*CReSIS*, 2018). S-wave travel times from all grid points to all seismic sites are calculated using a temperature-based seismic velocity model (*Kohnen*, 1974), described in Appendix B. Then, thresholded STA/LTA data from each seismometer are migrated back in time to each grid point by the calculated travel times, and the migrated data are stacked, forming a back-projected "beam" of S-wave energy. Basal icequakes are then detected in 0.24 second windows where S-waves coherently stack, described in detail in Appendix B. Basal icequake detections are retained only if 7 or more S-waves contribute to the detection (minimum 5 sites). A basal icequake location is determined by this method to be within the 50x50 m area surrounding a basal grid point.

We use this backprojection method to detect and locate basal icequakes during 30 and 18 ice-plain-wide unstable slip events in January and December 2014, respectively, for a total of 48 unstable slip events over 35 days. We analyze data from 15 minutes before to 60 minutes after GPS-determined unstable slip initiation. We do not process data between unstable slip events because basal seismicity is extremely rare between unstable slips. In total, we detect 15,969 basal icequakes over this period.

3.4 Results

During an individual unstable slip event typically lasting ~30 minutes, only a few locations beneath the seismic network are seismically active, but the ice base collectively generates many microseismic events during this brief period of activity (Figure B.4). During the most micro-seismically active unstable slip, we detect 1,683 basal icequakes, and during the least active (or perhaps noisiest) we detect only 22 basal icequakes. Close examination of the detected basal icequakes shows events detected at the same grid point to be nearly identical, repeating basal icequakes, as previously observed beneath other areas of the WIP (Winberry et al., 2013, Barcheck et al., 2018). Icequakes are typically detected at 2-10 grid points per unstable slip event (Figure B.4), meaning $> 99.7\%$ of the ice stream bed is aseismic beneath the network. No spatial patterns are typically observed during a single unstable slip event.

Cumulative basal seismicity, however, shows a striking pattern after only a few weeks: Integrated over all 48 unstable slips analyzed in both years, cumulative basal seismicity shows at least three streaks of seismically active ice stream bed separated by generally aseismic bed (Figure 3.2A). These streaks are elongated in the ice flow direction, as determined by a local GPS site (circles, Figure 3.2A). The two major streaks are spaced about 750m apart, and a third is another few hundred meters to the south.

3.5 Discussion

The streaks of basal seismicity elongated in the ice-flow direction have similar plan-view geometry to MSGLs from paleo-ice stream beds. Elongate bedforms such as drumlins and MSGL have been observed forming beneath the currently

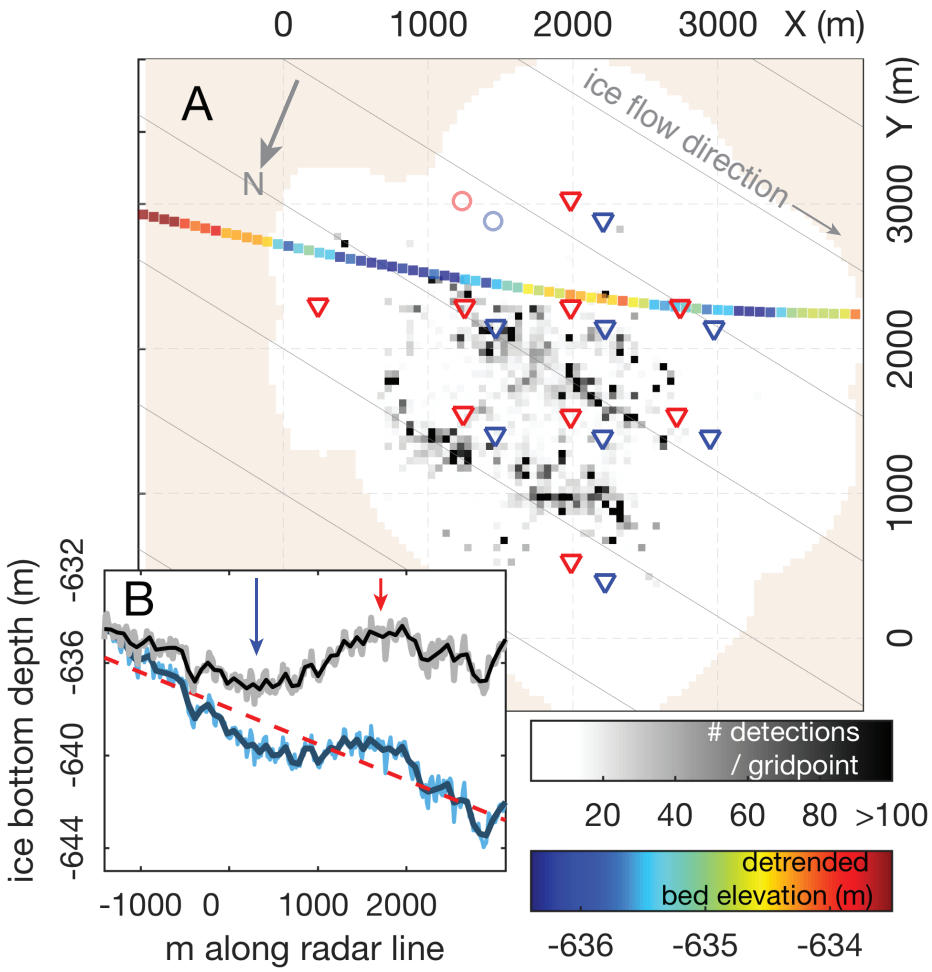

Figure 3.2: A: Seismicity detected during 48 unstable slip events. Grid points show the number of basal icequakes detected per gridpoint. Colorscale is saturated at 100 icequakes, though some gridpoints have up to 580 detections total. Tan gridpoints are beyond the sensitivity of the network, where too few horizontal channels are available to trigger a detection. Red triangles are seismometer locations in January 2014, and blue triangles are seismometer locations in December 2014. Circles show location of GPS unit in January 2014 (red) and December 2014 (blue). Colored boxes display detrended ice bottom depth, as shown by the black line in panel B. Grey solid lines show the direction of ice flow. X- and Y-axes are in polar stereographic projection with origin at PS X = -229,500 and PS Y = -557,570 m. B: Ice bottom depth below sea level determined by ice-penetrating radar (*CReSIS*, 2018). Light blue is raw data and dark blue is a 7-sample average of the raw data. Grey and black lines are detrended light and dark blue lines, respectively, detrended using the red dashed line fit to the local basal topography. Red and blue arrows indicate local peak and trough in basal topography, respectively. .

active Rutford Ice Stream (*Smith et al.*, 2007; *Smith and Murray*, 2009; *King et al.*, 2009), and are often cited as evidence of fast flow in paleo-ice stream beds (e.g. *Boulton and Clarke*, 1990). The streaks of seismicity observed here are spaced ~700m apart, consistent with measured spacing of MSGL on paleo-ice stream beds (*Spagnolo et al.*, 2014). We suggest that sub-km scale heterogeneity shown by basal seismicity beneath our seismic network is linked to the geomorphology of the basal topography.

Constraints on bed topography from ice-penetrating radar are consistent with subglacial bedforms being present beneath the ice in this area, though knowledge of detailed basal topography is limited to one radar line collected in January 2014 (*CReSIS*, 2018). The radar reveals basal topography with an overall gently dipping slope and a superposed low-amplitude undulation (dark blue line, Figure 3.2B). This topography is projected to a vertical plane fit to the surface positions, and a linear trend is removed, shown in Figure 3.2B, for comparison with the seismicity results. The detrended topography shows an undulating bed with residual amplitude of about 2m (black line, Figure 3.2B), also consistent with paleo-MSGL amplitudes (*Spagnolo et al.*, 2014). We therefore infer the presence of sparse, low-amplitude MSGL beneath our seismic network, supporting our proposition that sub-km scale basal heterogeneity shown by spatial seismicity patterns is linked to basal geomorphology.

The center streak of seismicity projects upstream into a trough of the undulating basal topography. Assuming the topographic signature of the low-amplitude MSGL persists downstream, this streak of seismicity occurs in the shallow local trough next to a MSGL. This suggests that in some basal environments, basal icequakes in the presence of bedforms occur in local lows in the basal topography, possibly where soft till has been eroded away as troughs deepen. This observation

can help to constrain the formation mechanism of MSGL or other geomorphic features.

Basal seismicity beneath the Rutford Ice Stream occurs in a broad area of the bed where "stiff", low porosity till is inferred to outcrop to the ice base and cause potentially seismogenic basal sliding (*Smith et al.*, 2015). Meanwhile, high porosity "dilatant" till is inferred to allow ice movement by till deformation, which is aseismic (*Smith et al.*, 2015). (*Barcheck et al.*, 2018) built on this observation to propose that WIP basal icequakes occur where soft, deformable till is thinned, exposing stiffer, possibly over-consolidated material from beneath the deformable till. Adapting these interpretations to our results here, we suggest that WIP basal icequakes occur in outcrops of lower porosity, "stiff" till or other material from deeper in the sediment package topped by a significantly thinned or absent layer of soft, deformable till (Figure 3.3). Where the deformable till is completely absent or eroded away, the deeper, lower porosity sediment is exposed to a heterogeneously debris-laden basal ice and is prone to brittle failure and basal icequake generation. Basal icequake streaks beneath the WIP, then, are elongate areas where MSGL or other bedform formation has resulted in erosion into deeper layers of material in MSGL troughs. Evidence of MSGL eroding into deeper, stiffer layers of sediment is found, for example, in the Ross Sea, where chirp profiles through paleo-MSGL on the seafloor show the Ross Sea unconformity heterogeneously intersecting troughs in the undulating MSGL surface (*Halberstadt et al.*, 2016, , their Figure 2B).

A thinned layer of deformable till in the MSGL trough also suggests that MSGL are formed, at least in part, by erosive processes removing soft sediment from the lows between lineations (*Eyles et al.*, 2016), not only constructional (depositional) processes in the topographic highs. A mechanistic explanation of MSGL formation or propagation should be compatible with the possibility of erosion and stick-slip

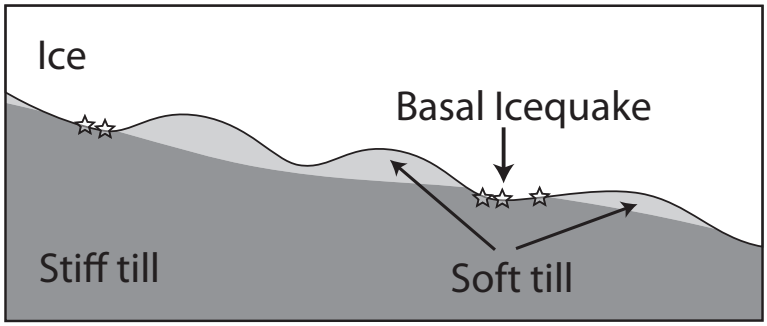

Figure 3.3: Schematic cross section of the ice base, showing ice (white) flowing out of the page, over-riding undulating basal bedforms. As a result of erosion in the troughs between bedforms, the ice base is heterogeneously in contact with surficial soft, aseismic, deformable till (light grey) in topographic peaks, and stiffer, deeper material (dark grey) in topographic lows. The stiff till is possibly over-consolidated till, which may cause basal icequakes (stars) where it contacts the ice base.

in the troughs and primarily aseismic sliding on the ridges.

The existence of lower-porosity material deeper in the WIP till package is supported by an active seismic survey performed along flow just upstream of our seismic network (*Luthra et al.*, 2016). This survey suggests that the WIP Central Sticky Spot till is in bulk more consolidated than the till beneath upstream, faster-moving reaches of the WIP (*Blankenship et al.*, 1986, 1987). *Luthra et al.* (2016) also find some evidence that the upper ~1.5m of the Ice Plain till has a lower P wave velocity and density than the bulk till, implying that the top of the till layer is interacting with the over-riding ice and has an increased porosity due to shear. This sheared surface layer may correspond to the soft, aseismic, deforming till, and the underlying higher density till may be the stiff material that outcrops where the basal icequakes originate.

The presence of three wide streaks of basal seismicity recorded in just 35 days beneath this WIP seismic network suggests that the high porosity, weak,

deformable till may be significantly thinned over a large proportion of the ice base beneath our seismic network. Basal seismicity has previously been observed beneath a wide swath of the WIP, in particular within 10s of km of the Central Sticky Spot (*Barcheck et al.*, 2018). Observations of basal seismicity over such a large area may therefore indicate that the high porosity, weak, deformable till layer is thinned beneath a large area of the ice plain. This could be because the deforming till budget is negative (*Barcheck et al.*, 2018), because of shifting basal hydrologic patterns (*Luthra et al.*, 2016) and resultant till compaction, or because of basal freeze-on (*Joughin et al.*, 2003, 2004; *Beem et al.*, 2014; *Meyer et al.*, 2018) entraining soft sediments or causing till dewatering. Over time, any of these mechanisms may expose increasingly larger areas of stiff, low-porosity till to the ice base, potentially increasing basal traction and contributing to the long term slowdown of the WIP.

Transverse variability in ice stream bed properties has been previously inferred beneath active ice streams at several locations in Antarctica. Beneath the WIP, at a site near Subglacial Lake Whillans ~50 km from our seismic network, an active seismic survey found basal reflection phases to vary between reversed and non-reversed over short distances of ~100s of m, indicating rapid transverse changes in bed sediment density and/or rigidity (*Atre and Bentley*, 1994). This basal variability was found to occur in alternating stripes elongated in approximately the ice flow direction (*Atre and Bentley*, 1994), which may be the signature of MSGL presence beneath the ice base. Similar observations of across-flow variability in inferred till properties come from patterns of high and low acoustic impedance beneath Kamb Ice Stream (*Atre and Bentley*, 1993) and in conjunction with direct geophysical observation of geomorphic bedforms beneath Rutford Ice Stream (e.g. *Smith*, 1997; *Smith and Murray*, 2009; *King et al.*, 2009). Lateral basal variability

at scales comparable to ice thickness may therefore be common beneath active ice streams. We propose that such variability is linked to the presence of bedforms, and we note that evolving basal geomorphology can cause changing heterogeneous exposure of the ice base to till of variable strength and frictional properties. Such changes in ice stream basal conditions may be an important driver of changing basal traction, especially where a greater or lesser area of high basal traction material is exposed over time as basal geomorphology evolves.

We note that comparable streaks of small tectonic earthquakes and tremor are occasionally observed in fault zones. Earthquake lineations have been observed in various creeping sections of the San Andreas Fault system (e.g. *Rubin et al.*, 1999; *Waldhauser and Ellsworth*, 2000, 2002; *Waldhauser et al.*, 2004) and on the creeping decollement beneath the south flank of Kilauea Volcano, Hawai'i (*Rubin et al.*, 1999; *Matoza et al.*, 2013). And tectonic tremor streaks have been observed during slow slip events, for example in the Cascadia subduction zone (*Ghosh et al.*, 2010). Comparison of similarities in these diverse sliding environments may yield insight about the fault zone conditions that promote elongated zones of seismicity.

In summary, we find streaks of basal icequakes likely related to the presence of MSGL beneath the WIP. We propose the streaks occur where the evolution of MSGL or other bedforms has thinned a surface layer of soft, deformable, aseismic till, exposing deeper, stiffer, brittle material in the troughs between bedforms. If a greater area of this stiffer material is exposed over time due to evolving basal geomorphology, this may be an important contributing factor in the long-term slowdown of the WIP. Evolution of the basal geomorphology may directly impact heterogeneity in basal conditions and basal traction over time by exposing the ice base to changing proportions of till with variable strength and frictional properties.

3.6 Acknowledgements

This work was supported by the National Science Foundation awards 1043784 and 1443525. Field work was made possible by the logistical support of the US Antarctic Program, the Antarctic Support Contract (ASC), IRIS PASSCAL, UNAVCO, Kenn Borek Air, and the New York Air National Guard. We thank Dan Sampson, Matt Siegfried, Esteban Chaves, Sarah Neuhaus, Marino Protti, Marci Beitch, Neil Foley, Carolyn Begeman, Brad Lipovsky, and the entire WISSARD team for their dedication and assistance with field work and logistical support. We acknowledge the use of data from the Center for Remote Sensing of Ice Sheets (CReSIS) generated with support from the University of Kansas, NASA Operation IceBridge grant NNX16AH54G, and NSF grant ACI-1443054.

Chapter 4

High resolution heterogeneity of the Whillans Ice Plain bed from basal icequakes

4.1 Introduction

This chapter is motivated by a desire to understand the basal icequake source in greater detail, and to quantify the smallest resolvable scale of basal heterogeneity. I begin by generating a refined catalog of Whillans Ice Plain basal seismicity: I extract template icequakes from the December 2014 back-projection catalog generated in Chapter 3, and I detect repeats of these basal icequakes using cross correlation. I then ask the following questions of this catalog: How big are basal icequake patches, and what proportion of the ice stream bed is moving by seismogenic stick-slip? What is the smallest resolvable scale of basal heterogeneity revealed by basal icequake activity? Do patterns in icequake characteristics such as amplitude and timing within families give clues to what the mechanism is? Is

there icequake evidence for healing of the basal interface between the unstable slip events? And in what ways are repeating basal icequakes similar to repeating tectonic earthquakes? A major focus of this chapter is understanding what the time evolution of the basal icequake families reveals about scales of basal heterogeneity beneath the seismic network.

I first describe how I generate this improved catalog of basal icequakes starting from the December 2014 back-projection catalog produced in Chapter 3. Then, I describe the overall behavior of the icequakes within the WIP stick-slip cycle: Where are the repeating icequake family sources? When do they happen in the stick-slip cycle? Are there any simple correlations between number of icequakes and ice sliding speed? Or how much healing time has elapsed since the previous unstable slip event? Then, I discuss several estimates for the size of the basal icequake patches: I determine estimates of icequake fault rupture area from spectral fitting of P waves, and I quantify the "active slip distance" over which typical icequake families are active, and the slip distance over which regular fluctuations in icequake amplitude typically take place. These estimates allow me to approximate the smallest seismically resolvable scales of basal heterogeneity–the size of these icequake patches, and to quantify the proportion of the bed that slides by local seismogenic stick-slip. I additionally hypothesize several basal processes that may be causing the basal icequakes. I also discuss seismic evidence for healing of the ice base between unstable slips. I explore another explanation for icequake amplitude fluctuations in terms of basal velocity fluctuations. And lastly, I explore some of the ways in which repeating basal icequakes are similar to or different from repeating tectonic earthquakes.

4.2 Methods

4.2.1 Seismic processing: Icequake catalog generation

In this chapter, I refine the December 2014 catalog of basal icequake detections generated by the back-projection analysis in Chapter 3 to retain only a single high quality template for each unique basal icequake family (Figure 4.1a), and then I use cross correlation of these templates to build an improved catalog of these repeating basal icequakes (Figure 4.1b, 4.2). A basal icequake "family" is defined here as a series of repeating basal icequakes with nearly identical waveforms, variable amplitudes, and having the same arrival times at all seismometers within a few samples. All detections within a family occur on the same patch of the ice stream bed within resolution. The same 18 unstable slip events occurring in December 2014 that were analyzed in Chapter 3 are included in this analysis. The timing of these 18 unstable slip events is shown in Table 4.1.

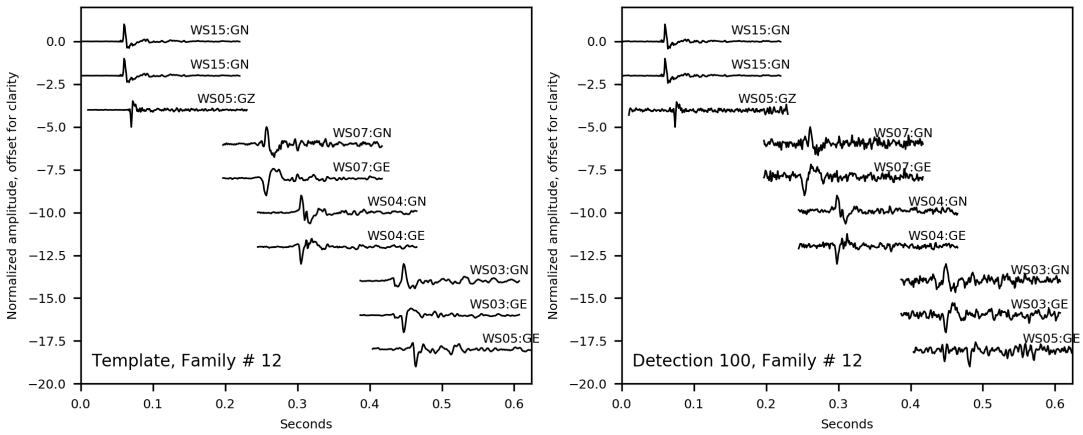

Figure 4.1: Example basal icequake template (left) and detection (right) from Family number 12.

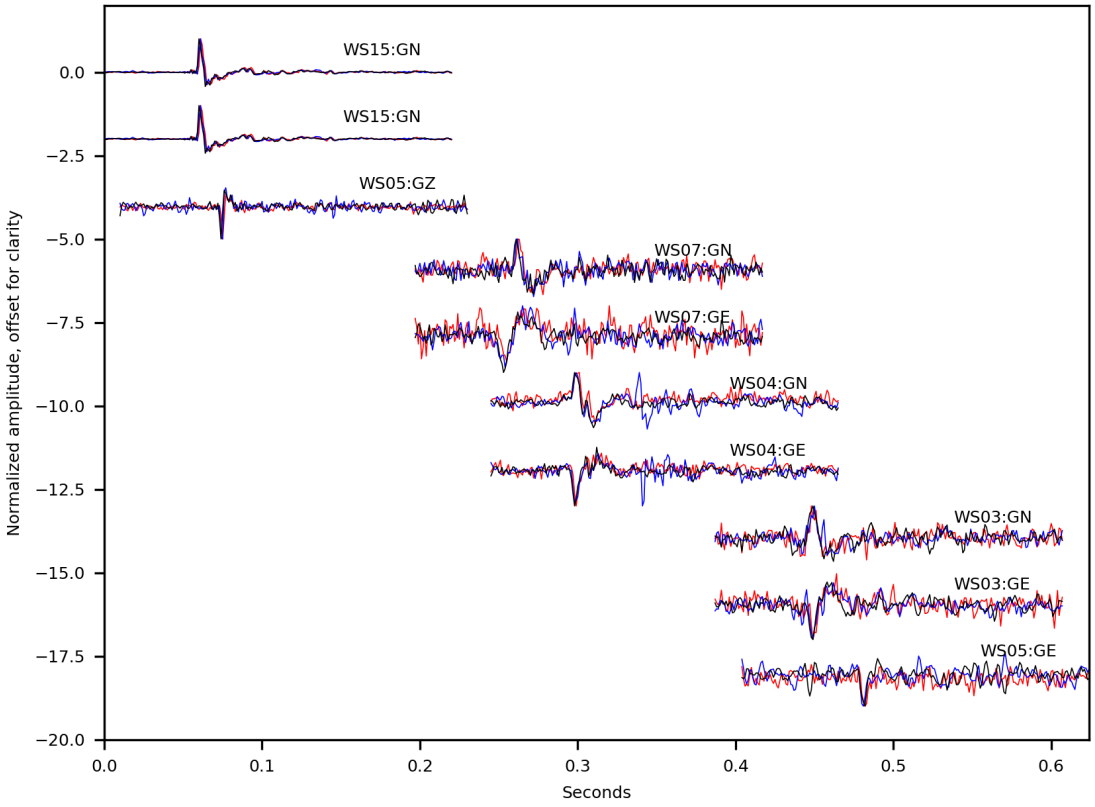

Figure 4.2: Three detections from Family number 12. Red is detection 5, blue is detection 100, and black is detection 600. Amplitudes are normalized so waves have a common vertical scale. This family has 709 detections total during unstable slip event number 3. Note the highly similar waveshapes for each detection.

Slip Number	Slip Time
1	2014-12-16 19:14:30
2	2014-12-17 10:49:30
3	2014-12-17 22:55:30
4	2014-12-18 15:01:30
5	2014-12-19 14:26:15
6	2014-12-20 14:41:30
7	2014-12-21 14:58:14
8	2014-12-22 15:32:00
9	2014-12-23 15:57:00
10	2014-12-24 02:41:45
11	2014-12-24 18:36:45
12	2014-12-25 17:18:45
13	2014-12-26 01:27:30
14	2014-12-26 18:07:45
15	2014-12-27 16:55:30
16	2014-12-28 04:18:30
17	2014-12-28 17:14:00
18	2014-12-29 16:18:45

Table 4.1: Timing of unstable slip events analyzed in Chapter 4

Extracting unique basal icequake template events from the catalog of back-projection detections

The 15,969 basal icequakes detected by the back-projection analysis in December 2014 are sorted and winnowed to a set of 174 unique basal icequake family templates by the following process: First, within each unstable slip event, waveforms of all basal icequake detections made at each back-projection gridpoint are cross correlated with each other and sorted into sets of similar detections by correlation coefficient. Highly correlated detections are repeats of the same family and are aligned and stacked, and less correlated detections are assigned as different families within the same gridpoint. This produces a few preliminary basal icequake family templates from each grid point, resulting in a few hundred preliminary templates per unstable slip event, or 6451 preliminary templates for all 18 unstable slip events.

At this point, many preliminary templates are still mis-detections from the back-projection in Chapter 3. Back-projection mis-detections result when arrivals from two or more different families are associated by the back-projection. When one of these templates containing arrivals from several families is cross correlated with the entire slip event in which it originated, the pattern of detection times is similar to that of both of the families from which the arrivals were mis-associated. I exploit this overlap in detection time similarity to remove many of the templates generated from back-projection mis-detections in the following way: All preliminary templates are cross correlated with the unstable slip event from which they are generated, and I calculate the number of detections in 20 second increments for each preliminary template, which I call the "detection time function". Then, within each unstable slip event, I cross correlate the detection time function of each preliminary template with all other binned detection time functions and sort

them into groups by correlation coefficient (Figure 4.3). Within each group of icequake families with similar detection times, I then retain only the template generated from the largest number of back-projection detections, which is most likely to be an authentic basal icequake template and not a mis-detection. After this step, for each icequake template, I again align all cross correlation detections with a high correlation threshold and stack them to produce the final templates. This step reduces the number of preliminary templates per slip event from several hundreds to several tens.

At this point, there are a few tens of basal icequake templates for each unstable slip event. I manually remove any remaining templates that are obviously of poor quality (ex., high noise levels, multiple arrivals on the same channel, or clearly resemble another template), resulting in a final set of 174 templates, corresponding to 174 repeating basal icequake families.

Cross correlation to detect repeating basal icequakes

I then cross correlate these 174 final templates with seismic data from the unstable slip in which they originate, from 15 minutes before the GPS-determined unstable slip initiation to 45 minutes after slip has started. Icequakes are detected where the network stacked cross correlation coefficient is greater than 9 x the median absolute deviation of the network stacked correlation function; this threshold is determined by trial and error to maximize high quality detections and minimize mis-detections.

Subset and refinement of high quality detections

For the analysis below, I look at a subset of 98 basal icequake families with more than 40 detections per unstable slip event, as a way of focusing on the

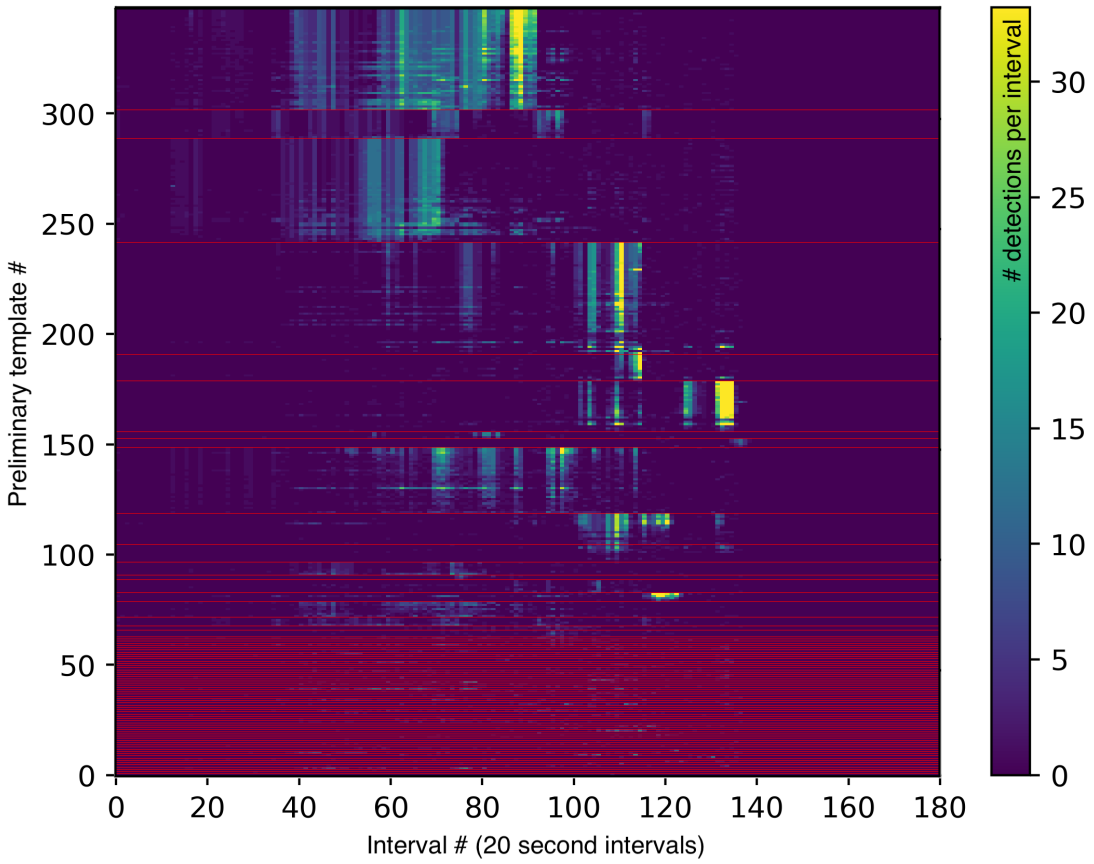

Figure 4.3: Detection time functions, or number of basal icequakes detected per 20 second interval, for the 349 preliminary templates generated from the back-projection catalog for unstable slip 6. Each row is the detection time function for a single preliminary template. All detection time functions are cross correlated with each other and sorted by correlation coefficient to determine basal icequake templates that share arrivals from multiple basal icequake sources. Horizontal red lines separate clusters of similar detection time functions, sorted by the number of back-projection detections that were used to generate each preliminary template. For each cluster, the template generated from the most back-projection detections is assumed to be the real template, and others are discarded. This results in 96 templates, which are then manually narrowed to 11 very high quality template events for slip number 6.

basal icequake families that dominate the seismicity signal of each slip event. A number of these families still contain mis-detections at low correlation coefficient. I eliminate low correlation coefficient mis-detections manually for each family in the following way: For each of these high quality basal icequake families, I plot all detections in order of descending correlation coefficient and determine a family-unique correlation coefficient cutoff threshold. I found that each family required a unique correlation threshold, which I chose as the threshold at which detection waveform similarity deteriorates. The resulting dataset of high quality detections contains 98 unique families of basal icequakes, and a total of 16,742 basal icequake detections from 18 unstable slip events occurring over 14 days.

All seismic data processing is done using the python package ObsPy (*Beyreuther et al.*, 2010; *Megies et al.*, 2011; *Krischer et al.*, 2015), and cross correlations are done using EQCorrScan (*Chamberlain et al.*, 2017).

4.2.2 GPS data

GPS data throughout this chapter were recorded on the GPS site shown in Figure 3.2a at 15 second intervals. Raw data are processed to latitude, longitude, and vertical positions using the Canadian Spatial Reference System Precise Point Positioning (CSRS-PPP) software available online from Natural Resources Canada. I convert latitude and longitude to polar stereographic (PS) coordinates using the Antarctic Mapping Tools package for MATLAB (*Greene et al.*, 2017), fit a line to the PS X and Y coordinates in map view, and rotate the position data into a downstream and transverse to flow reference frame. Downstream displacement data are then low-pass filtered below 300 seconds to reduce high frequency noise, as shown in Figure 4.4. GPS-determined ice sliding velocity is then calculated as the slope of a line fit by least squares to a running 4 sample (1 minute)

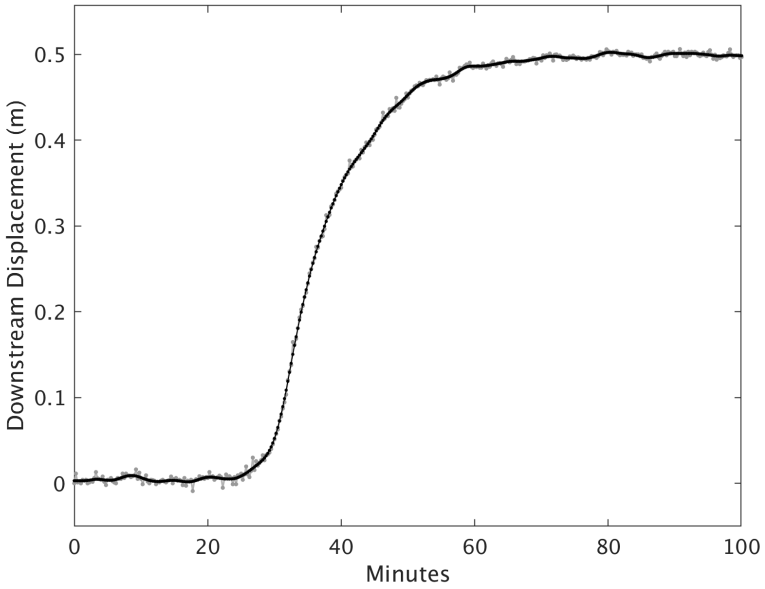

Figure 4.4: Example GPS data from an unstable slip event occurring at 10:50 on Jan 25, 2014. Light grey is the raw displacement data. Black data has been low-pass filtered below 300 seconds.

displacement window, assigned to the time of the 3rd sample. Both displacement and velocity are interpolated to 10 samples per second for comparison with basal icequake family behavior. These interpolated GPS data are upsampled to compare basal icequake family behavior to data that has a similar sampling interval, but because the GPS displacement data has been low pass filtered, any higher frequency fluctuations in velocity are missing.

4.3 Results

4.3.1 Icequake catalog: Overall patterns

The basal icequake catalog resulting from the cross correlation process described above contains 16,742 high quality icequake detections from 18 consecutive unstable slip events. Example repeating basal icequakes from Family 12 are

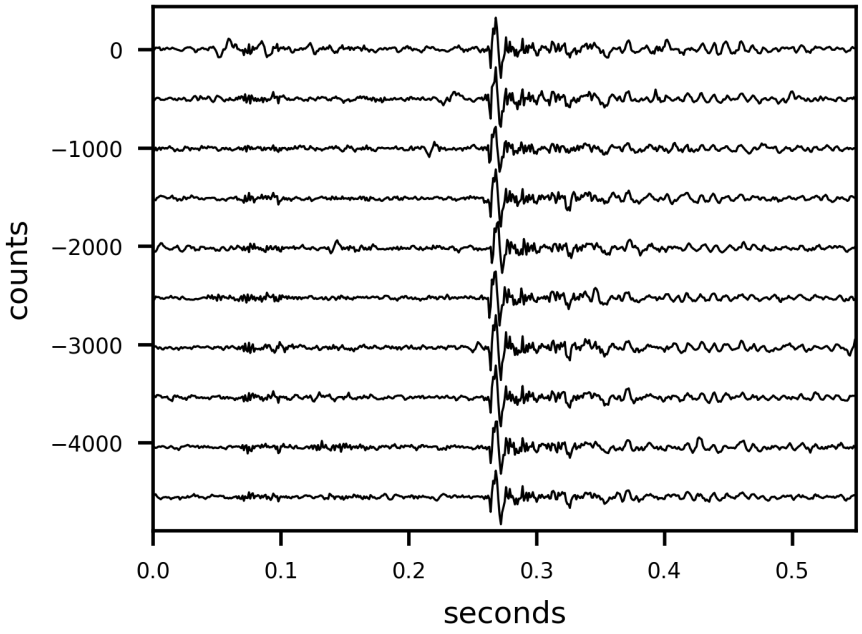

Figure 4.5: Ten repeat basal icequakes from Family 12 showing a high degree of waveform similarity between repeats. These data are from station WS15, east component, sampled at 1000 Hz.

shown in Figure 4.5, and have a high degree of waveform similarity. Key questions are addressed and observations are summarized about this dataset of basal icequakes below.

Where do repeating basal icequakes happen, and do these largest families of repeaters still occur in streaks?

The P- and S-wave arrival times on the final templates for each of the 98 basal icequake families are picked manually and re-located using the NonLinLoc earthquake location algorithm and a temperature-based seismic velocity model (described in Appendix B). Icequake family locations are shown in Figures 4.6 and 4.7. After re-location, most basal icequake locations remain within ~100 m of the back-projection location, with a few exceptions (Figure 4.6). After re-

location, the streaks of basal icequakes remain (Figure 4.7), but appear sparser, suggesting that the streaks are defined partly by families of repeating icequakes with fewer than 40 detections per slip event. Re-located icequake families occur near the base of the ice. Uncertainty in ice column wavespeed and ice thickness preclude confident re-location of icequakes to the ice base, but location depths are consistent with icequake sources at the base of the ice.

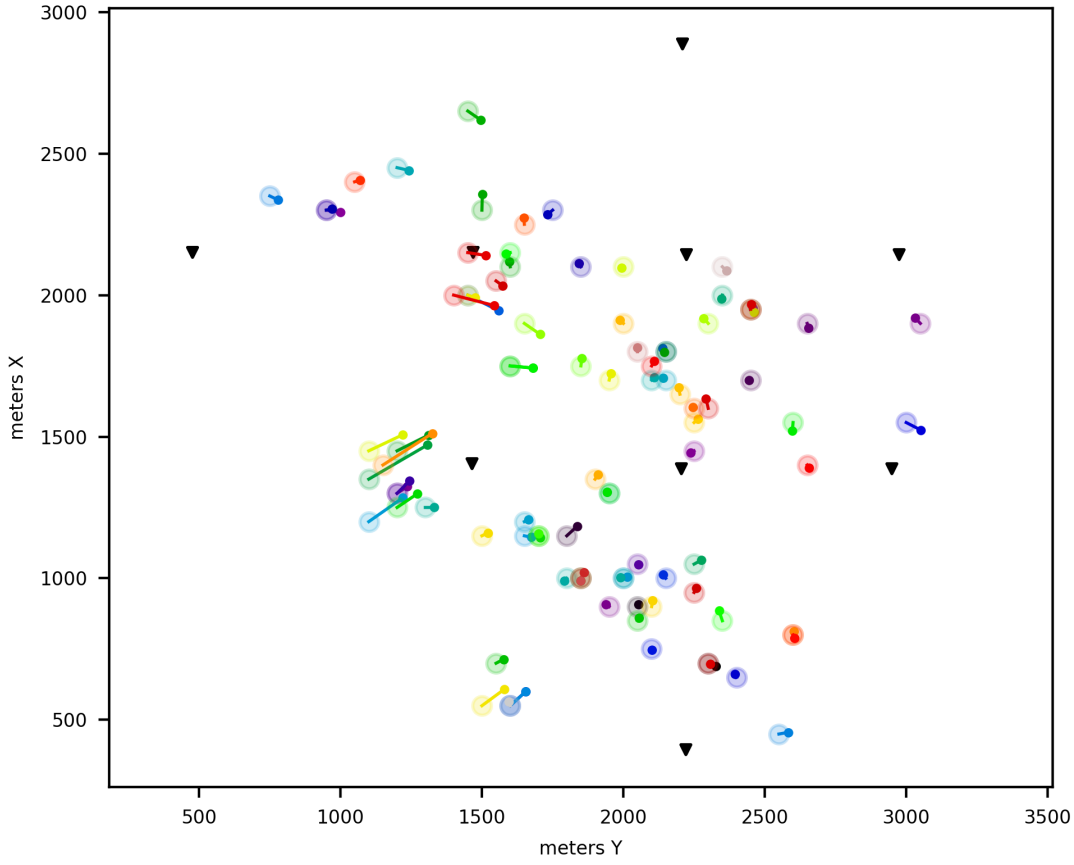

Figure 4.6: NonLinLoc icequake family locations compared with original back-projection locations. Black triangles are seismometer locations. Large circles represent original back-projection locations of each basal icequake family. Small circles are the new NonLinLoc locations. Original and new locations are colored the same and connected by a line. Most icequake family locations moved by less than 100 m.

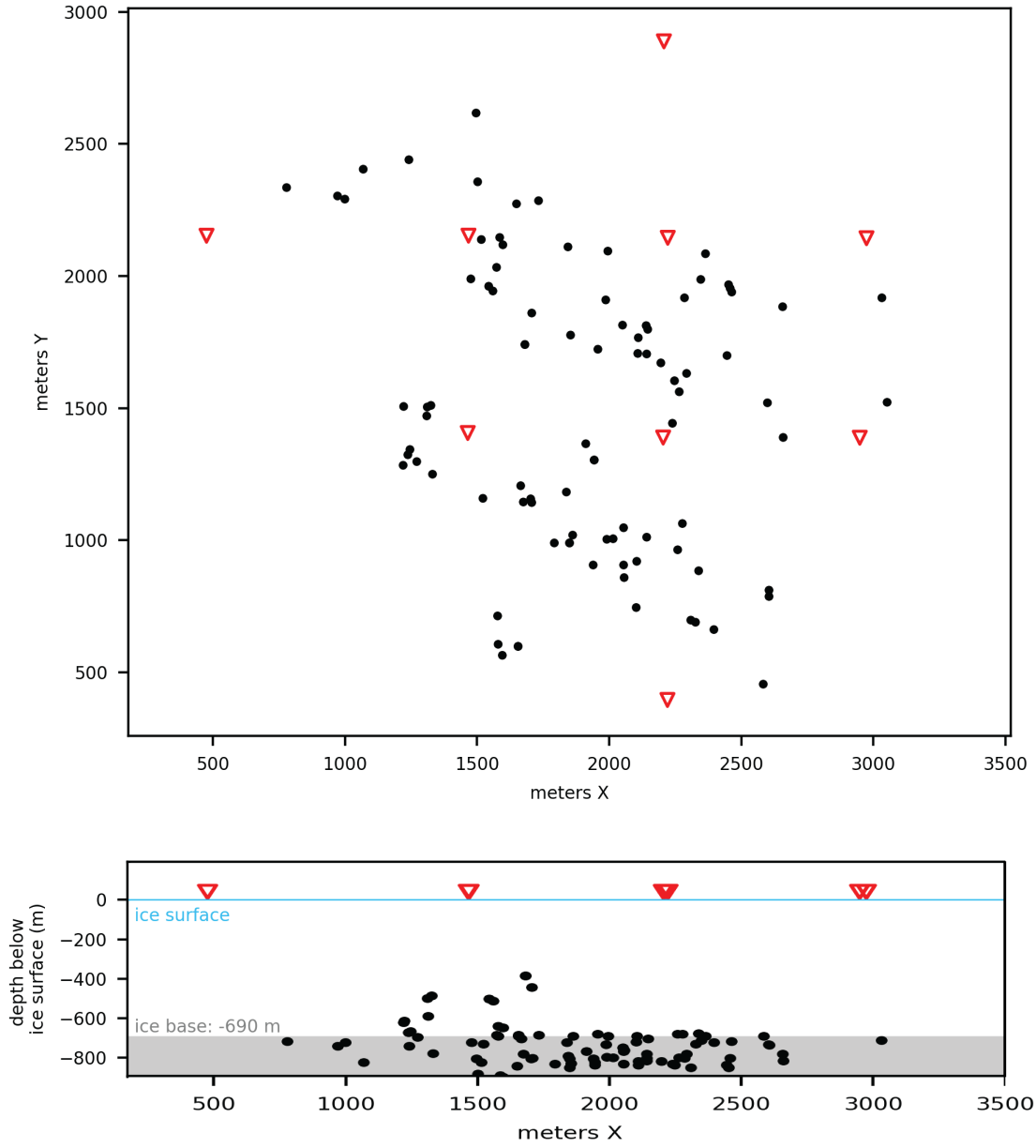

Figure 4.7: Top: Black dots are NonLinLoc locations for each icequake family. Red triangles are seismometer locations. Streaks of seismicity are still apparent. Bottom: Cross section showing that icequakes locate preferentially near the ice base.

When do basal icequakes happen within the WIP stick-slip cycle, neglecting family distinctions?

Figure 4.8 shows all 18 unstable slip events in the dataset. The black line in each panel shows the GPS-determined ice velocity. Bars show the number of basal icequakes per 30 second interval, with each family of repeating basal icequakes within each unstable slip colored differently. Colors that are continuous in this figure do not indicate that icequake families are continuously active between unstable slip events.

Figure 4.8 shows that there is no consistent relationship between the number of basal icequakes detected per interval and the phase of the stick-slip cycle: Sometimes the highest rate of icequakes per interval is when the ice sliding velocity is highest, but sometimes the highest rate occurs when the ice has slowed significantly. This shows that there is no simple relationship between the total number of icequakes per interval and the ice velocity. However, Figure 4.9 does show that the highest possible icequake rate does increase as the ice velocity increases, suggesting that the upper limit on icequake rate is determined by the ice sliding rate.

The total number of icequakes detected per unstable slip event is not correlated with either the maximum velocity per unstable slip event (which correlates with total ice slip during the event) or the elapsed time since the previous unstable slip event (Figure 4.10A,B). This means the simple metric of number of icequakes is not consistently correlated with how far the ice slides in a single unstable slip event, how fast it slides, or how much healing has occurred.

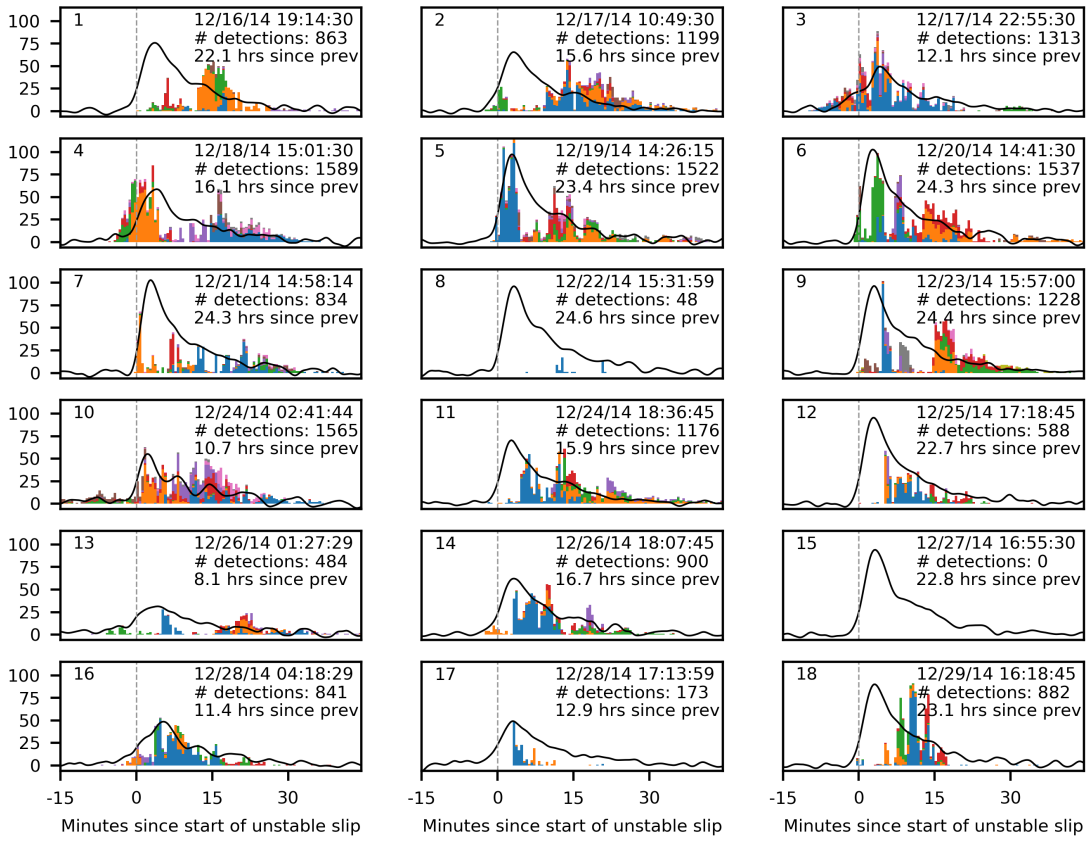

Figure 4.8: Number of icequakes detected per 30 second interval for all 18 unstable slip events in the dataset. Colors are chosen so that basal icequake families are distinguishable within each slip event; colors are not continuous between consecutive unstable slips. The y-axis is both ice slip velocity from on-ice GPS in m/day and the number of icequakes detected per 30 seconds. Vertical dashed grey line is the unstable slip initiation time determined by GPS velocity thresholding. Number in upper left corner is the slip number.

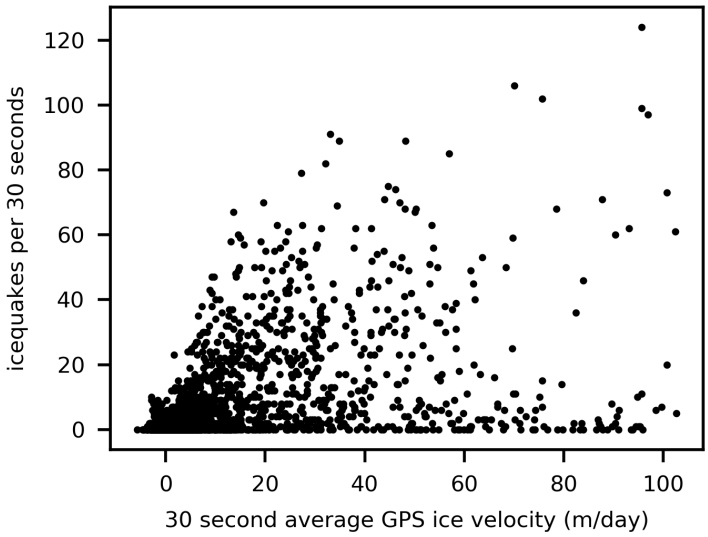

Figure 4.9: Total number of icequakes per 30 seconds as a function of GPS-determined ice sliding velocity for the entire icequake dataset, neglecting family distinctions. The largest number of basal icequakes per 30 seconds occurs at high slip velocities, but high slip velocities do not always have the most basal icequakes.

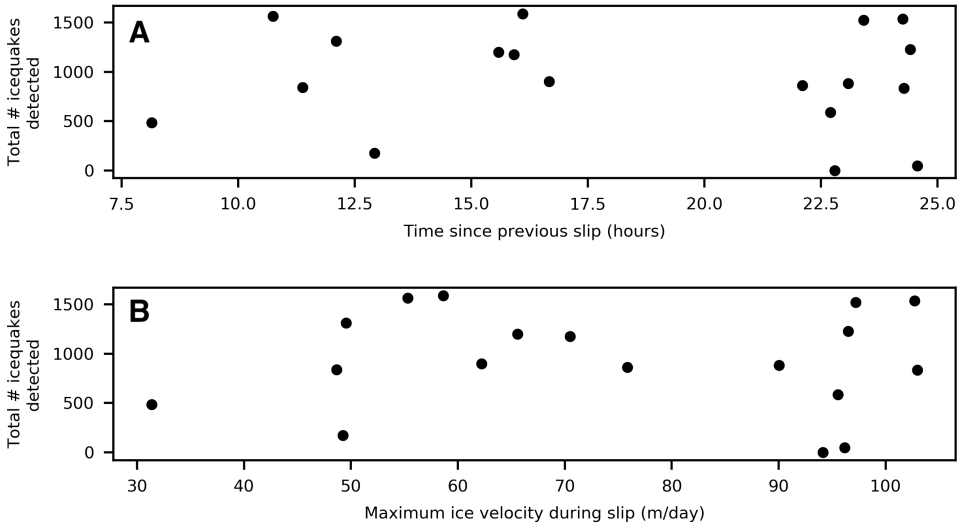

Figure 4.10: Total number of icequakes detected within each slip event as a function of the maximum ice velocity during slip (A) and the elapsed time since the previous unstable slip event (B). Maximum ice velocity is correlated with total slip distance within an unstable slip event. No pattern is seen here.

Precursory seismicity

Another important pattern is apparent in Figure 4.8: Precursory seismicity, occurring for several minutes before GPS ice velocity begins to rise, occurs only for slip events with fewer than ~16 hours of time elapsed since the start of the previous unstable slip event. In other words, unstable slips with a shorter healing time since the previous unstable slip event have more precursory seismicity. This observation may be evidence of immature healing of the ice base, and is discussed further in Section 4.3.8 below.

4.3.2 Behavior of icequakes within individual families of repeating events

Over these 18 unstable slip events, a total of 16,742 basal icequakes are detected in 98 families. Figure 4.11 shows the distribution of how many detections are in each of the 98 icequake families. More than half of all basal icequakes occur in families with fewer than 80 detections per family, shown in Figure 4.11A. This is an important point, that although for much of this chapter I discuss icequake families with many detections because they show the most clear patterns, the majority of icequake families have relatively few detections.

Families of basal icequakes are typically active for only a portion of the time during which the GPS can detect ice sliding (Figure 4.8). They typically turn on, last for a few cm of ice sliding, and then turn off. There is no consistent pattern in icequake family occurrence timing relative to the unstable slip, though a number of the unstable slips contain families active only in the first few minutes of sliding, during the acceleration phase, and other families that activate only after a few cm of sliding and last for the ice deceleration phase. This distinction in icequake family activation timing may reflect an evolution distance over which the basal

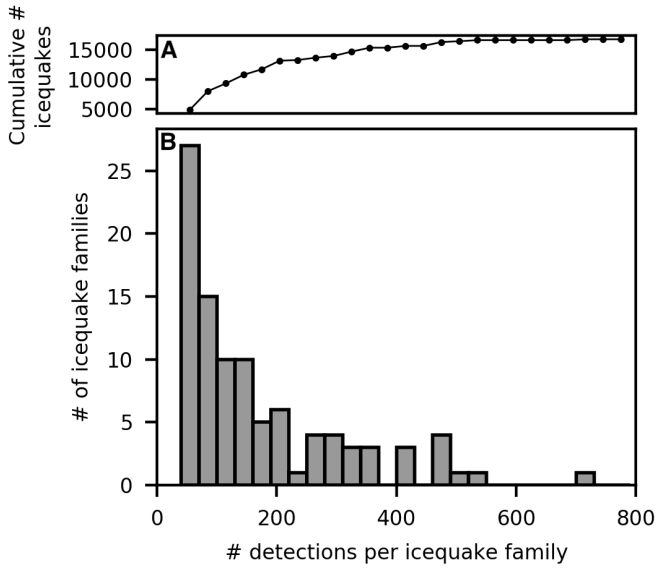

Figure 4.11: A: Cumulative number of basal icequakes contained in each bin in B, illustrating that more than half of the 16,742 basal icequakes detected occur in families with fewer than 80 detections. B: Histogram of how many basal icequake families have the given number of detections.

environment adapts to a faster sliding velocity.

Some individual families of basal icequakes have much stronger relationships between ice sliding velocity and icequake characteristics than the dataset as a whole. In particular, icequake amplitude and inter-event time within a family are often, but not always, correlated with GPS ice sliding velocity. Figures 4.12–4.14 show six families of repeating icequakes, with the amplitude of the largest S arrival for each family and the inter-event time (time since previous icequake in that family) plotted as a function of both time and ice displacement from GPS. Figures 4.12–4.14 also plot S-wave amplitude amplitude and inter-event time as a function of GPS ice sliding velocity. S-wave amplitude scales overall with ice sliding velocity, but fluctuations in amplitude are superposed on the overall trend. Icequake inter-event time scales inversely overall with ice slip velocity, indicating that icequakes get closer together in time as the ice sliding speed increases. These

six families of icequakes are characteristic of many of the icequake families in the dataset, though there is a lot of variability.

Are icequake amplitudes correlated with GPS-determined ice sliding velocity?

Icequake amplitudes are measured as the absolute value of the largest shear wave arrival on the same channel for all detections. Amplitudes vary significantly over the lifetime of each icequake family. Amplitudes of early icequake detections within a family often begin low, increase with time, experience one or several fluctuations in amplitude, and then end low again. This fluctuating pattern may reflect the ice sliding atop basal material with variable roughness or variable frictional material properties. Many icequake families also have an overall correlation between icequake amplitude and ice sliding velocity, with the fluctuations in amplitude superposed on this correlation (ex., Figure 4.12A,B,C). This overall correlation between amplitude and sliding velocity suggests that icequake amplitude may be broadly driven by loading rate (ice sliding velocity), which in turn suggests the hypothesis that fluctuations in amplitude may be the signature of local fluctuations in basal sliding velocity above and below the low-pass filtered velocity observed by GPS at the ice surface. Further interpretation of the significance of amplitude fluctuations are included in later sections.

Are icequake inter-event times correlated with GPS-determined ice sliding velocity?

Icequake inter-event times are generally inversely correlated with ice sliding velocity (e.g., Figure 4.12F), meaning faster sliding produces more icequakes per unit time within a family of repeaters. This suggests that basal icequakes rates

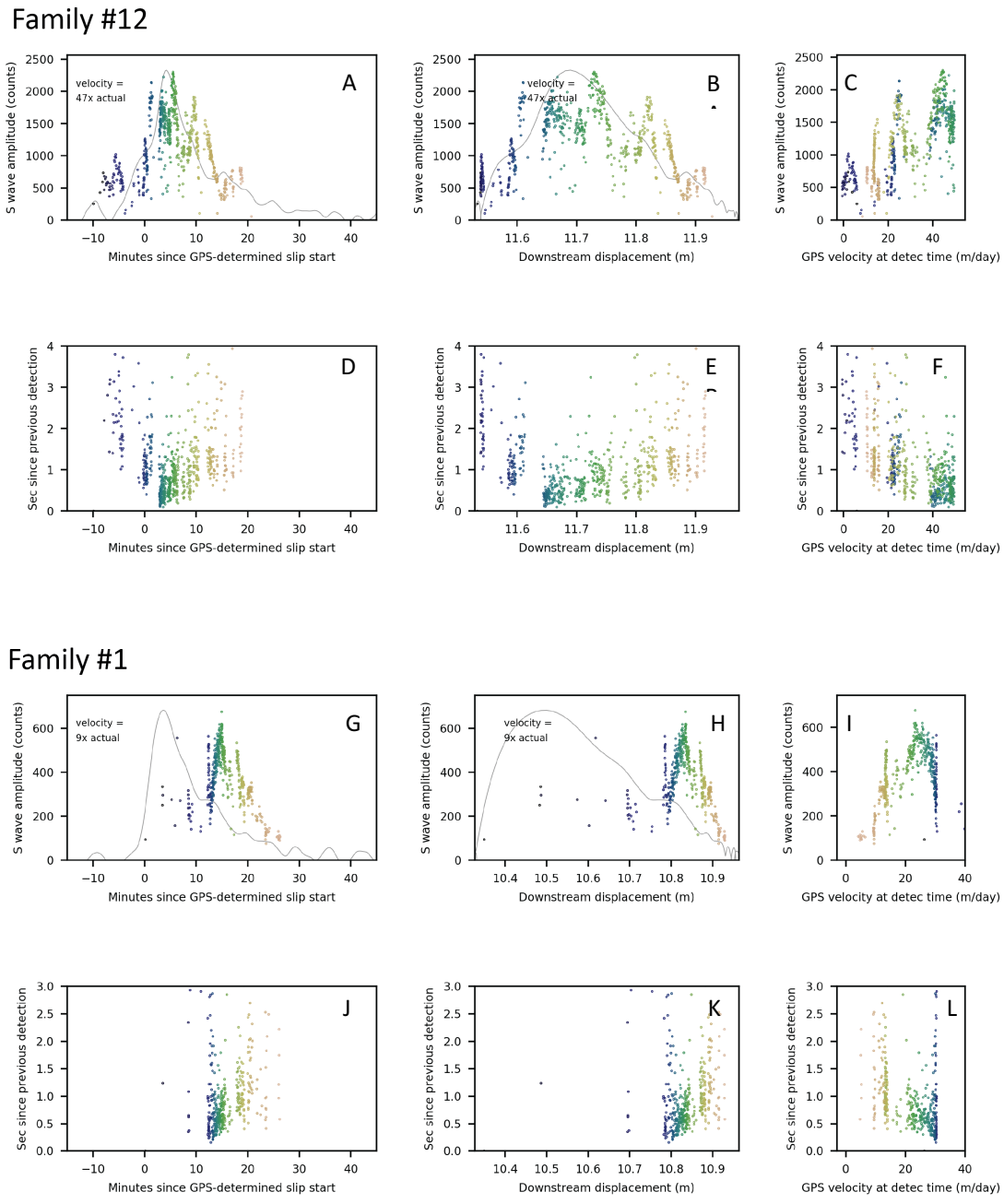

Figure 4.12: Two characteristic basal icequake families: Basal icequake S-wave amplitudes (top row) and recurrence times (bottom row) as a function of time since slip start (left), ice displacement (middle), and corresponding ice sliding velocity from GPS. Dot colors for each family correspond to time in upper left plot and are the same for each detection in each plot.

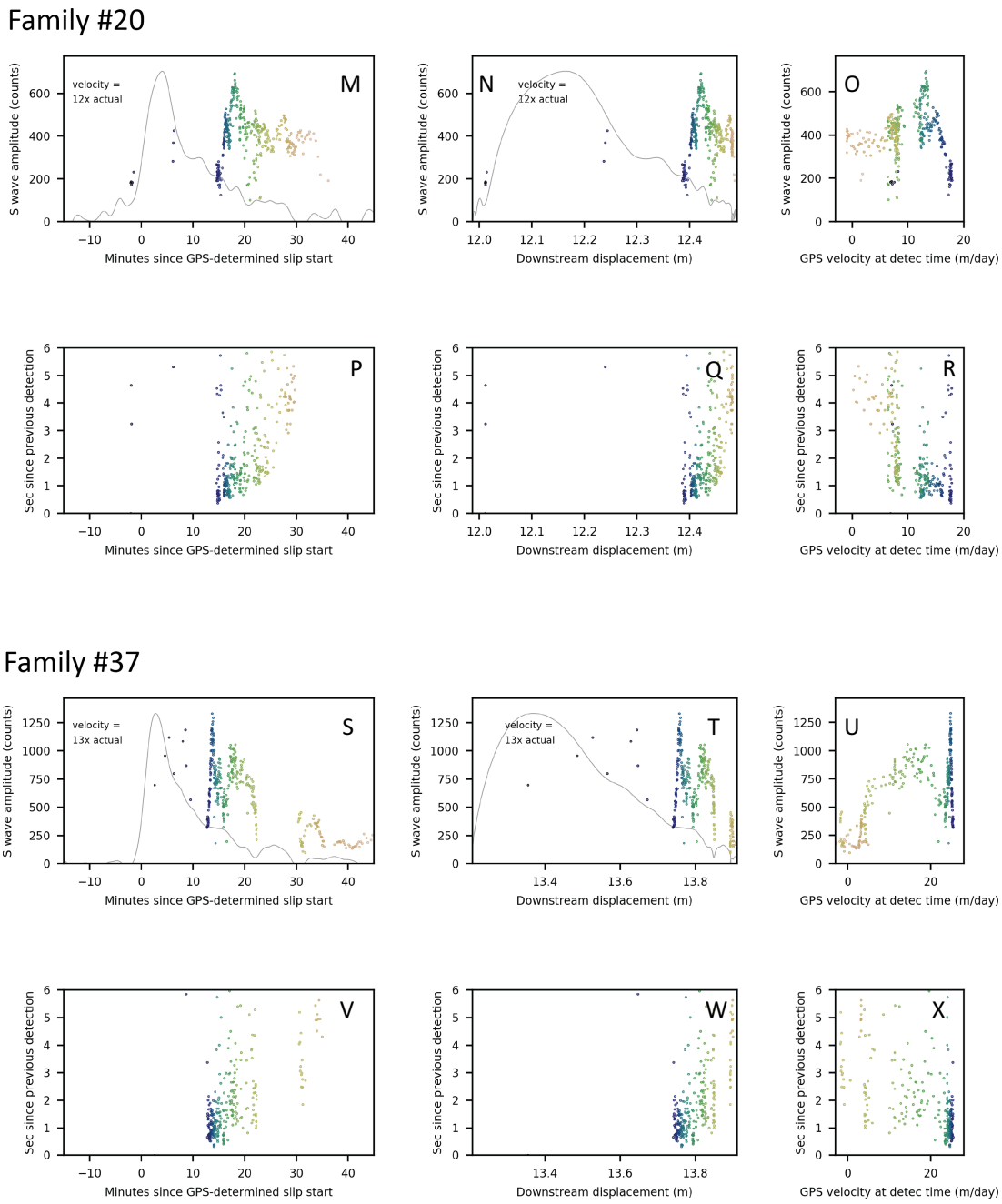

Figure 4.13: Two characteristic basal icequake families: Basal icequake S-wave amplitudes (top row) and recurrence times (bottom row) as a function of time since slip start (left), ice displacement (middle), and corresponding ice sliding velocity from GPS. Dot colors for each family correspond to time in upper left plot and are the same for each detection in each plot.

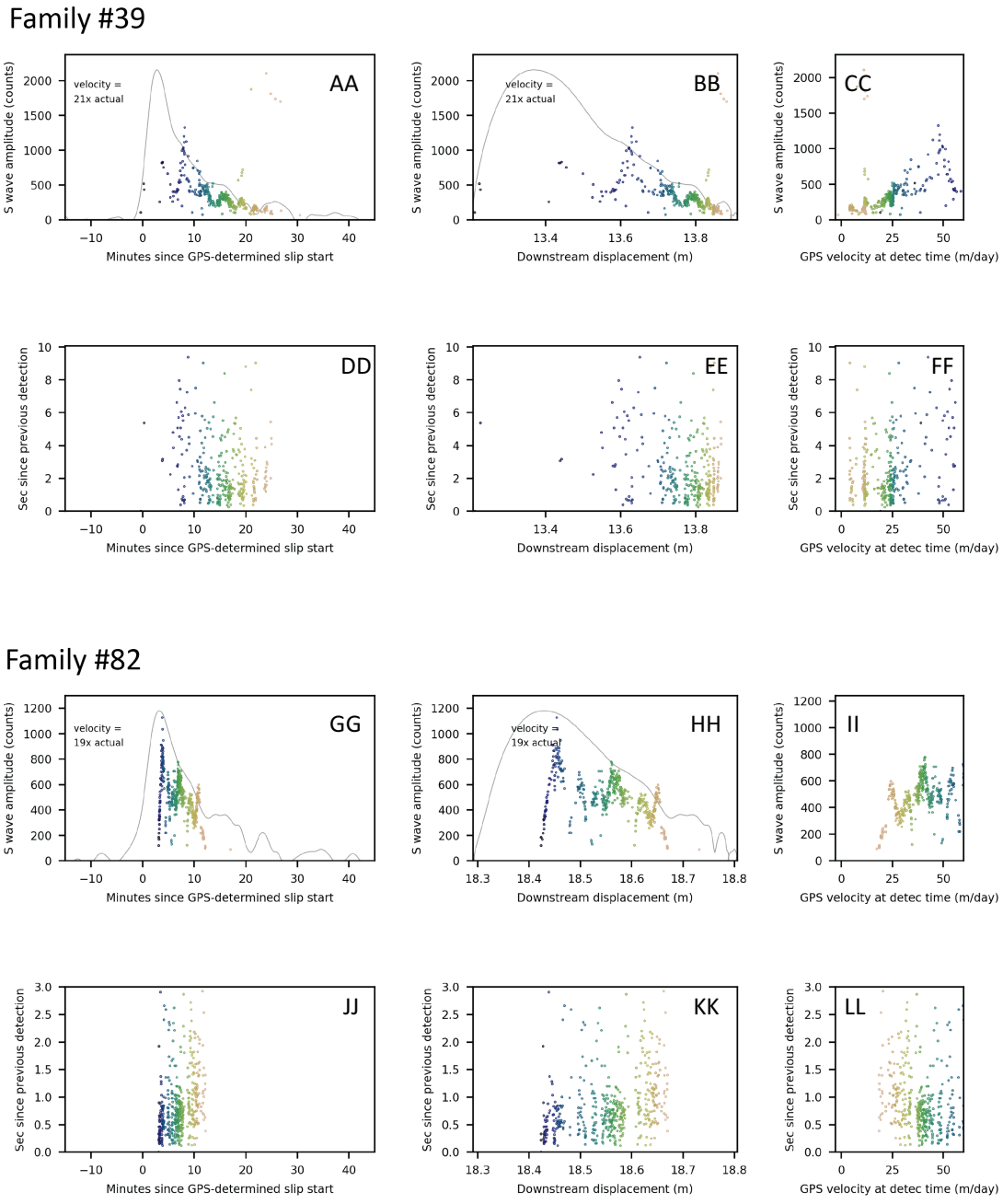

Figure 4.14: Two characteristic basal icequake families: Basal icequake S-wave amplitudes (top row) and recurrence times (bottom row) as a function of time since slip start (left), ice displacement (middle), and corresponding ice sliding velocity from GPS. Dot colors for each family correspond to time in upper left plot and are the same for each detection in each plot.

within a family are sometimes related to the loading rate, with faster ice sliding causing more icequakes per minute in a relatively predictable way. The lack of correlation between total number of icequakes per 30 seconds and sliding velocity discussed in Section 4.3.1 likely reflects that icequake families rarely persist for an entire unstable slip, and the unpredictable start and stop times affect the overall correlation for the entire dataset.

4.3.3 Estimates of basal icequake patch size

What are typical basal icequake magnitudes, rupture areas, and stress drops?

I performed spectral analysis of four of the largest and best observed basal icequake events to estimate seismic moment, rupture dimensions, and stress drop of the largest icequake sources. The frequency spectrum of an earthquake is related to the amount of slip and dimensions of the slip surface. In general, the form of a displacement spectrum model is (*Abercrombie*, 1995):

$$\Omega(f) = \frac{\Omega_0 e^{-\left(\frac{\pi f t}{Q}\right)}}{\left[1 + \frac{f}{f_c}^{\gamma n}\right]^{\frac{1}{\gamma}}} \tag{4.1}$$

where $\Omega(f)$ is the frequency spectrum, Ω_0 is the low frequency amplitude, f is frequency (Hz), f_c is the corner frequency, Q is the frequency independent quality factor, n is proportional to the high frequency falloff rate, γ is a constant controlling corner sharpness, and t is travel time. If attenuation $(1/Q)$ is assumed to be zero or corrected for independently, then $e^{-\left(\frac{-\pi f t}{Q}\right)}$ simplifies to 1. The classic *Brune* (1970) model assumes $n = 2$, $\gamma = 1$, and $t = 0$, though some workers tune n and γ to the specific shape of the source spectra in question (e.g. *Abercrombie*, 1995).

I compute moment using P waves from four high-amplitude basal icequakes from four different icequake families. I use P waves because the P wave corner frequency is well within the frequency resolution of the 1000 Hz data, while S wave corner frequencies, which are lower, are at the lower edge of the frequency resolution. Four basal icequakes with clear vertical P wave arrivals at two or three seismic sites are extracted and instrument-corrected to units of m/s using the obspy.signal.simulate package with the RESP files generated from an antelope database. For each arrival in each basal icequake, I take the velocity spectra and integrate in the frequency domain to displacement. I then average the spectra from the different stations to account for the radiation pattern, and I fit the average P-wave displacement spectra using a nonlinear least squares regression of the portion of the averaged spectrum below 350 Hz. Once the displacement spectra is fit, seismic moment M_0 is calculated as (*Brune*, 1970):

$$M_0 = \frac{4\pi\rho V_p^3 R\Omega_0(Z)}{U_{\phi\theta}} \tag{4.2}$$

where ρ is density, V_p is P wave velocity, R is the source-receiver distance, $\Omega_0(Z)$ is the low frequency amplitude of the average vertical (Z) component P wave spectra, and $U_{\phi\theta}$ is the mean radiation pattern coefficient ($U_{\phi\theta} = 0.52$) (*Aki and Richards*, 2002) . Moment magnitude is then calculated as (*Hanks and Kanamori*, 1979):

$$M_w = \frac{2}{3}\log_{10}(M_0) - 6 \tag{4.3}$$

I assume a circular crack model (*Madariaga*, 1976) for simplicity. Stress drop is highly model dependent, and these results are meant to be an order of magnitude estimate of rupture areas. According to *Madariaga* (1976), the radius of a circular

fault is determined using P wave spectra as:

$$r = 0.32\frac{V_s}{f_c} \tag{4.4}$$

and rupture area $A = \pi r^2$. This result can then be used to estimate a stress drop ($\Delta\sigma$) for each event (*Eshelby*, 1957):

$$\Delta\sigma = \frac{7}{16}\frac{M_0}{r^3} \tag{4.5}$$

I also estimate displacement D on the fault during each icequake as:

$$D = \frac{M_0}{\mu A} \tag{4.6}$$

where μ is the shear modulus of ice or till.

I calculate M_0, M_w, r, A, $\Delta\sigma$, and D for the averaged spectra for each of the four basal icequakes. Waveforms and spectra are shown in Figure 4.15 and results are summarized in Table 4.2. Because I do not necessarily know whether a basal icequake occurs in the till, on the ice-till interface, or in the basal ice, I calculate M_0, M_w, r, A, $\Delta\sigma$, and D assuming properties of an ice-ice fault and a till-till fault, bracketing possible rupture dimensions and stress drops. I assume most ice and till properties from *Luthra et al.* (2016). Till properties from *Luthra et al.* (2016) are from amplitude versus offset active seismic experiments, which estimate till properties for material within ~1/4 wavelength of seismic wave penetration into the till, which Luthra et al. (2016) estimate to be ~1.5 m. These estimates therefore are for the till properties in the top ~1.5 m of till. This means the wavespeed and shear modulus are probably higher for this ~1.5m m thick layer than for any thin deforming layer of surface till, and also the wavespeed and shear

modulus are probably lower than deeper, more consolidated layers of till.

I find seismic moment M_0 falls in the range of 6-16 x 10^6 Nm for an ice-only fault, and 0.7-1.8 x 10^6 Nm for a till-only fault, both of which are order-of-magnitude consistent with estimates of basal icequake moment from the upper Whillans Ice Stream (*Anandakrishnan and Bentley*, 1993), the Kamb Ice Stream (*Anandakrishnan and Alley*, 1994), the Rutford Ice Stream (*Smith et al.*, 2015), and from the western margin of the Greenland Ice Sheet (*Roeoesli et al.*, 2016). These values of M_0 correspond to moment magnitudes of $M_w = -1.47$ to -1.20 for ice-only and $M_w = -2.11$ to -1.83 for till only faulting. Corner frequencies for these four icequakes vary between 105 and 196 Hz, corresponding to rupture areas of approximately 30-100 m^2 and 0.8-2.8 m^2 for ice-ice and till-till faulting respectively. Corresponding stress drops are low for ice-ice faults: $\Delta\sigma = 30 - 100$ kPa, and high for till-till faults: $\Delta\sigma = 1.1 - 7.2$ MPa. This extremely high till-till value for stress drop suggests the faults are not happening on till-only faults, unless the till is much stiffer.

An actual basal icequake fault likely occurs near the ice-till interface, and basal icequakes likely have properties intermediate between these estimates: seismic moment in the range of $1 - 10 \times 10^6$ Nm, moment magnitude in the range of $M_w = -2$ to -1, rupture areas of a few m^2, and stress drops of a few hundred kPa. The basal icequake patch diameter, discussed further below, is likely in the range of 1 to several meters for these four basal icequakes, which are among the largest and most clearly observed in the dataset. The majority of basal icequakes occur with smaller seismic moment and likely smaller rupture areas.

Ice-ice fault: Vp = 3840 m/s (Luthra et al., 2016) Vs = 1860 m/s (Luthra et al., 2106) mu = 3.664 GPa									
Family #	Obs station	low frequency amplitude (m)	corner frequency (Hz)	M0 (Nm)	Mw	Circular Crack Radius (m)	Circular Crack Area (m^2)	Stress Drop (Pa)	Displacement (m)
40	WS05	1.10E-11	105	1.390E+07	-1.24	5.669	100.95	3.339E+04	3.759E-05
52	WS05	5.10E-12	196	6.418E+06	-1.46	3.037	28.97	1.003E+05	6.046E-05
78	WS15	4.95E-12	132	6.228E+06	-1.47	4.509	63.87	2.972E+04	2.661E-05
92	WS15	1.28E-11	116	1.608E+07	-1.20	5.131	82.71	5.206E+04	5.305E-05

Till-till fault: Vp = 1840 m/s (Luthra et al., 2016) Vs = 310 m/s (Luthra et al., 2016) mu =20 Mpa (Lipovsky et al., 2016)									
Family #	Obs station	low frequency amplitude (m)	corner frequency (Hz)	M0(Nm)	Mw	Circular Crack Radius (m)	Circular Crack Area (m^2)	Stress Drop (Pa)	Displacement (m)
40	WS05	1.10E-11	105	1.530E+06	-1.88	0.945	2.80	7.213E+06	0.00015
52	WS05	5.10E-12	196	7.060E+05	-2.10	0.506	0.80	2.166E+07	0.00024
78	WS15	4.95E-12	132	6.852E+05	-2.11	0.752	1.77	6.420E+06	0.00011
92	WS15	1.28E-11	116	1.769E+06	-1.83	0.855	2.30	1.125E+07	0.00021

Table 4.2: Calculated properties of four characteristic basal icequakes assuming ice-ice and till-till faulting.

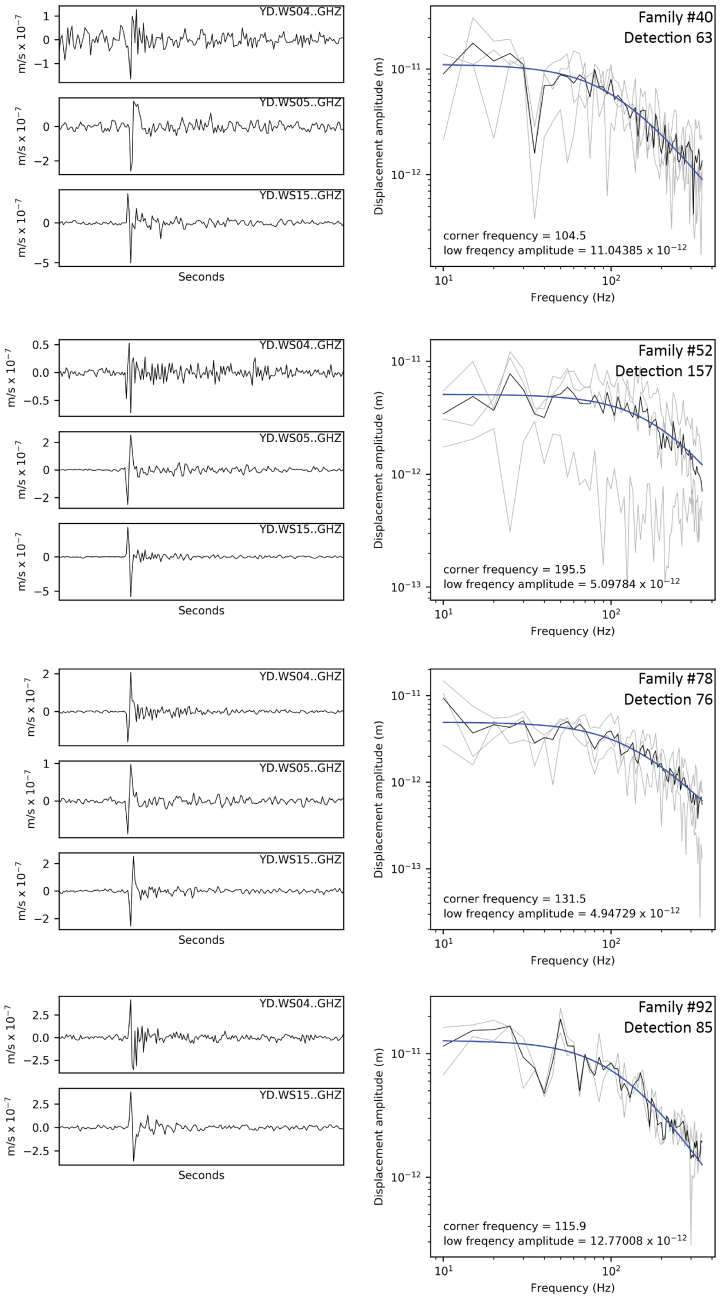

Figure 4.15: Four P wave spectral fits. Left: P wave arrivals from available vertical components in instrument corrected units of m/s; panels are 0.15 seconds. Right: Displacement spectra for each P wave (grey) and average spectra (black). Blue lines are least-squares fits of the Brune model ($n = 2$) to the average P wave displacement spectra in the range of 5-350 Hz.

Family numbers	Recur in slip numbers:	Total ice displacement between first and last detection (m)
52, 93, 95	9, 17, 18	5.6
59, 87	10, 16	3.58
69, 78	11, 13	1.4
6, 12, 30, 54	2, 3, 5, 9	4.98
36, 55	6, 9	2.81
24, 45	4, 7	2.54
14, 22	3, 4	0.5
11, 13	2, 3	0.65
29, 41	5, 6	1.39

Table 4.3: Table summarizing basal icequake families that recur in multiple slips.

Other estimates of basal icequake patch size: Active slip distance and amplitude fluctuation widths

Of the 98 basal icequake families, there are 9 families that recur in multiple unstable slip events, reducing the number of distinct families to 86. Figure 4.16 shows the same dataset as Figure 4.8, but with each family colored continuously, showing that several families recur later in the dataset. For example, family 59 (teal) occurs first in unstable slip 10, becomes aseismic, and then returns in unstable slip 16, 5 days later. The family that recurs over the largest amount of ice slip is family 52, which is active in unstable slip 9 (dark green), then again in slips 17 and 18, 5 days later. A total of 5.6 m of ice sliding occurs between the first and last detection in family 52. All recurring families and the ice slip distance over which they occur are summarized in Table 4.3. It is important to note that most of these recurring families are not consistently active, but instead turn off for periods of time between and during slip events before they turn back on again.

Within each unstable slip event, as mentioned above, an individual icequake family is only active for a portion of the unstable slip event, which I term the

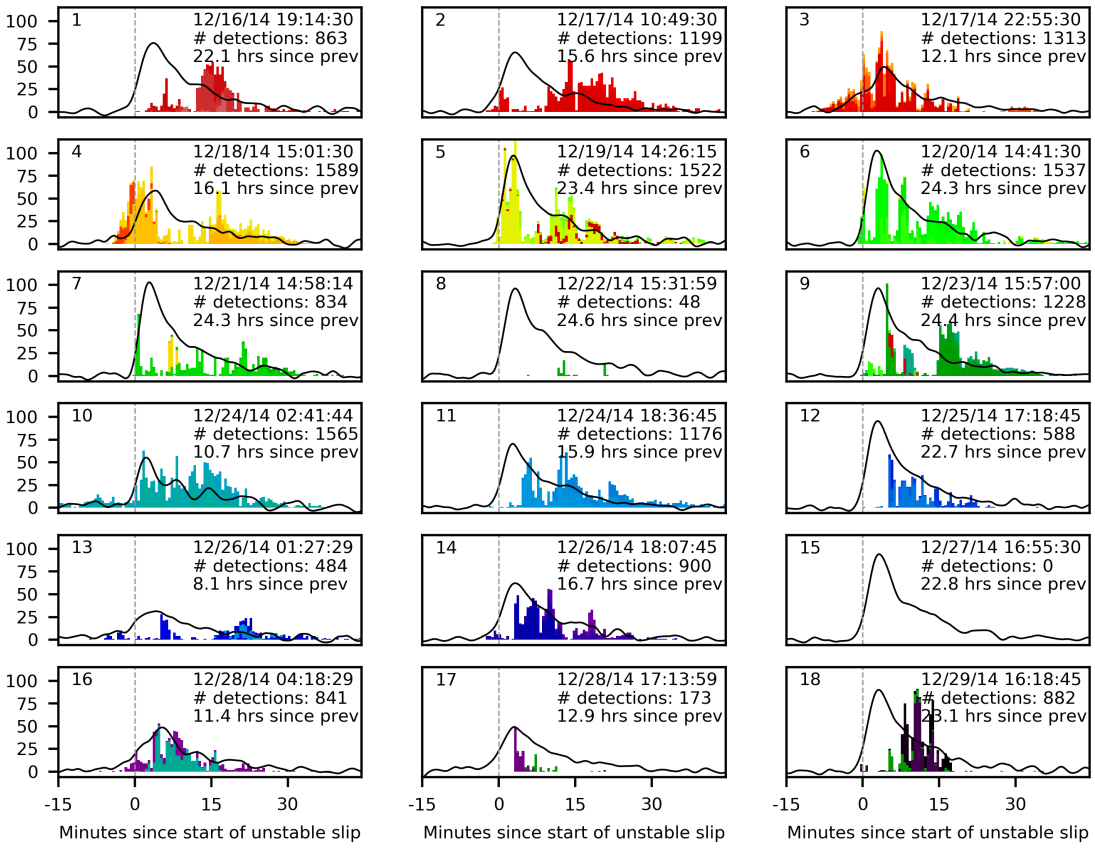

Figure 4.16: Same as Figure 4.8, but with icequake family colors continuous between unstable slip events, illustrating that some basal icequake families recur in subsequent unstable slip events.

icequake family "active duration" for the amount of time a family is active, and the "active slip distance" for the ice slip distance over which an icequake family is active. The active duration and slip distance for each icequake family are shown in Figures 4.17 and 4.18. Each vertical column is a different icequake family, and the colored bar represents the time (Figure 4.17) or ice slip (Figure 4.18) over which the icequake family occurred. Because the dataset contains some misdetections occurring at random times, data are refined to show the time or ice slip that occurred between the first detection with more than 10 detections in the next minute to the last detection with more than ten detections in the previous minute. Each bar therefore represents the time during which the icequake family is very active. Families are sorted by slip event, and slip events are sorted by elapsed time since previous unstable slip event. Bar colors signify icequake families in which more than 2/3 of events occur before peak ice velocity (orange), more than 2/3 of events occur after peak ice velocity (dark blue), or neither (light blue).

Figures 4.17 and 4.18 show that basal icequake families are active for variable amounts of time and variable amounts of slip, and that there is no single characteristic timescale or slip distance controlling icequake family activity. This is further quantified in Figures 4.19A and 4.19B, which show the active duration and active slip distance for each family as a function of healing time; this figure shows the lengths of the bars in Figures 4.17 and 4.18. Figures 4.19C and 4.19D show the distribution of active durations and active slip distances, showing that basal icequake families are active for durations of typically less than 20 minutes, and over slip distances of typically less than 0.5 meters, and most less than 0.2 meters. Though Figure 4.18 clearly shows the previously made observation that the ice slides further with larger time since previous unstable slip event (*Winberry et al.*, 2009a; *Walter et al.*, 2011), no other trend is obvious; there is no dominant

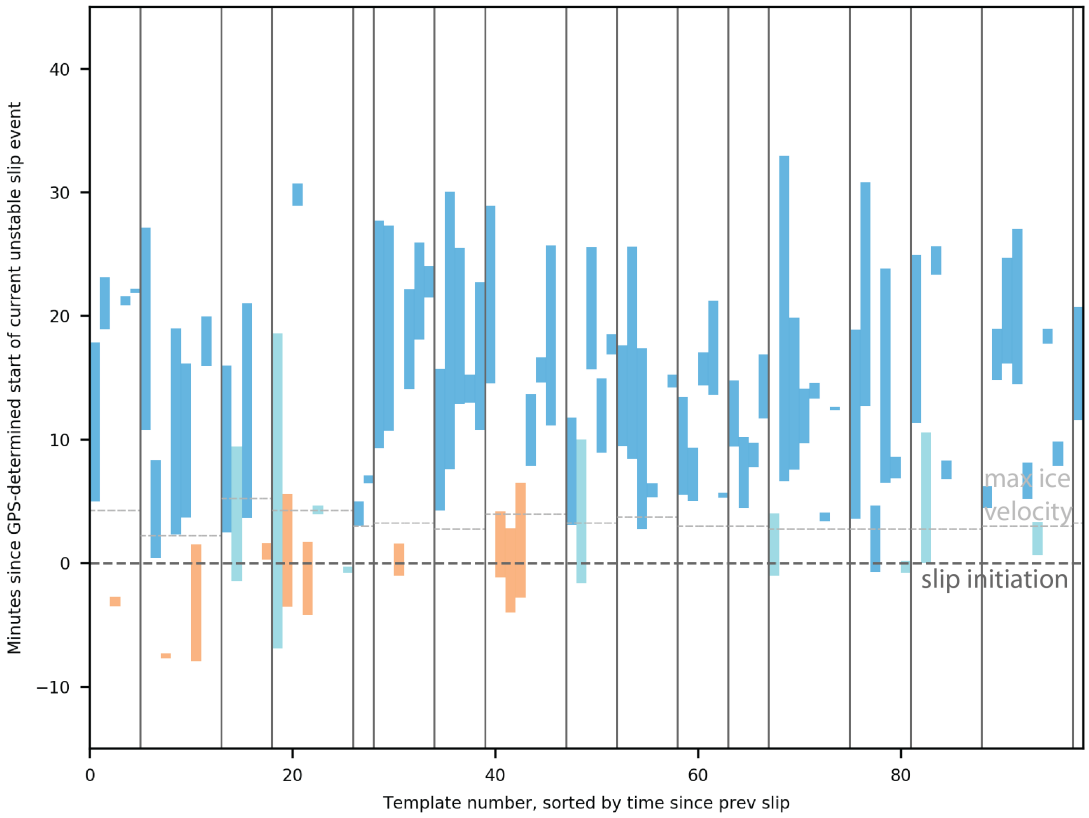

Figure 4.17: Time duration over which each basal icequake family is active. Each column is one of 98 basal icequake families, and the bar represents the time over which the family is active, from the first detection with more than 10 icequakes in the next minute to the last detection with more than 10 icequakes in the previous minute. These thresholds are chosen to reduce the number of time-isolated mis-detections and look at the time duration over which the families are most active. Dark grey dashed line is the GPS-determined slip nucleation time. Light grey dashed lines indicate the time at which the ice sliding velocity is highest; icequakes below the light grey dashed line occur during the slip acceleration phase, and icequakes above the light grey dashed line occur during the slip deceleration phase. Families are grouped by unstable slip event, separated by vertical dark grey lines. Unstable slip events are sorted left to right by increasing number of hours elapsed since previous unstable slip event. Orange indicates icequake families with more than 2/3 of detections occurring during ice acceleration before the maximum ice sliding velocity; dark blue indicates icequake families with more than 2/3 of detections occurring during deceleration after maximum ice sliding velocity; and light blue indicates that the icequake family meets neither criteria.

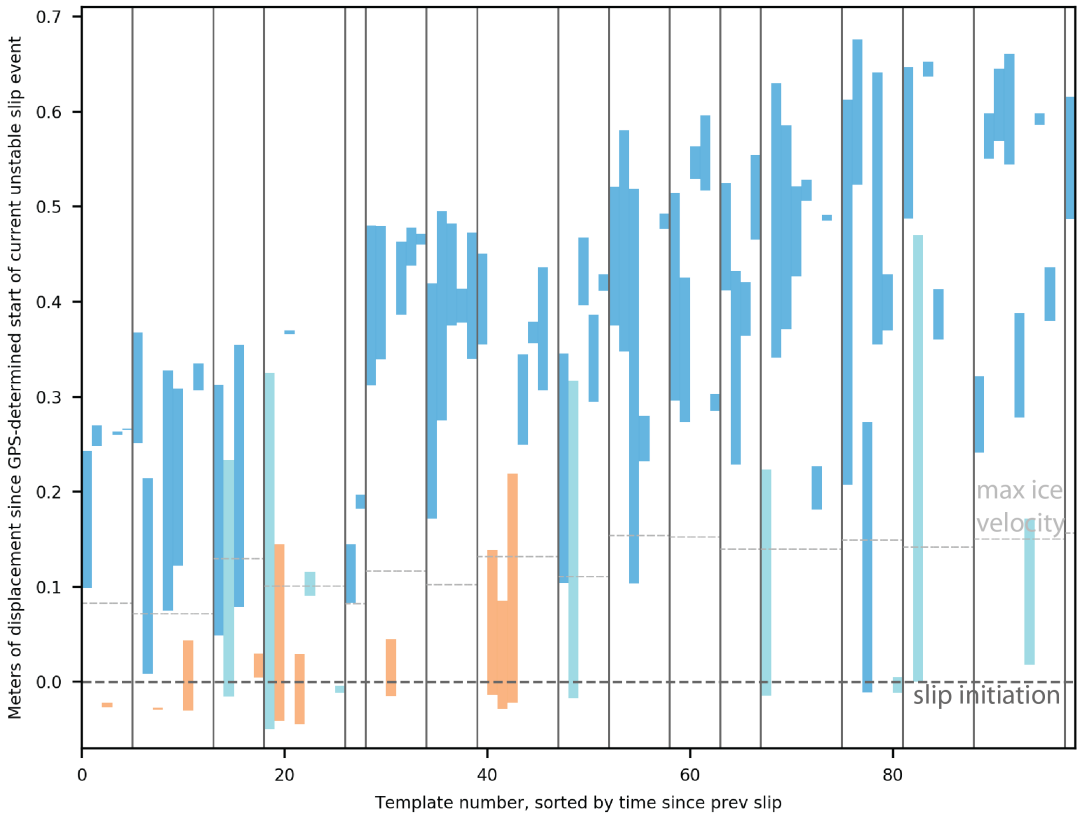

Figure 4.18: Slip distance over which each basal icequake family is active. Each column is one of 98 basal icequake families, and the bar represents the slip distance over which the family is active, from the first detection with more than 10 icequakes in the next minute to the last detection with more than 10 icequakes in the previous minute. These thresholds are chosen to reduce the number of time-isolated mis-detections and look at the slip distance over which the families are most active. Dark grey dashed line is the GPS-determined displacement value at the slip nucleation time. Light grey dashed lines indicate the displacement value at which the ice sliding velocity is highest; icequakes below the light grey dashed line occur during the slip acceleration phase, and icequakes above the light grey dashed line occur during the slip deceleration phase. Families are grouped by unstable slip event, separated by vertical dark grey lines. Unstable slip events are sorted left to right by increasing number of hours elapsed since previous unstable slip event. Orange indicates icequake families with more than 2/3 of detections occurring during ice acceleration before the maximum ice sliding velocity; dark blue indicates icequake families with more than 2/3 of detections occurring during deceleration after maximum ice sliding velocity; and light blue indicates that the icequake family meets neither criteria.

characteristic timescale or slip distance observed in any of these figures, or trend with time since previous unstable slip event.

Because the active duration of an icequake family is strongly modulated by the changing ice sliding velocity, I instead focus on the amount of ice sliding over which families are active, the active slip distance (Figure 4.18, 4.19B,D), which ranges between 0.02-0.5 m. If the active slip distance corresponds to the size of the basal icequake source patch, then there is no evidence of basal icequake patches changing size systematically with elapsed time since previous unstable slip event in this dataset. Nor is there one controlling patch size or amount of slip over which a single family of repeating basal icequakes take place. Basal seismicity appears to be dominated by families that only last for small amounts of basal sliding, typically less than 0.2 meters.

Interestingly, there is an approximately exponentially decreasing trend in the number of families that occur over an increasing ice displacement (Figure 4.19D), suggesting that there may also be an exponential distribution of icequake patch sizes at the ice base: Many more families occur over short amounts of ice displacement than occur over larger amounts of displacement. Two possible interpretations of this quantity, the active slip distance, are that it corresponds to either the width of outcrops of stiff over-consolidated till to the ice base, or the width of patches of debris-laden basal ice. Figure 4.19D suggests that there are many more small (~0.02m) outcrops of over-consolidated till or areas of dirty basal ice than larger (~0.5m) ones. This suggests a picture of the ice stream bed with a few large basal icequake patches and many smaller icequake patches within the streaked seismically active area beneath the ice, illustrated schematically in Figure 4.20.

Figures 4.17, 4.18, and 4.19A,B also show that families that occur primarily

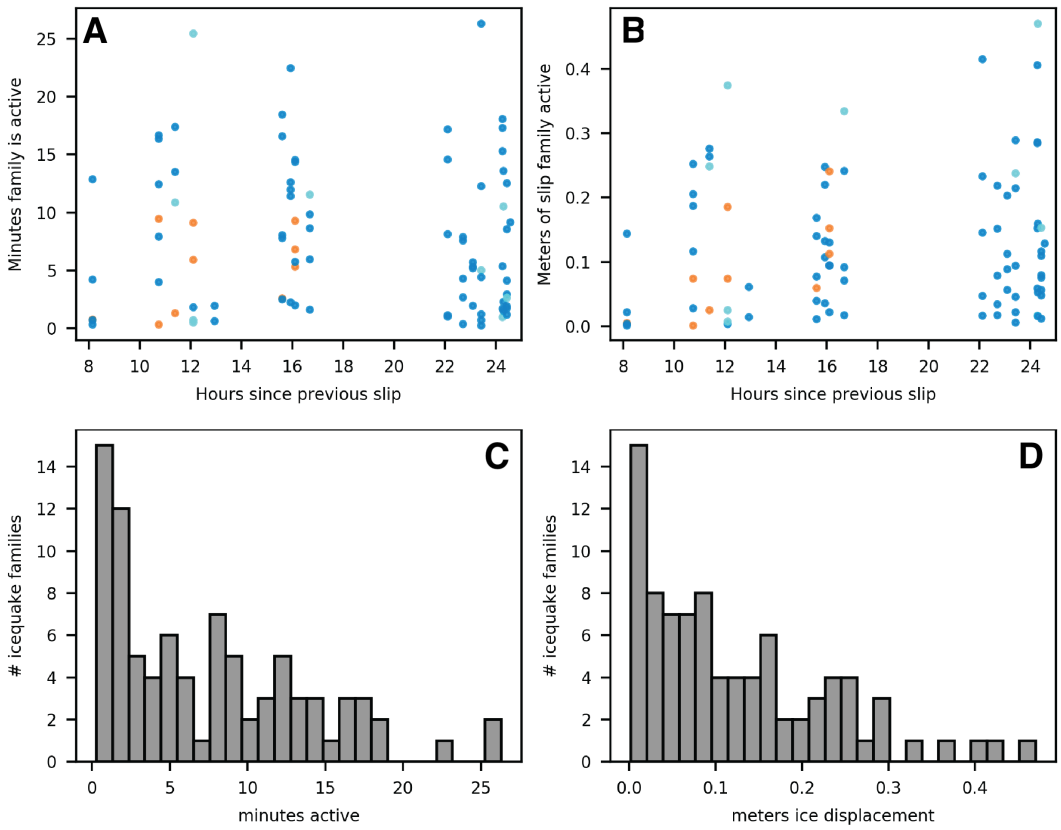

Figure 4.19: Top: Minutes (A) and slip distance (B) over which each icequake family is active. These plots show the length of individual bars in Figures 4.17 and 4.18. Active slip durations and distances are plotted as a function of elapsed time since previous unstable slip event. Colors correspond to Figures 4.17 and 4.18. Bottom: Histograms showing the number of basal icequake families active for a range of active slip durations (C) and active slip distances (D). Most icequake families last for short amounts of time or slip distance.

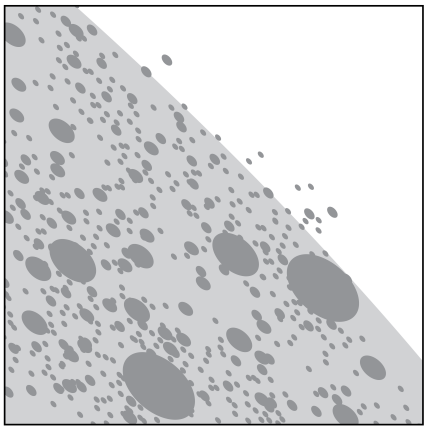

Figure 4.20: Schematic illustration of the distribution of basal icequake patch sizes suggested by the approximately exponentially decreasing number of families having larger active slip distances (Figure 4.19D). Dark grey areas are basal icequake generating patches of ice stream bed with few large patches and many small patches. The light grey area indicates the dimensions of a basal seismicity streak imaged in Chapter 3. The white area indicates the aseismic area surrounding a basal seismic streak from Chapter 3, where the basal interface does not experience seismogenic stick-slip.

early, before the peak ice velocity (orange bars and dots) occur only for short amounts of time elapsed since the previous unstable slip event, which may be a signal of immature basal healing between unstable slips, discussed further below. Neither early (orange) nor late (dark blue) icequake families have distinct controlling active durations or active slip distances (Figure 4.19A,B).

Do basal icequakes within a family of repeaters move over the course of a family lifetime?

Family 52 occurs first in slip 9, then again in slips 17 and 18, with 5.6 m of ice sliding between the first and last detection (Table 4.3). I now consider the effect of a 5.6 m change in icequake location relative to the seismometer locations on seismic phase arrival times.

Seismometer station spacing is 750-1000 m. Considering an icequake at the base of the ice that occurs at an epicentral distance (map view) of 500 m from a seismometer in 700m thick ice, the P wave travel time is 0.22402 seconds, and the S wave travel time is 0.46249 seconds, using typical P and S wave speeds of 3840 m/s and 1860 m/s, respectively (*Luthra et al.*, 2016). Moving the source 5.6 m farther from a seismometer along the basal interface results in travel time changes of 0.00085 seconds and 0.00176 seconds for the P and S waves, respectively, illustrated as the red and blue lines in Figure 4.21. Seismometer sampling rates are 1000 Hz, meaning the P wave travel time change for a 5.6 m change in location is approximately 1 sample, and the S wave travel time change is approximately 2 samples. This suggests that these icequake locations may be distinguishable with relative relocation methods, though the changes in location are at the edge of detectability. With the current dataset, I cannot distinguish if the source location of a recurring family of icequakes is static with respect to the bed, the ice, or neither.

Amplitude fluctuations: Width of fluctuations as a length scale of basal variability

An interesting pattern in this data is that, over the lifetime of a single basal icequake family, the amplitude of individual icequake detections fluctuates significantly (Figures 4.12, 4.13, 4.14). Here, I consider the possibility that the amplitude fluctuations may represent basal ice sliding across one or several basal icequake fault patches, with amplitude fluctuations resulting from changing area of basal ice to fault patch coupling as the ice traverses the patch. In this situation, the amount of ice sliding during an amplitude fluctuation from trough to trough would be an additional constraint on how wide a basal icequake patches is. Here, I

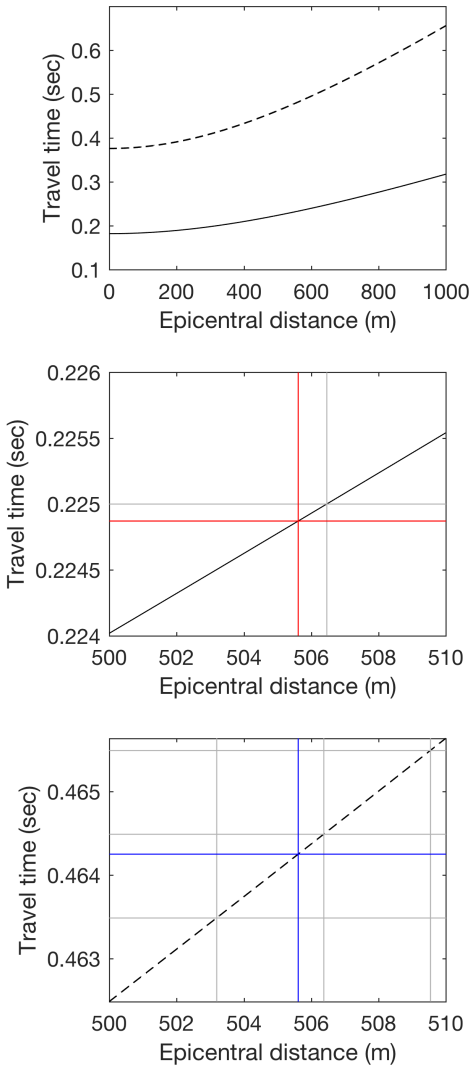

Figure 4.21: Travel time calculations for icequakes traveling through ice with $V_p = 3840$ m/s and $V_s = 1860$ m/s. Top: Travel times for basal icequake P waves (solid line) and S waves (dashed line) through 700 m thick ice as a function of epicentral (map view) distance. Middle (Bottom): P wave (S wave) travel times calculated for epicentral distances of 500-510 m, a typical distance of a basal icequake from a seismometer in this small network. Solid black (dashed black) line shows the travel time. Light grey lines indicate the change in epicentral distance that would cause a 1-sample change in arrival time at a sampling rate of 1000 Hz. Red (blue) lines show the travel time change that would result from the maximum possible change in epicentral distance of 5.6 m for basal icequake family 52, which recurs in unstable slips 9, 17, and 18. For a change in epicentral distance of 5.6 m, the P wave arrival time changes approximately 1 sample, and the S wave travel time changes approximately 2 samples.

quantify the slip over which these amplitude fluctuations take place and compare them to the active slip distance, discussed above.

The widths of these fluctuations in icequake amplitudes proved challenging to determine algorithmically and are consequently picked by hand for the 12 icequake families with clear fluctuations. The edges of the fluctuations are determined where a continuous downward trend in the icequake amplitude time-series deteriorates, either because there are no nearby detections in time, or the amplitude begins to increase again. Only clear, high quality, and continuous fluctuations in amplitude are analyzed. Figure 4.22 shows the icequake amplitude time series of the 12 icequake families with hand-picked fluctuations highlighted in grey. Figure 4.23 shows a histogram of the amplitude fluctuation widths, both in terms of ice displacement and duration in minutes.

The fluctuations in icequake amplitude always take place over less than ~0.1 m of ice slip, with most occurring over slip distances of less than 0.05 m. Figure 4.23 suggests that basal icequake sub-patches may be as small as 0.005-0.01 m wide. The fluctuations correspondingly last for fewer than 4 minutes, with the exception of the family 52 amplitude fluctuation, which lasts 18.5 minutes as the ice is decelerating (Figure 4.22H). The ice slip distances over which the amplitude fluctuations occur are consistent with the smallest active slip distances quantified in Figure 4.19D above, suggesting that the amplitude fluctuations and the active slip distances may result from the same process. For example, the fluctuations can be the result of the ice traversing multiple small basal icequake patches located next to each other, or, alternatively, multiple patches of dirty basal ice traversing a single static basal icequake patch.

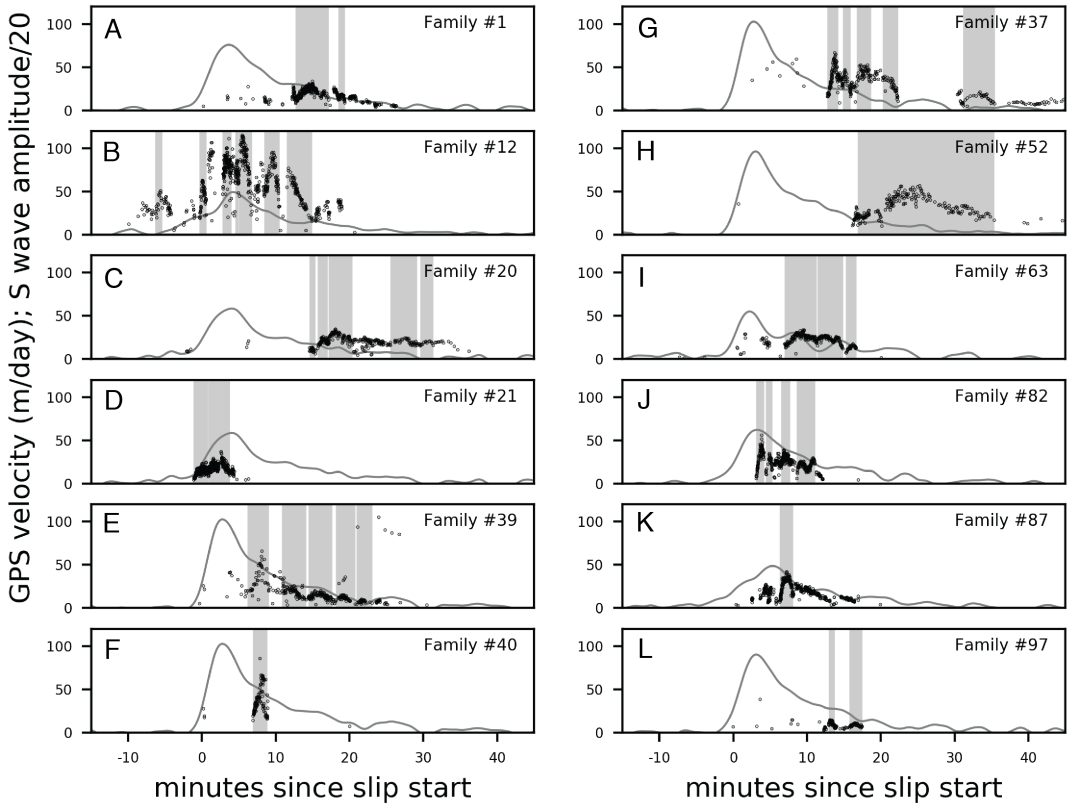

Figure 4.22: Icequake amplitude time series for 12 basal icequake families with clear, high quality amplitude fluctuations. Dark grey lines are the GPS-determined ice sliding velocity. Black dots indicate the icequake amplitude, scaled by 1/20. Grey vertical bars show the hand-picked durations of the amplitude fluctuations.

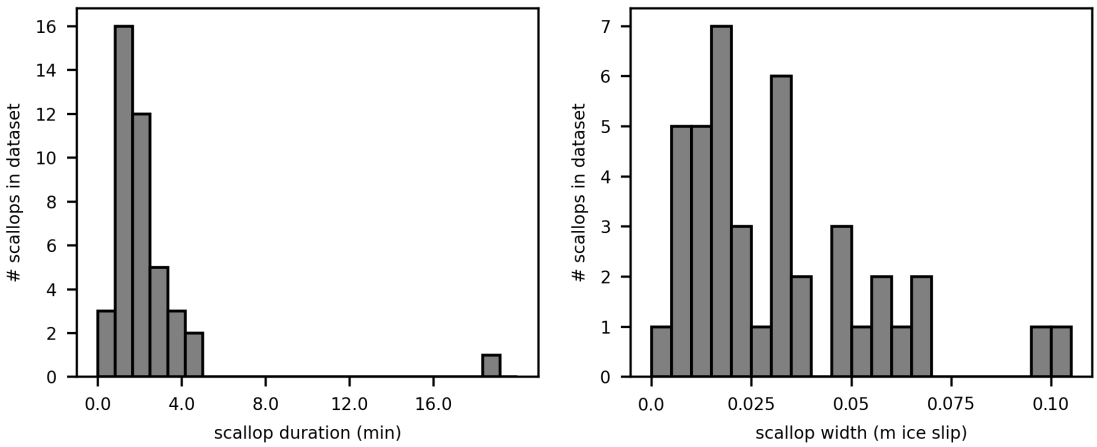

Figure 4.23: Histograms of the number of amplitude fluctuations of given duration in minutes (A) and slip distance (B). All amplitude fluctuations except 1 take place in less than 5 minutes, and all take place over less than 0.11 m of ice slip.

Basal icequake patch dimensions: Smallest seismically observable scale of basal heterogeneity?

Several length scales (or, equivalently, timescales) have emerged in the basal icequake data so far: 1). The seismic source itself has a characteristic dimension determined from the source corner frequencies. 2). Families of repeating icequakes are only active for a limited amount of ice slip (or time). 3). Fluctuations in icequake amplitude also occur over a limited range of ice slip distances (and time durations). Here, I discuss similarities in these length scales and suggest they may be the smallest scale of basal heterogeneity observable using passive seismic observations.

Determination of the corner frequency of the largest icequake sources (Section 4.3.3) suggests a rupture area of ~1-10s of m^2, depending on whether the fault is in ice only, ice-till, or till only. For icequakes of the same seismic moment, rupture on a till-only or ice-till fault would occur over a smaller area than an ice-ice fault,

because the shear wave speed of till is significantly lower than that of ice. An ice-ice fault is unlikely with abundant weak till nearby, suggesting that the icequakes occur on faults with till on at least one side. Rupture areas are therefore likely at the small end of the estimates from Section 4.3.3, ~few m^2, and with fault radii of ~0.5-1 m^2.

These small rupture areas determined from corner frequencies are approximately an order of magnitude larger than the asperity sizes suggested by the active slip distances (~0.02-0.5 m) and the slip over which amplitude fluctuations take place (~0.005-0.1 m). However, the corner frequency rupture areas are also determined from some of the larger icequakes in the dataset, meaning they are an upper threshold for basal icequake patch area. The generally smaller active slip distances and amplitude fluctuation slip distances may reflect that most of the basal icequake patches are just much smaller than the large icequakes for which rupture areas are determined from corner frequencies, with perhaps multiple small basal icequake patches neighboring each other to cause the fluctuations.

Assuming for a moment that the relatively larger rupture areas from corner frequencies represent the largest basal icequake patches, the shorter length scales of cm to tens of cm from active slip distances and amplitude fluctuation slip distances likely reflect the smallest scale of basal heterogeneity that can be observed remotely from the ice surface. Such heterogeneity could result from basal roughness and resulting basal water pressure heterogeneity, from heterogeneous outcropping of different bed materials, from heterogeneously dirty basal ice, or from some combination of all of these conditions. These possible icequake mechanisms are explored further in Section 4.3.5 below.

Alternative interpretations of basal icequake length scales

The observation that the rupture areas determined from corner frequencies are approximately an order of magnitude larger than the active slip distances and the amplitude fluctuation slip distance suggests the smaller distances may reflect a slip evolution distance rather than the actual dimensions of the basal icequake patch. This evolution distance could be, for example, the sliding distance over which over-consolidated till shears and dilates to become normally consolidated (*Barcheck et al.*, 2018). Basal icequake patch evolution could also occur as a result of basal melting during sliding. As the ice slides atop the till, it generates heat frictionally at a rate that scales with the ice sliding velocity. This heat goes into heating basal ice and till and potentially melting basal ice, which would change the basal pore water pressure and affect the sliding stability of basal icequake patches, as discussed in detail below. Finally, active slip distance and the amplitude fluctuation slip distance may also reflect the wavelength of roughness at the ice-bed interface.

4.3.4 How much of the ice stream bed is moving by stick-slip?

Over two weeks of seismic recording, 86 distinct and unique families of basal icequakes are identified. The largest icequakes in this dataset have individual icequake rupture areas that are ~1s - 10s of m^2, depending if they happen in ice only, till only, or between ice and till. The seismic network is sensitive to seismicity in an approximately 13.5 km^2 area of the ice stream bed (area inside tan area, Figure 3.2), meaning that even if all basal icequake families are active at the same time (which they never are), only 86 - 860 m^2 of 13.5 x 10^6 m^2 of the ice stream bed is experiencing seismogenic stick-slip, or 0.0006-0.006% of the ice stream bed.

Nearly all of the ice stream bed, therefore, does not move by basal stick-slip, at least not that produces basal icequakes.

However, stress drop values are orders of magnitude larger than regional driving stresses of a few kPa (*Bindschadler et al.*, 1987; *Beem et al.*, 2014). Even the smallest stress drops estimated for a till-till fault are an order of magnitude larger than the driving stress, suggesting that even though basal icequake patches occupy only a small area of the ice stream bed, they could still play an important role in the mechanism of basal sliding.

4.3.5 Hypotheses for the basal icequake mechanism

Sliding stability of frictional faults

Whether or not a fault will move by stable sliding (no sudden accelerations above the background slip velocity) or unstable sliding (fault slip rates accelerate rapidly to above the background slip velocity) is usually framed in the earthquake literature in terms of rate and state friction (RSF). In the RSF framework, the friction coefficient is described using the following equation, illustrated in Figure 4.24 (e.g., *Scholz*, 1998):

$$\mu = \mu_0 + a \ln \frac{V}{V_0} + b \ln \frac{V_0 \theta}{D_c} \tag{4.7}$$

in which friction coefficient μ depends on a change in sliding velocity V above a background sliding velocity V_0, frictional parameters a and b describing the magnitude of the frictional response to a velocity change (Figure 4.24), the state variable θ describing the evolution of friction with time, and D_c, described as a critical distance of slip over which the change in friction coefficient takes place in response to a velocity perturbation. Resistance to fault sliding τ is then the usual

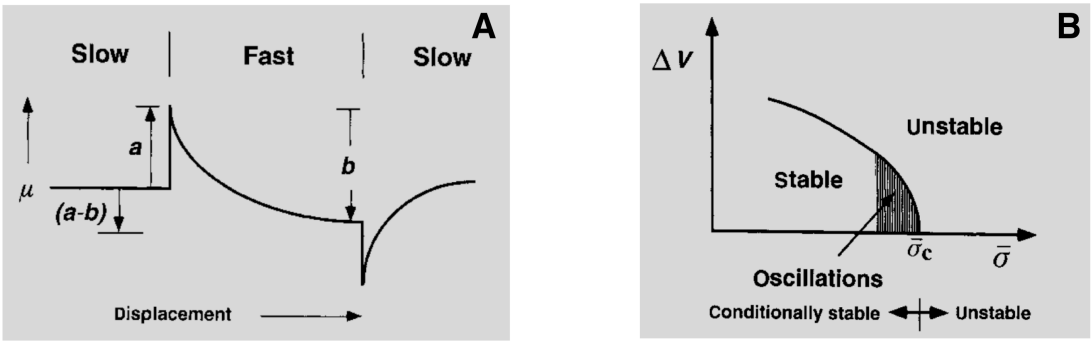

Figure 4.24: Figures from *Scholz* (1998) showing (left) the functional shape of the RSF equation for friction coefficient μ, and (right) how a change in effective normal stress σ_n' can bring a fault closer to or farther from a critical threshold for stability.

expression for friction: $\tau = \mu\sigma_n'$, where the effective fault normal stress σ_n' depends on the absolute value of the fault normal stress σ_n and pore water pressure P as $\sigma_n' = \sigma_n - P$.

Fault stability then depends on the frictional parameters a, b, D_c, and the effective normal stress σ_n'. If $(a - b)$ for a fault is positive, sliding is always stable, and the fault slip velocity will not accelerate above the fault loading rate; this is "velocity-strengthening" behavior. If $(a - b)$ is negative, this is "velocity-weakening" behavior, and there is a critical effective normal stress $\sigma_{n_{crit}}'$ that defines the transition in behavior from stable or conditionally stable to unstable, illustrated in Figure 4.24B:

$$\sigma_{n_{crit}}' = \frac{kD_c}{-(a-b)} \tag{4.8}$$

This means that, for a given set of frictional parameters a, b, and D_c, changing the effective normal stress σ_n' impacts the sliding stability of the fault. Comparably, if frictional properties of a material evolve through time, the value of $\sigma_{n_{crit}}'$ may change, causing a fault to transition between stable, conditionally stable, and unstable.

Sliding stability of icequake faults and implications for the basal icequake mechanism

The basal icequakes in this dataset turn on and off over relatively short amounts of time, typically minutes, and short distances of slip, typically just a few cm or tens of cm. These short icequake family lifespans suggest that the rupture patches transition from stable sliding to unstable sliding and back to stable sliding relatively rapidly. I offer four simple explanations for this behavior in the framework of RSF:

1. The frictional parameters of the basal icequake patch material, a, b, and D_c, may be changing with slip in situ. This could mean the interface is evolving with slip, perhaps as a result of over-consolidated basal till dilating and becoming normally consolidated till (*Barcheck et al.*, 2018). Future comparison of basal icequake family source parameters and behavior with RSF models of frictional sliding may be able to constrain this behavior.

2. Changing basal icequake patch frictional parameters could also result from advection of upstream materials with different frictional properties onto the icequake fault. Debris-laden ice is more likely to have velocity-weakening behavior than clean ice (*Zoet et al.*, 2013b), and movement of dirty basal ice into an area with velocity-weakening bed material could produce basal seismicity. Alternatively, ice movement may drag soft, aseismic, velocity-strengthening till to cover outcrops of velocity-weakening material, thereby quieting basal seismicity.

3. The effective normal stress on the icequake faults may be changing due to cavitation, especially at the high slip rates observed at the start of unstable slip. Cavitation results from roughness of the ice bed interface. As the ice slides, small cavities open in the lee sides of roughness elements and become areas of low pore pressure. Depending on the bed morphology and diffusivity of the subglacial

hydrologic network, cavitation can cause temporary local decreases in the basal water pressure, causing a temporary increase in effective normal stress at the edges of the cavity which may exceed $\sigma'_{n_{crit}}$ and cause these areas of the ice base to transition to unstable sliding. The local drop in basal water pressure can also cause a change in frictional properties of till surrounding the cavity as water slowly diffuses out of the surrounding till over subsequent minutes. A characteristic lengthscale L of till porewater diffusion over a timescale t of several minutes and at hydraulic diffusivities of 10^{-8} m^2/s expected for this till (*Tulaczyk et al.*, 2001) would be $L \sim \sqrt{\kappa t}$, or $L \sim$ 1-2 mm. A slight stiffening of a thin, mm-thick layer of till over several minutes is an improbable mechanism for generating basal seismicity: The basal seismicity increase usually happens as soon as the ice sliding begins, before there is time for pore water diffusion to dewater and stiffen the till.

Additionally, if cavitation were driving the mechanism behind basal icequakes, more basal icequakes should occur at the start of unstable slip, when sliding velocities are highest and cavitation and resulting increases in effective normal stress are largest. This prediction is not clearly borne out by my observations; basal icequakes occur throughout unstable slip events.

4. The effective normal stress on the icequake faults may change throughout an icequake family's lifetime as a result of meltwater generation from shear sliding. Icequake families may simply turn off when enough meltwater is generated to increase pore water pressure, decrease effective normal stress below $\sigma'_{n_{crit}}$, and cause the fault to transition to conditionally stable or stable sliding.

4.3.6 Four basal icequake mechanisms

I propose four mechanisms (illustrated in Figure 4.25) for the families of repeating basal icequakes observed beneath the Whillans Ice Plain:

1. Cavitation: During sliding, cavitation in the lee sides of bed roughness (Figure 4.25A and B) will cause local decreases in pore pressure and increases in effective normal stress, which may temporarily transition areas of the ice stream bed from stable sliding to unstable sliding as the basal hydrologic network adjusts. With this mechanism, rupture areas will vary over the lifetime of a basal icequake family as cavities grow and are destroyed, and as the basal hydrologic network adjusts to changing basal water pressure.

2. Heterogeneous basal ice debris concentration: Basal icequakes may occur where basal ice contains large volumes of frozen debris, causing basal ice sliding to transition to velocity-weakening behavior (*Zoet et al.*, 2013b). In this situation, the rupture area corresponds to the area of debris laden ice in contact with the bed (Figure 4.25C). Basal icequake families may turn off when enough meltwater is generated by frictional heating from sliding of debris-laden ice to lower effective normal stress and transition the icequake patch to stable sliding, or when basal debris becomes dislodged from the ice base and incorporated into the till layer.

3. Bed material heterogeneity: Basal icequakes may occur where stiff, velocity-weakening basal material outcrops through frictionally stable till and creates a velocity-weakening patch of ice-stream bed (Figure 4.25D). This brittle basal material could be over-consolidated till from deeper in the till package (*Barcheck et al.*, 2018), stiff sediments, or bedrock outcropping through the till. For this mechanism, the rupture area is the size of the outcrop of velocity-weakening material, and basal icequake family lifetime corresponds to the amount of slip required to cause the over-consolidated till to dilate to normally consolidated, the amount of slip required to advect upstream velocity-strengthening till on top of the velocity-weakening material, or when enough meltwater is generated by frictional heating to lower effective normal stress and transition the patch to stable

sliding.

4. Combined heterogeneity of basal debris concentrations and bed material: Basal icequakes may only happen where both velocity-weakening bed material outcrops to the ice base and the basal ice contains sufficient debris concentration to also have velocity-weakening behavior (Figure 4.25E). In this case, the rupture area corresponds to the area of bed in which both velocity-weakening bed material and dirty basal ice are in contact. And the lifetime of basal icequake families may correspond to the amount of slip over which both dirty basal ice and stiff bed material are in contact.

4.3.7 Preferred basal icequake mechanism: Basal debris with bed material heterogeneity

As discussed above, the cavitation mechanism predicts greater basal seismicity at the start of sliding, as many cavities open all at once. This behavior is not observed in the data. My preferred mechanism of basal seismicity, therefore, is basal material heterogeneity in both basal ice and till. I hypothesize that clean, debris-free basal ice layers near the pressure melting temperature are both velocity-strengthening (*Zoet et al.*, 2013b) and too low-friction to cause stick-slip at the ice base, even in the presence of brittle material such as stiff till or bedrock. Likewise, normally consolidated, porous till in the presence of abundant basal water is usually weakly velocity-strengthening (*Iverson et al.*, 1998; *Tulaczyk et al.*, 2000), and is unlikely to cause stick-slip at the ice base. Therefore, I suggest that basal icequakes happen where dirty basal ice units with sufficient debris concentration slide atop an outcrop of velocity-weakening ice stream substrate (Figure 4.25E). Beneath the WIP, this velocity-weakening material is unlikely to be bedrock (*Luthra et al.*, 2016), suggesting a central role for over-consolidated

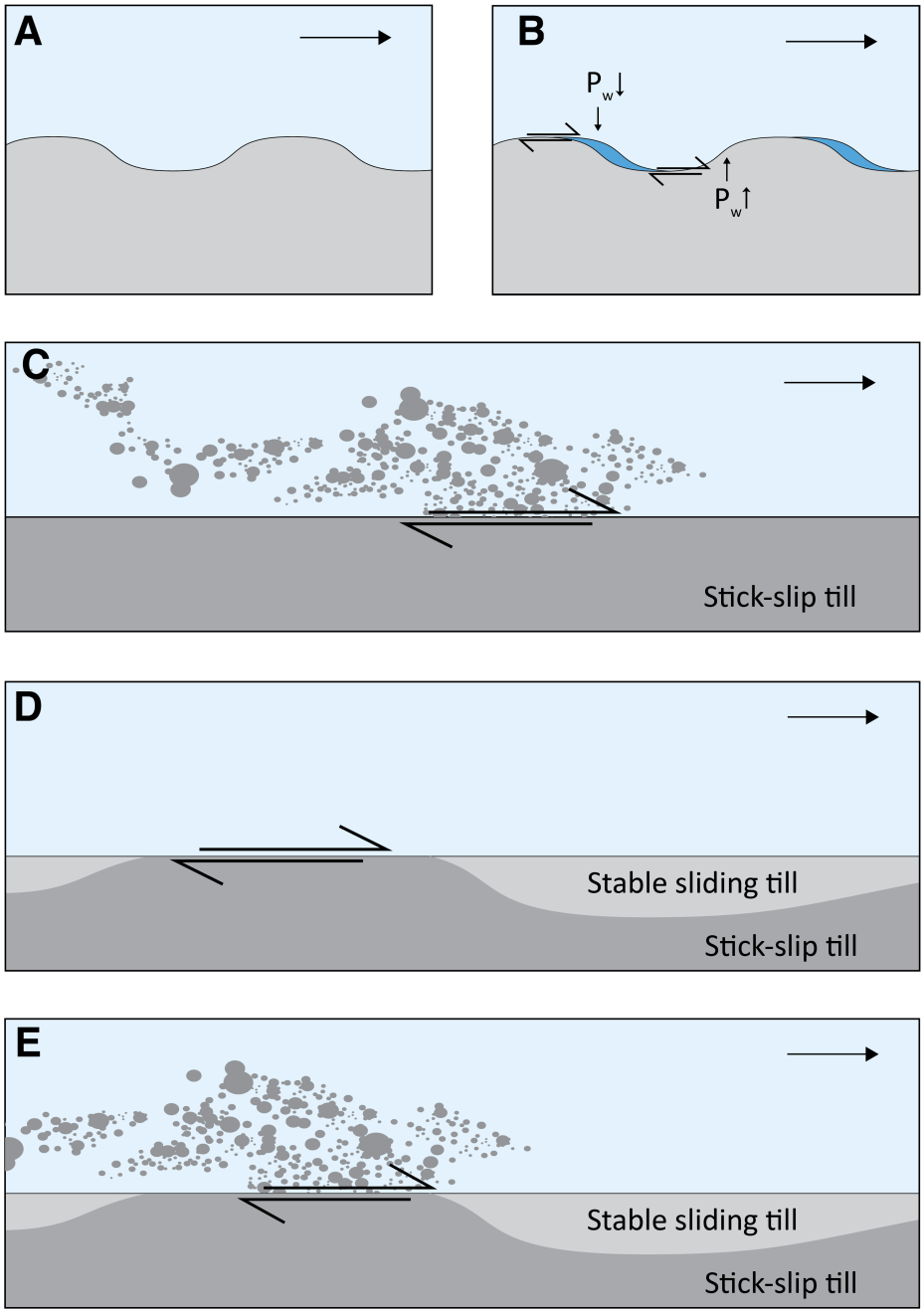

Figure 4.25: Schematic diagram of four basal icequake mechanisms: A,B: Cavitation-induced increase in effective normal stress; C: Debris-laden basal ice sliding; D: Ice sliding over patches of velocity-weakening substrate, possibly over-consolidated till; E: Combined debris-laden basal ice sliding over velocity-weakening substrate.

till or stiff sediments in the basal icequake mechanism. This is consistent with the interpretation of *Smith et al.* (2015) from Rutford Ice Stream (RIS) that RIS basal icequakes occur where stiff basal till outcrops to the ice base.

This preferred mechanism suggests that the streaks of icequakes result from laterally varying bed material properties (for example, normally- vs over-consolidate till) plus the spatial effect of heterogeneously debris-laden basal ice units.

4.3.8 Is there basal icequake evidence for healing of the ice-bed interface between unstable slip events?

Previous work has shown that the Ice-Plain-wide basal yield strength increases with time following the end of an unstable slip event (*Winberry et al.*, 2009a), a phenomenon known as healing. This a well-known frictional phenomenon, in which longer contact time between two surfaces causes an increase in the frictional yield strength. Several hypotheses have been suggested to explain healing of the basal interface of the WIP between consecutive unstable slip events: Basal freezing may cause till dewatering and strengthening during stagnant phases between unstable slips (*Winberry et al.*, 2009a; *Walter et al.*, 2011). Strengthening may occur by dissipation of pore water pressure that was increased in the stoss side sediments of ploughing particles during unstable slip (*Iverson*, 2010). Or, pressure melting and re-freezing of basal ice at points of impingement on basal roughness elements may increase real area of contact with time (*Zoet and Iverson*, 2018). Additionally, WIP basal tremor, which is interpreted to be closely spaced basal icequakes, is observed to have higher amplitudes with longer time since previous unstable slip, which is interpreted as either an increase in bed shear modulus with time since previous unstable slip, or a decrease in aseismic slip between repeating basal icequakes (*Lipovsky and Dunham*, 2016).

Any evidence of changing basal icequake activity either as a function of increased healing time between consecutive unstable slip events, or during different phases of an individual unstable slip event, may help to understand the mechanism of basal healing between unstable slips.

First, I explore trends in basal icequake timing as a function of elapsed time since previous unstable slip event. As mentioned above, unstable slip events occurring less that ~16 hours after the previous unstable slip tend to feature precursory seismicity, while events occurring more than 16 hours after the previous unstable slip do not. Additionally, Figures 4.17, 4.18, and 4.19A,B show that more basal icequake families are active before the peak ice velocity (orange bars and dots in Figures 4.17, 4.18, and 4.19A,B) when less time has elapsed since the previous unstable slip event. Together, these observations suggest that basal icequake activity begins at lower values of total slip with less time elapsed since the previous unstable slip. It seems to take less ice slip for basal icequake patches to begin failing seismically with less healing time. This would suggest that the icequake patches with less healing time have a lower initial yield strength that is reached with less stressing from slip of the surrounding basal ice. Basal icequake patches may therefore strengthen with healing time between unstable slip events.

However, unlike basal tremor amplitudes (*Lipovsky and Dunham*, 2016), basal icequake amplitude is not clearly correlated with elapsed time since previous unstable slip. Figure 4.26 shows the median amplitude (black dots) and the standard deviation of the amplitude distribution of the largest S wave arrivals for each icequake family. S wave amplitudes are determined as the absolute value of the S wave arrival (in counts) on the seismometer channel with the largest median S wave amplitude. While the longest elapsed time since previous unstable slip does indeed have the largest median amplitude S waves, there is no strong trend

over all slip events in unstable slip recurrence time and icequake amplitude. This suggests that either the basal icequake mechanism is more complicated than the basal tremor mechanism and depends on more than just healing time, or perhaps basal icequakes and basal tremor are different mechanisms entirely.

The best evidence in this dataset for healing of the ice-bed interface between unstable slip events is the occurrence of more seismicity earlier in slip events with shorter healing times. Overall, there is little evidence of the mechanism of healing between unstable slips.

4.3.9 Basal icequake amplitude fluctuations as velocity fluctuations

An alternative explanation for the fluctuations in icequake amplitude is suggested by the observation that amplitude is correlated overall with GPS ice sliding velocity for many of the icequake families (e.g., Figure 4.12C). If icequake amplitude is overall correlated with sliding velocity, perhaps the fluctuating amplitudes indicate acceleration and deceleration of local areas of the ice base above and below the surface velocity. Such local basal ice sliding accelerations and decelerations would not necessarily be observable from ice surface velocity measurements, similar to the way that the bristles of a toothbrush dragged across cement might get stuck on individual grains in the cement, but the handle of the toothbrush moves with a smooth velocity.

In this section, I explore this possibility and quantify the magnitude of acceleration and deceleration indicated by the change in icequake amplitude within four icequake families. I choose four icequake families with a good correlation between icequake amplitude and ice sliding velocity from the GPS. For each of these four families, shown in Figure 4.27, I assume the icequake amplitudes to

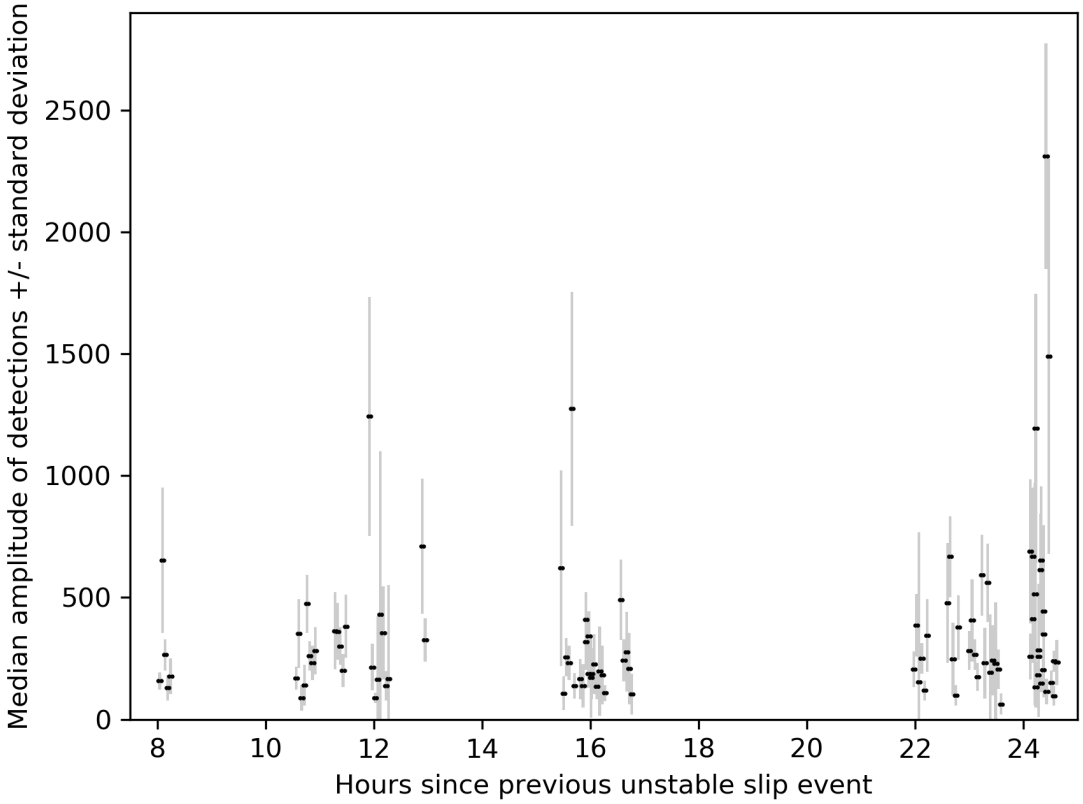

Figure 4.26: Amplitude of detections for all basal icequake families. Black dots are median amplitudes of the largest S wave arrival on one consistent channel. Grey bars are one standard deviation of the distribution of the S wave amplitudes for each family. Icequake families are sorted by the unstable slip event in which they occur, and unstable slip events are sorted by elapsed time since the previous unstable slip event, or healing time. Though the single highest amplitude basal icequake family occurs after long healing time, there is no consistent trend in icequake family median amplitude with healing time.

be a linear function of the ice sliding velocity, and I solve for a scaling coefficient between the ice velocity and the icequake amplitudes using linear least squares inversion. This scaling coefficient relates the amplitude of the icequakes to the GPS velocity. I then divide the icequake amplitudes by this scaling coefficient, effectively converting them to units of ice sliding velocity (m/day), and subtract the GPS velocity that corresponds to each basal icequake (4.27B,D,F,H). This leaves residual fluctuations in amplitude that would represent increases in basal sliding velocity above and below the GPS sliding velocity.

The amplitudes of these residual sliding velocities are all in the range of +/- 50 m/day, in the same range as the GPS-determined ice sliding velocity, which is around 100 m/day at the fastest. A residual sliding velocity of -25 m/day would mean the basal ice is sliding 25 m/day slower than the velocity observed by the GPS at the surface. The fastest possible basal ice sliding velocity would be the fastest GPS-observed sliding velocity (~100 m/day) plus the fastest residual sliding velocity from an amplitude fluctuation (~+50 m/day), giving a maximum basal sliding velocity of ~150 m/day. A basal sliding velocity of 150 m/day corresponds to about 2mm/sec, well within a reasonable range.

This hypothesis would be strongly supported if the basal icequake inter-event times also decrease during amplitude peaks, indicating that basal icequakes occur closer together in time during faster sliding phases shown by amplitude peaks. This would be consistent with the general observation from Section 4.3.2 that basal icequakes occur closer together in time for faster ice sliding velocity (Figures 4.12, 4.13, 4.14). Current results do not, unfortunately, show clear evidence that basal icequake inter-event time changes inversely proportional to icequake amplitude, which would be predicted if amplitude fluctuations correspond to accelerations and decelerations. Further refinement of icequake origin times may

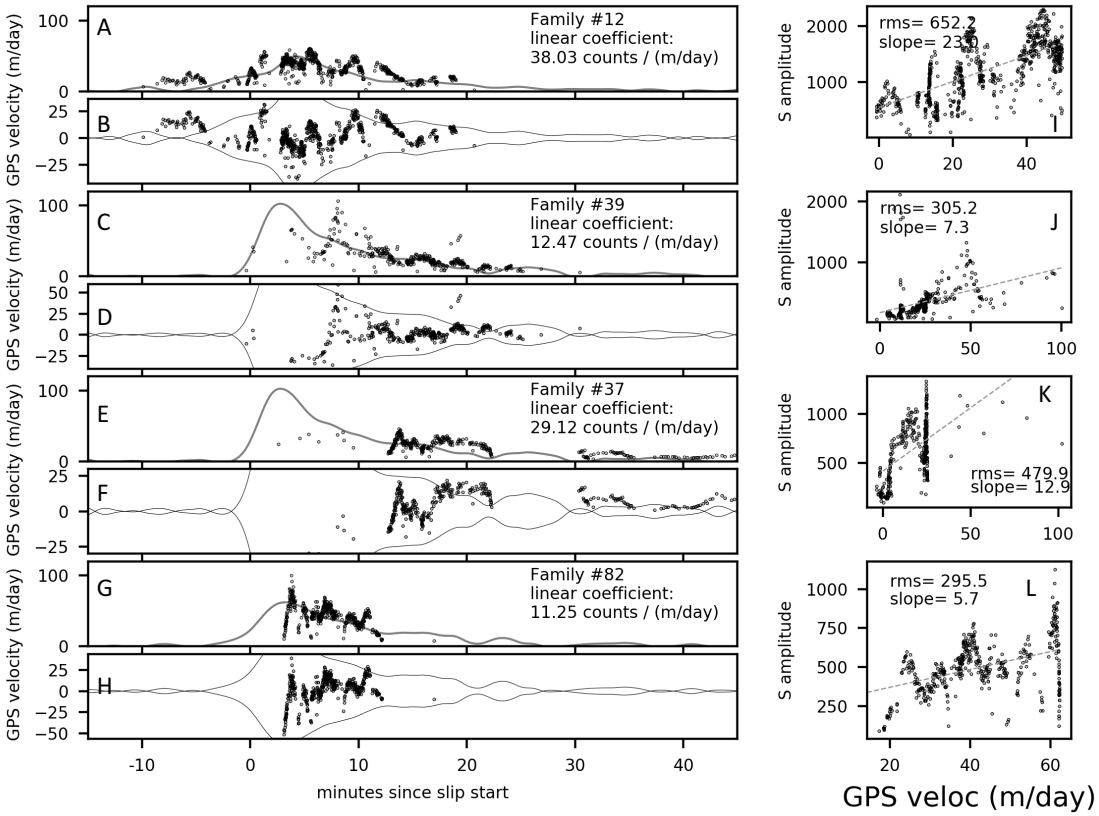

Figure 4.27: Basal icequake amplitude fluctuations of four basal icequake families. Amplitude fluctuations are fit as a linear function of ice velocity, giving a linear coefficient for each family that converts amplitude to units of ice sliding velocity. A,C,E,G: GPS velocity (black line) with time series of icequake amplitudes scaled by the given linear coefficient for each family to convert to units of m/day. B, D, F, H: Scaled icequake amplitudes minus icequake velocity to give residual velocity fluctuations suggested by the icequake amplitudes. Black lines are +/- raw GPS ice sliding velocity to show that residual velocity amplitudes scale with overall sliding velocity. Residual ice velocity fluctuations are in the range of +/- 50 m/day, well within a reasonable range. Right: S wave amplitude as a function of GPS velocity showing overall positive relationship between amplitude and ice sliding velocity, with amplitude fluctuations superposed.

help. Nevertheless, this idea that basal icequake amplitude fluctuations may indicate basal sliding velocities fluctuating around the GPS-determined velocity is intriguing and warrants further study.

4.3.10 Repeating basal icequakes and repeating tectonic earthquakes

A final interesting question is the extent to which these small earthquakes on isolated faults on the ice-bed interface are similar to repeating earthquake sequences on tectonic faults. Repeating earthquake sequences are series of events with periodic or quasi-periodic recurrence times and nearly identical waveforms, usually considered to be re-rupturing parts of the same isolated earthquake-prone fault patch, or asperity (e.g., *Marone et al.*, 1995; *Nadeau and Johnson*, 1998; *Okada et al.*, 2003; *Chen et al.*, 2010).

One relationship often explored in repeating earthquake sequences is the relationship between the earthquake recurrence time, or time since the previous earthquake in the sequence, and seismic moment. Two varieties of this relationship have emerged. On the one hand, longer recurrence times between repeating earthquakes often cause events with larger seismic moment (e.g., *Vidale et al.*, 1994; *Nadeau and Johnson*, 1998; *Peng et al.*, 2005). This results from longer healing times and resulting higher frictional strength on a repeating earthquake asperity by the time it ruptures, potentially generating a slightly larger moment. This relationship is seen, for example, in repeating earthquake sequences on various faults in central California (*Vidale et al.*, 1994; *Marone et al.*, 1995; *Nadeau and Johnson*, 1998; *Peng et al.*, 2005), and often in experiments (e.g., *Mclaskey et al.*, 2012). Conversely, other observations show larger seismic moment at shorter recurrence times (e.g., *Marone et al.*, 1995; *Peng et al.*, 2005; *Chen et al.*, 2010).

For example, a small subset of the repeating earthquakes occurring on the Parkfield section of the San Andreas Fault have larger seismic moment and shorter recurrence time just after the 2004 M6 Parkfield earthquake, which then slowly revert to longer recurrence time and smaller seismic moment with time after the mainshock (*Chen et al.*, 2010). This peculiar relationship is interpreted as resulting from rupture on velocity-weakening fault patches with a nucleation length comparable to the patch size (*Chen and Lapusta*, 2009; *Chen et al.*, 2010): When the nucleation length is nearly the same as the patch area, much of the slip at the patch edges occurs aseismically during the nucleation phase and seismic events happen in the middle of the patch where the stress concentrations are highest. At higher loading rates, stress concentration in the middle of the patch are higher, and the patch can consequently rupture with a larger area and larger seismic moment. *Chen et al.* (2010) find that repeating earthquake sequences with overall smaller moment exhibit larger relative moment at shorter recurrence times just following the 2004 M6 Parkfield earthquake.

I assess whether either of these relationships holds for basal icequake Families 12 and 82, which have 709 and 486 detections, respectively. I calculate seismic moment for each icequake detection using data from the same station with the highest quality vertical component P wave; I fit each P wave displacement spectra individually, as described in Section 4.3.3 using the *Brune* (1970) model with $n = 2$. Because I only fit the P wave from a single station, the values of the seismic moments may not be correct in an absolute sense because of radiation pattern effects, but the relative variations through time are correct. I also calculate recurrence time for each detection as the elapsed time since the previous detection. Results are summarized in Figures 4.28 and 4.29, in which I also plot raw seismic amplitudes for comparison. Interestingly, calculated seismic moments show less

variability than raw amplitude values for both families, though moment is still overall correlated with GPS-determined ice sliding velocity. Also, seismic moment shows a much larger range of values at higher GPS ice sliding velocity than at lower sliding velocity.

Importantly, Figures 4.28D and 4.29I show the relationship between seismic moment and recurrence time. Both families show generally larger seismic moment values at the shortest recurrence times, especially Family 12 (Figure 4.28D). This suggests that larger seismic moment is not related to greater healing of the basal icequake patch with longer recurrence times; instead, seismic moment is largest at the shortest recurrence times. That healing is not important intuitively makes sense, since the recurrence intervals are remarkably short, in some cases only a fraction of a second.

My results may be compatible with the model of (*Chen et al.*, 2010), suggesting that aseismic slip at patch edges during longer recurrence times can decrease the seismic rupture area and moment. Additionally, I suggest the larger seismic moments at short recurrence times may be the result of a strain-rate-hardening process, for example cavitation and interaction with the subglacial hydrologic network. Because the shorter recurrence times and larger seismic moment events also occur at higher GPS ice sliding velocities, the larger events are occurring when basal cavitation rates should be highest. As discussed above, cavitation in the presence of relatively stiff basal material can create areas of low basal water pressure near cavities, causing increased effective normal stress. This will increase Coulomb frictional yield strength of basal icequake patches and result in icequakes with larger seismic moment at high sliding velocities. Fluctuations in seismic moment may then result from interactions with the basal hydrologic network, either by diffusion of pore pressure or pulses of fluid movement.

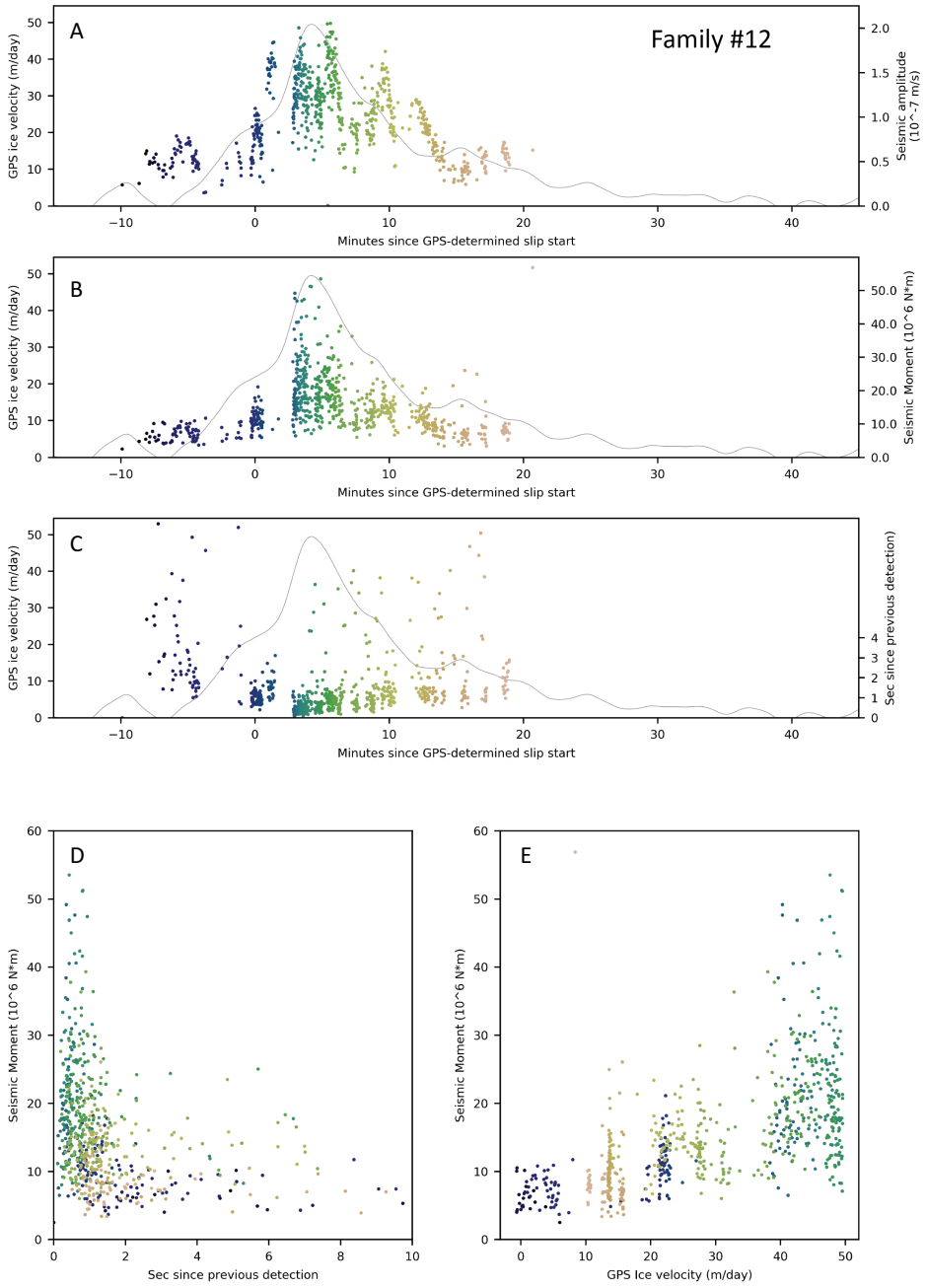

Figure 4.28: Seismic amplitudes (A), seismic moments (B), and recurrence times (C) for basal icequake family 12. Grey lines are the GPS-determined ice sliding velocity. Panel D crossplots icequake recurrence time and seismic moment, showing larger seismic moments at shorter recurrence intervals. Panel E crossplots GPS ice sliding velocity and seismic moment, showing larger seismic moment and range of seismic moment at larger sliding velocities.

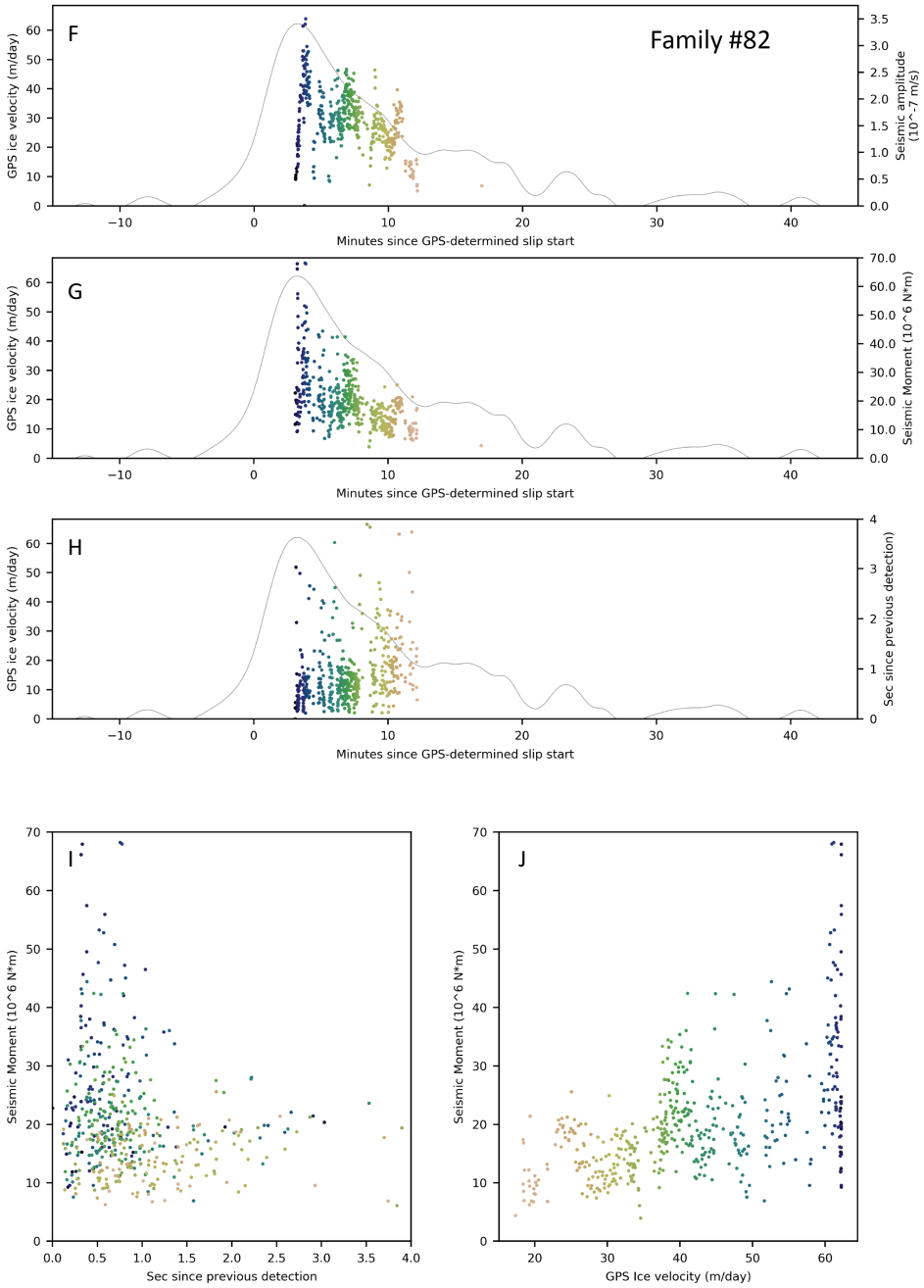

Figure 4.29: Seismic amplitudes (F), seismic moments (G), and recurrence times(H) for basal icequake family 82. Grey lines are the GPS-determined ice sliding velocity. Panel I crossplots icequake recurrence time and seismic moment, showing larger seismic moments at shorter recurrence intervals. Panel J crossplots GPS ice sliding velocity and seismic moment, showing larger seismic moment and range of seismic moment at larger sliding velocities.

Repeating tectonic earthquake sequences are also often used to infer creep rates on deep faults (e.g., *Schaff et al.*, 1998; *Igarashi et al.*, 2003; *Uchida et al.*, 2003; *Matsuzawa et al.*, 2004; *Nadeau and McEvilly*, 2004; *Taira et al.*, 2014; *Turner et al.*, 2015). Another interesting question to ask of the basal icequake sequences is whether or not the ice sliding velocity is clearly related to the recurrence time of the icequakes within a family. I find that the relationship between recurrence time and loading rate for the basal icequake families is variable: Figures 4.12, 4.13, and 4.14 show that some of the families of repeating icequake sequences do exhibit an inverse relationship between GPS ice sliding velocity and recurrence time, while others are more equivocal. Family 12 in Figure 4.12F, for example, shows a clear decreasing relationship between icequake recurrence time and ice sliding velocity. Families 20 and 82 in Figure 4.13R, 4.14LL show similar though noisier relationships, while Family 39 in Figure 4.14FF shows no relationship whatsoever. Other families seem to have a relationship with GPS sliding velocity that changes through the lifetime of the family. For example, Family 1 in Figure 4.12L starts with long recurrence times at high slip velocity (dark blue dots), then evolves into a more typical relationship of small recurrence time at large GPS velocity, and vice versa. These results suggest that variability is dominant. Perhaps repeating earthquake sequences on tectonic faults are comparably variable, with some repeating earthquake sequences having a clear relationship with creep rates, some with changing relationships through time, and some with no clear relationship at all.

In summary, basal icequake sequences appear to exhibit some behaviors similar to some sequences of repeating tectonic earthquakes. Basal icequake families 12 and 82 show a larger range in seismic moment at larger GPS sliding velocity and smaller recurrence intervals. This suggests that healing is not playing a role

in determining icequake magnitude, but instead icequake magnitude may be controlled by the nucleation size being comparable to the icequake patch size (*Chen et al.*, 2010), or a strain-rate-hardening process, for example basal cavitation rate. Additionally, some basal icequake families exhibit a clear relationship of decreased icequake recurrence time as a function of increased GPS-determined ice sliding velocity, while other families exhibit a relationship that changes through time, or no relationship at all. Thus, the repeating basal icequake families neither clearly support nor weaken the argument that repeating sequences of tectonic earthquakes can be used to directly infer fault creep rates.

Appendix A

Supplementary information for "Implications of basal micro-earthquakes and tremor for ice stream mechanics: stick-slip basal sliding and till erosion," *Earth and Planetary Science*

Letters

A.1 Methods: additional details

A.1.1 Seismic data collection and event detection

Broadband seismic data were collected at 55 locations on the WIP during three separate field campaigns in Dec-Jan 2010-11 and Dec 2011 (see Table A.1 for details). All seismic data are high pass filtered above 1 Hz to eliminate teleseismic and regional earthquake signals. We rely on visual detection of basal micro-earthquakes because standard STA/LTA detectors and cross correlation methods are problematic for this dataset. The basal micro-earthquakes identified by *Winberry et al.* (2013) have short duration (< 1 sec), and at times they have a low signal to noise ratio. STA/LTA detectors fail to detect basal micro-earthquakes without also detecting significant spurious seismicity. Additionally, a single basal micro-earthquake typically only shows up at one seismometer, meaning network association cannot be used to sort through spurious detections. Cross correlation detection is also problematic because detection depends on choice of event template, and event wave shapes change between subsequent slip events and between sites. Consequently, we rely on visual detection of basal micro-earthquakes. We inspect the data in the time and spectral domains for evidence of local basal micro-earthquakes and tremor during each slip event.

In the time domain, basal micro-earthquakes are identified as short-lived seismic events above the background noise with a distinct characteristic waveform shape (Figure 2.1B, 2.1C): P energy primarily on the vertical component, S energy primarily on the horizontal components, with no discernible surface waves.

Typical S minus P intervals of ~0.18-0.4 seconds indicate a hypocentral distance of ~650-1440m (V_p=3840 m/s; V_s=1860 m/s (*Luthra et al.*, 2016)), consistent with origins at the base of the ice with regional thicknesses of 650-800 m (*Fretwell et al.*, 2013). Often these events repeat, occurring in groups with nearly identical waveforms. Where P energy is low, repeating basal events are detected solely on the basis of the characteristic S wave shape and lack of surface waves (Figure 2.1B, N and E components), and repeating nature.

This method selectively finds local (<few kms source distance) basal micro-earthquakes. Nearby near-surface crevassing events are dismissed because they would contain surface waves (*Walter et al.*, 2009) and have smaller S minus P time interval for crevassing taking place less than an ice thickness away. Basal events from further than a few ice thicknesses away (several km) may also contain significant surface wave energy and are indistinguishable from large distal near-surface crevassing events, or they attenuate before reaching the sensor. Tectonic earthquakes would occur several km deeper and therefore have much longer S minus P time intervals. Other seismic events lacking distinguishable P and S wave arrivals are not detected, for example possible subglacial lake drainage events (*Winberry et al.*, 2009b). High wind speeds can generate noise that swamps basal micro-earthquake signal. Slip events with high background noise are removed from the dataset when broadband noise amplitudes become greater than typical basal micro-earthquake or tremor amplitudes.

If there are more than ~10 characteristic basal micro-earthquakes during an unstable slip event, that unstable slip event is marked as having basal micro-seismicity. Individual slip events and different stations have extremely variable numbers of basal micro-earthquakes; some have only 10s-100s of basal micro-earthquakes, while others have 1000s per unstable slip event. Because it is tedious

to select 1000s of basal micro-earthquakes visually, results are presented as percent of unstable sliding events that exhibit basal micro-seismicity at each station, rather than total number of basal micro-earthquakes recorded at that station.

Basal tremor is identified as gliding lines in spectrograms of seismic data during unstable slip events (Figure A.1; (*Lipovsky and Dunham*, 2016)). Spectrograms are generated for the East component of each station for each unstable slip event and visually inspected for the presence of gliding lines. Any hint of continuously gliding lines during slip is marked as tremor, though the amplitude of tremor also varies greatly between stations and unstable slip events.

A.1.2 GPS data collection and processing

At each of 39 GPS sites, total motion is partitioned into unstable motion during a slip event and stable sliding between unstable slip events, typically of much smaller magnitude. The relative fraction of each varies across the Ice Plain and could be related to spatially varying bed strength, bed frictional properties, or ice loading geometry. This variation in space is captured by the geodetic coupling coefficient, which is the fraction of total ice motion accommodated through unstable slip events (*Walter et al.*, 2015). Where geodetic coupling is high, most of the ice motion occurs during the ~30 minute slip events, and ice barely moves between these unstable slip episodes.

GPS data from three deployments were processed for 3-8 weeks in Dec-Jan 2010-11 and Dec 2011 (Supplementary Table A.1) using either the Precise Point Positioning (PPP) Method (*Zumberge et al.*, 1997; *Winberry et al.*, 2014) or the *track* package within GAMIT/ GLOBK (*Herring et al.*, 2015), with the nearby permanent rock site Ramsey Glacier (RAMG) as a base station for *track* processing. Sampling interval for all GPS is 15 seconds.

GPS solutions are projected to polar stereographic coordinates with true latitude at 71° S and then rotated into a downstream / transverse to flow coordinate system. To determine geodetic coupling for each site, we fit the downstream displacement time series for each unstable sliding event to a hyperbolic tangent curve using a nonlinear least squares regression. Adapting the method used by *Larson et al.* (2004) for subduction zone slow slip events (Supplementary Figure A.2), we use the equation:

$$x(t) = x_0 + Vt + \frac{U}{2}\left[tanh\left(\frac{t - T_0}{\tau}\right) - 1\right] \tag{A.1}$$

where *x(t)* is downstream displacement at time t, x_0 is initial displacement, V is ice creep velocity before and after unstable slip, U is total displacement occurring during unstable slip, T_0 is the time halfway through the unstable slip, and τ scales with the time over which slip occurred. We discard unstable slip events with large unrealistic GPS position excursions (e.g., the ice stream moves uphill) or rms residuals greater than 0.035 m. We define geodetic coupling as the percent of total motion at a GPS site on the Ice Plain that occurs during unstable slip events. We calculate geodetic **X** coupling by summing over all unstable slip events with adequate data:

$$\mathbf{X} = \frac{\sum_{n=1}^{i} U_i}{\sum_{n=1}^{i}(U_i + u_i)} \times 100 \tag{A.2}$$

where U_i is the displacement during the ith unstable slip, and u_i is the pre-slip displacement determined from the fit from 60 minutes after the start of the previous unstable slip to 15 minutes before the current unstable slip. We interpolate the results to a 100m spacing grid using natural neighbor interpolation (Figure 2.2).

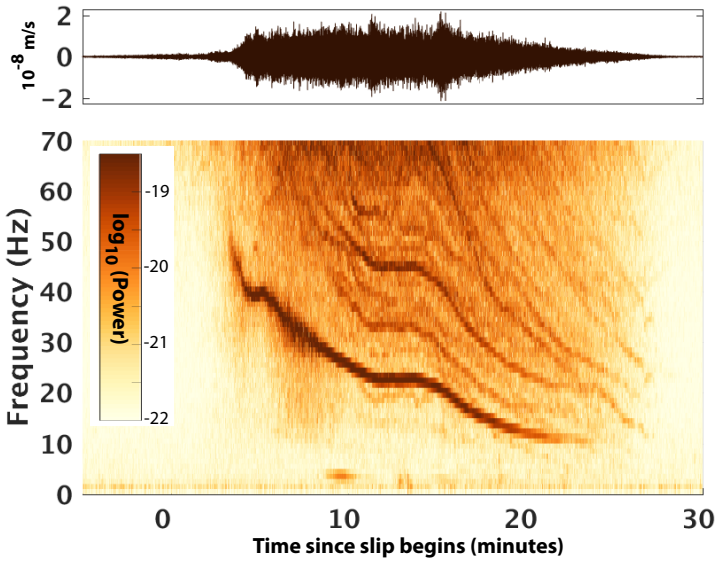

Figure A.1: Spectrogram of seismic data collected during unstable slip (site BB09, (*Pratt et al.*, 2014; *Winberry et al.*, 2014; *Lipovsky and Dunham*, 2016) on Dec 18, 2010. Gliding lines are apparent, and the dominant frequency decreases as unstable sliding progresses and the ice slows. Basal tremor is interpreted as small amplitude basal micro-earthquakes rapidly repeating in time, such that the number of events per second is the frequency of the fundamental spectral gliding line.

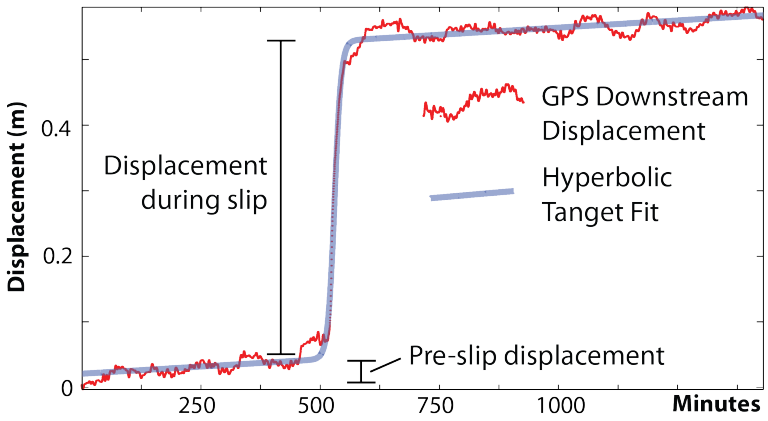

Figure A.2: Hyperbolic tangent fit to GPS data, following *Larson et al.* (2004), to derive geodetic coupling.

TABLE S1. DETAILS OF SEISMIC AND GPS DEPLOYMENTS

Field campaign	Type of Seismometers (# seismometers) *Sample rate (Hz)*	Recording time # unstable slip events	# GPS (sampling interval [s]) *Processing package*
Dec-2010	Guralp CMG 3T (5) *200*	4 weeks 32 slips	7 (15 sec) *track*
Dec 2010-Jan 2011	Nanometrics Trillium 120 (17) *200*	7 weeks 79 slips	20 (15 sec) *PPP*
	Guralp CMG 3T (18) *200*		
Dec-2011	Nanometrics Trillium 120 (15) *500*	3 weeks 26 slips	12 (15 sec) *PPP*

Table A.1: Table showing details of seismometer and GPS deployments.

Appendix B

Supplementary information for Chapter 3, Icequake streaks revealed at the base of an Antarctic ice stream.

B.1 Basal icequake detection method: additional details

Basal icequakes are seismic events happening at or near the ice-bed interface. These events are small amplitude, typically have clear P and S waves (Figure 3.1C) and can only be detected within a few km of the seismic source. Beneath the Whillans Ice Plain (WIP), basal icequakes typically occur only during ice plain wide unstable slip events, when ice sliding is fastest. During an unstable slip, hundreds to thousands of basal icequakes can occur within ~30 minutes, with waveforms often overlapping in time and making traditional detection and

association methods challenging. We use an S-wave backprojection technique to detect and preliminarily locate basal icequakes, similar to the method used by *Frank and Shapiro* (2014) to detect tectonic tremor.

Nine short period surface seismometers were operated at the location of the blue triangle shown in Figure 3.1D in January-February 2014 and December 2014, and we analyze data for 21 days in January-February 2014, and 14 days in December 2014. Instruments were arranged in a small network (triangles in Figure 3.2A) near the central nucleation area of WIP unstable slip events (red star, Figure 3.1D) (*Pratt et al.*, 2014). Instruments are less than 1 km apart, allowing small amplitude basal icequake seismic waves to be recorded by multiple instruments. Sercel L22 short period seismometers were leveled and directly buried in the snow ~1 meter below the snow surface in January 2014, and exhumed, re-leveled, and re-buried in December 2014. Three-component seismic data is collected at 1000 Hz and analyzed for 30 and 18 unstable slip events in January and December 2014, respectively.

Seismometer locations are offset between January and December due to downstream ice motion of ~270 m. We determine seismometer locations each year using a handheld GPS unit, with measurements made on different days. To correct for differential downstream advection of seismic sites, all sites are extrapolated upstream to a common time for each year using displacement recorded by a local GPS site (circles in Figure 3.2A). We then assume seismometer locations to be fixed, despite continuous ice displacement (~19 m in January 2014, ~13 m in December 2014), because displacement during the experiment is less than half of the 50 m grid point spacing (discussed below). Some apparent smearing of seismicity into the next upstream grid point is possible but will not affect overall seismicity patterns.

First, we select high quality horizontal component data from 15 minutes before through 60 minutes after the GPS-determined start of each unstable slip event. We then apply a 1Hz high-pass filter and decimate data to 250 Hz (black data, Figure B.1). We next convert the decimated data to short term average over long term average (STA/LTA) data streams (light grey data, Figure B.1) using windows of 0.02 and 0.2 seconds, which were determined to maximize S wave detection and minimize noise detection. The STA/LTA data are further modified by setting all values below 3.2 equal to zero (colored data, Figure B.1). These steps isolate local S-wave arrivals of appropriate duration for basal icequakes (Figure B.1).

We then generate a grid of potential icequake source locations beneath the seismic network at the base of 690 m thick ice, with ice depth determined from the CReSIS radar (*CReSIS*, 2018). Grid point spacing is 50 m, and only gridpoints within 1200 m of a seismometer (in map view) are considered, to ensure that only grid points within a reasonable distance of the network can have basal icequake detections. Grid points are at the center of pixels shown in Figures 3.2, B.3, and B.4, and absolute grid point locations do not change between years.

We calculate S-wave travel times from all grid points to all seismometers using the ObsPy taup module (*Krischer et al.*, 2015) and the ice velocity model shown in Figure B.2. This velocity model is determined using the temperature-velocity relationship of *Kohnen* (1974) applied to a vertical ice temperature profile from a borehole above nearby Subglacial Lake Whillans (SLW) (*Fisher et al.*, 2015). The near-surface S-wave velocity at SLW is estimated from a P-wave velocity profile generated by a seismic refraction survey conducted over SLW in 2010/11 (*Horgan*, 2011) and assuming a Poisson solid. We then vertically scale the SLW velocity model by the relative ice thicknesses of 690 m at the seismic network (*CReSIS*, 2018) and 800m at SLW (*Tulaczyk et al.*, 2014). The resulting S-wave velocity

profile is shown in Figure B.2.

Next, thresholded STA/LTA data are migrated back in time by the travel time for each grid point-seismometer pair, resulting in a set of migrated STA/LTA data streams for each grid point, illustrated in Figure B.1B. Prior to stacking, the migrated STA/LTA data are weighted according to the horizontal distance between each seismometer and grid point. This step is done to reduce the potential mis-association of seismic wave arrivals from disparate parts of the seismic network. STA/LTA streams are weighted by the seismometer-grid point horizontal distance D_{ij} in the following way:

$$W_{ij} = \begin{cases} 1, & D_{ij} \leq d_1 \\ \frac{1}{2}\cos\left[\frac{\pi}{(d_0-d_1)}(D_{ij}-d_1)+1)\right], & d_1 < D_{ij} \leq d_0 \\ 0, & D_{ij} > d_0 \end{cases} \tag{B.1}$$

where W_{ij} is the weighting factor for arrivals from seismometer i to grid point j, d_1 is the distance inside which all weights are 1, and d_0 is the distance beyond which all weights are set to zero. I use $d_1 = 750$ m, and $d_0 = 3250$ m; both are chosen to maximize detections and minimize mis-detections. This weighting scheme ensures that arrivals at seismometers far from a grid point cannot contribute heavily to STA/LTA stacks. Next, thresholded and migrated STA/LTA data at each grid point are stacked. After this step, any peaks in stacked power are probable detections. To determine a detection threshold, the stacked STA/LTA data for all grid points are subset into 20 second (January 2014) or 30 second (December 2014) windows. Within each window, data are further windowed into 0.24 second sub-windows, and two vectors are created for each grid point: the maximum value of the stack in each 0.24 second sub-window (s_{max}), and the power of the stack (sum of squared amplitude) in each 0.24 second sub-window (s_{pow}). An example

"beam" of back-projected power determined for a single 0.24 second sub-window is shown in Figure B.3. Two detection thresholds are then set for each 20 or 30 second window:

$$thresh_1 = \text{mean}(s_{max}) + 6 \times [\text{standard deviation}(s_{max})]\,, and \tag{B.2}$$

$$thresh_2 = \text{mean}(s_{pow}) + 6 \times [\text{standard deviation}(s_{pow})] \tag{B.3}$$

Any 0.24 second window with maximum stack value or power above the corresponding threshold is marked as a detection, provided that 7 or more S-waves contribute to the detection (minimum 4 seismic sites if both horizontal channels are operating). These thresholds keep only the highest quality detections, meaning that many overlapping or smaller icequakes are likely ignored.

The tan area surrounding the seismic network in Figures 3.2 and B.4 indicates grid points that are too far away from the network to offer any sensitivity to a basal icequake happening in that location. The tan area shows grid points that are more than 1200 m from a seismometer, have fewer than 7 possible S wave arrivals total, or fewer than 7 possible arrivals from any seismometer with $W_{ij} > 0.5$. Thus, the white and grey region inside the tan area represents the area of the ice stream bed to which the seismic network is sensitive, though sensitivity does decrease at the edges.

Basal icequakes are detected using this backprojection method on a total of 21 unstable slip events in January-February 2014 and 18 unstable slip events in December 2014. In a typical individual unstable slip event, only a few tens to a few hundreds of basal icequakes are detected, and only at a handful of grid points (Figure B.4). The streaked seismic pattern does not emerge until cumulative seismicity from many unstable slip events is analyzed. Additionally, the seismically

active grid points from one unstable slip event are rarely the same active locations in the next unstable slip. This is illustrated in Figure B.4, showing two consecutive unstable slip events in January 2014 with very different seismicity rates and locations.

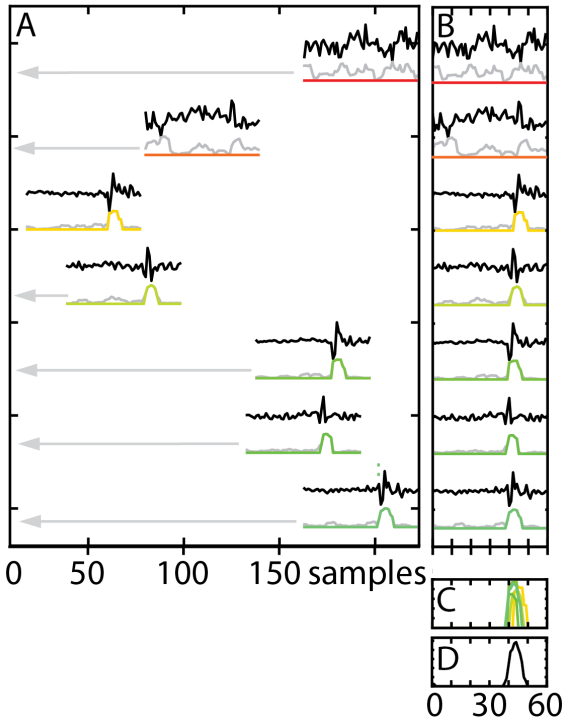

Figure B.1: Example data processing for a single 0.24 second sub-window at a grid point containing a basal icequake. A: 1 Hz high-pass filtered horizontal component seismic data (black) from 7 seismic sites are converted to STA/LTA streams (light grey) and set to zero below an STA/LTA threshold of 3.2 (colored streams). Colors are used to allow distinguishable peaks in panel C but are otherwise not significant. B: STA/LTA data are then migrated backwards in time by the calculated travel time (shown by grey arrows in A) to the source grid point, where the peaks in STA/LTA line up. STA/LTA data are then weighted according to the horizontal distance between the seismometer and the grid point. C: Migrated and weighted STA/LTA data. D: Stacked STA/LTA data from all sites, showing a coherent peak. Data from 7 additional channels that contributed to this detection are omitted for clarity.

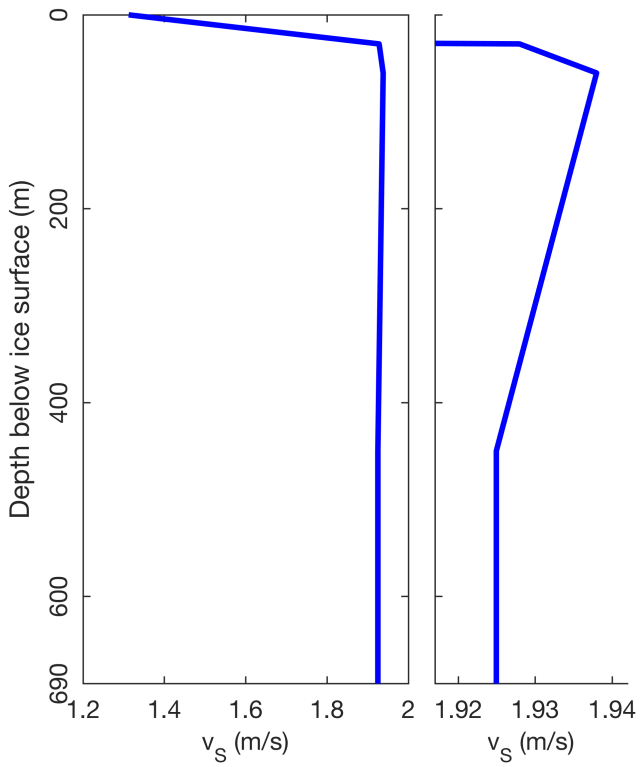

Figure B.2: Ice S-wave velocity model used in backprojection. Right panel is a zoom of the right-hand-side of left panel.

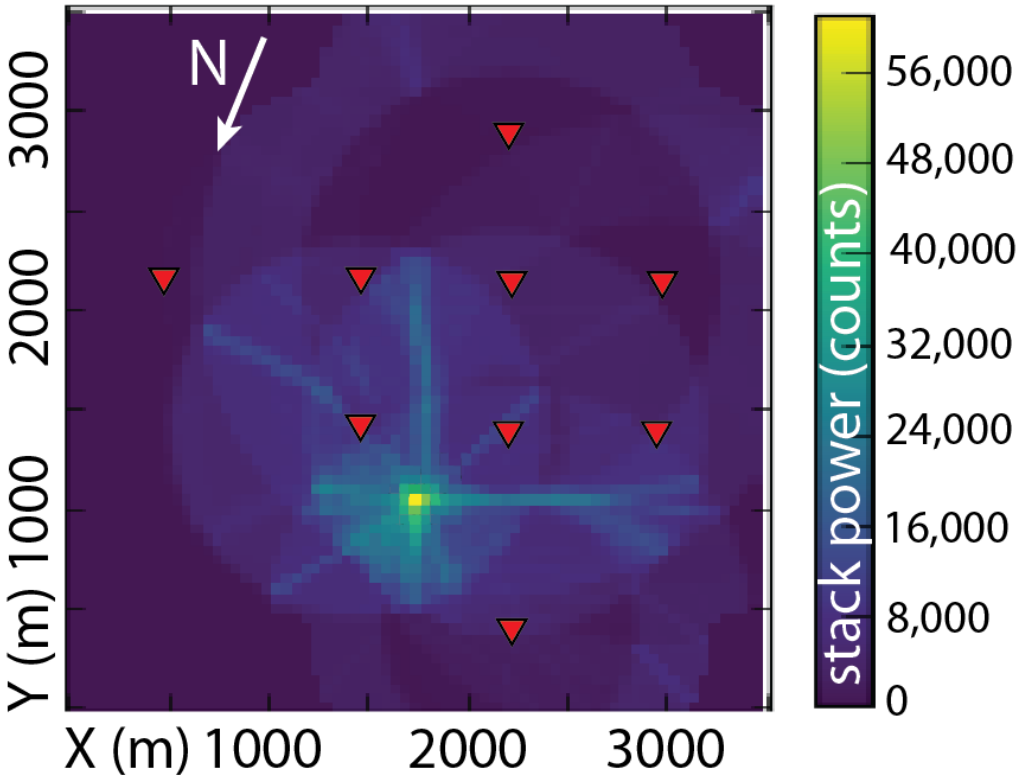

Figure B.3: An example "beam" generated for a single 0.24 second sub-window containing a basal icequake. Red triangles are seismometer locations in January 2014, and grid point color is the power (sum of squared amplitude) of the stacked STA/LTA data (Figure B.1D) at each grid point. The yellow grid point is where the stacked power is greatest for this 0.24 second sub-window and is the best location for this basal icequake. X- and Y-axes are in polar stereographic projection with origin at PS X = -229,500 and PS Y = -557,570 m.

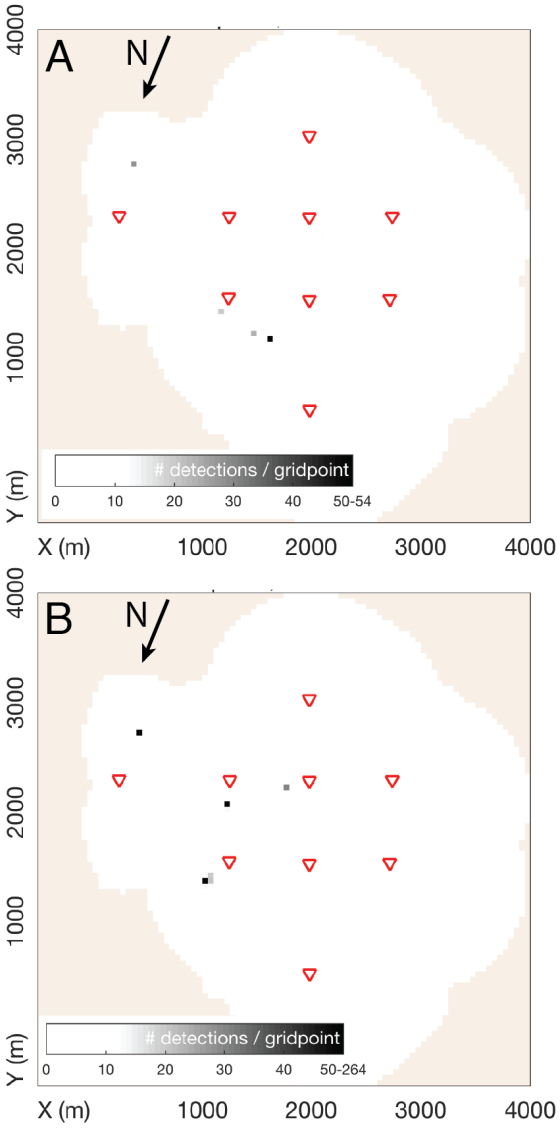

Figure B.4: Number of icequakes detected per grid point by backprojection during two consecutive unstable slip events. A: Unstable slip event beginning Jan 8, 2014 16:30. B: Unstable slip event beginning Jan 9, 2014 08:55. Both: Red triangles are seismometer locations in January 2014. Grid point color is the number of basal icequakes detected at that grid point for each unstable slip event. Grid point color is saturated at 50 basal earthquakes detected per gridpoint to highlight that basal icequakes only happen in a few locations beneath the seismic network in each unstable slip event. Note sparsity of detections. Tan represents the area outside of the detection field, in which no basal icequakes can be detected because too few horizontal channels are available to trigger a detection. X- and Y-axes are in polar stereographic projection with origin at PS X = -229,500 and PS Y = -557,570 m.

Bibliography

Abercrombie, R. E. (1995), Earthquake source scaling relationships from -1 to 5 ML using seismograms recorded at 2.5-km depth, *Journal of Geophysical Research: Solid Earth*, *100*(B12), 24,015–24,036, doi: 10.1029/95JB02397.

Adalgeirsdottir, G., A. M. Smith, T. Murray, M. A. King, K. Makinson, K. W. Nicholls, and A. E. Behar (2008), Tidal influence on Rutford Ice Stream , West Antarctica: observations of surface flow and basal processes from closely spaced GPS and passive seismic stations, *Journal of Glaciology*, *54*(187), 715–724.

Aki, K., and P. G. Richards (2002), *Quantitative Seismology*, University Science Books, Sausalito, CA.

Alley, R. B. (1993), In search of ice-stream sticky spots, *Journal of Glaciology*, *39*(133), 447–454.

Alley, R. B., D. D. Blankenship, C. R. Bentley, and S. T. Rooney (1986), Deformation of till beneath ice stream B, West Antarctica, *Nature*, *322*(3), 57–59.

Anandakrishnan, S., and R. Alley (1994), Ice Stream C, Antarctica, sticky spots detected by microearthquake monitoring, *Annals of Glaciology*, *20*, 183–186.

Anandakrishnan, S., and R. B. Alley (1997a), Stagnation of Ice Stream C, West Antarctica by water piracy, *Geophysical Research Letters*, *24*(3), 265–268, doi: 10.1029/96GL04016.

Anandakrishnan, S., and R. B. Alley (1997b), Tidal forcing of basal seismicity of ice stream C, West Antarctica, observed far inland, *Journal of Geophysical Research*, *102*(B7), 15,183–15,196.

Anandakrishnan, S., and C. R. Bentley (1993), Micro-earthquakes beneath Ice Streams Band C, West Antarctica: observations and implications, *Journal of Glaciology*, *39*(133), 455–462.

Atre, S. R., and C. R. Bentley (1993), Laterally varying basal conditions beneath Ice Streams B and C, West Antarctica, *Journal of Glaciology*, *39*(133), 507–514.

Atre, S. R., and C. R. Bentley (1994), Indication of a dilatant bed near Downstream B Camp, Ice Stream B, Antarctica, *Annals of Glaciology*, *20*, 177–182.

Barcheck, C. G., S. Tulaczyk, S. Y. Schwartz, J. I. Walter, and J. P. Winberry (2018), Implications of basal micro-earthquakes and tremor for ice stream mechanics : Stick-slip basal sliding and till erosion, *Earth and Planetary Science Letters*, *486*, 54–60, doi: 10.1016/j.epsl.2017.12.046.

Beem, L. H., S. M. Tulaczyk, M. A. King, M. Bougamont, H. A. Fricker, and P. Christoffersen (2014), Variable deceleration of Whillans Ice Stream, West Antarctica, *Journal of Geophysical Research: Earth Surface*, *119*, 212–224, doi: 10.1002/2013JF002958.

Bennett, M. R. (2003), Ice streams as the arteries of an ice sheet: their mechanics, stability and significance, *Earth-Science Reviews*, *61*, 309–339, doi: 10.1016/S0012-8252(02)00130-7.

Beyreuther, M., R. Barsch, L. Krischer, T. Megies, Y. Behr, and J. Wassermann (2010), ObsPy: A Python Toolbox for Seismology, *Seismological Research Letters*, *81*(3), 530–533, doi: 10.1785/gssrl.81.3.530.

Bindschadler, R., M. King, R. Alley, S. Anandakrishnan, and L. Padman (2003), Tidally controlled stick-slip discharge of a West Antarctic ice stream, *Science*, *301*(5636), 1087–1089.

Bindschadler, R., P. Vornberger, and L. Gray (2005), Changes in the ice plain of Whillans Ice Stream, West Antarctica, *Journal Of Glaciology*, *51*(175), 620–636.

Bindschadler, R., H. Choi, A. Wichlacz, R. Bingham, J. Bohlander, K. Brunt, H. Corr, R. Drews, H. Fricker, M. Hall, R. Hindmarsh, J. Kohler, L. Padman, W. Rack, G. Rotschky, S. Urbini, P. Vornberger, and N. Young (2011), Getting around Antarctica: New high-resolution mappings of the grounded and freely-floating boundaries of the Antarctic ice sheet created for the International Polar Year, *Cryosphere*, *5*, 569–588, doi: 10.5194/tc-5-569-2011.

Bindschadler, R. A., S. N. Stephenson, D. R. MacAyeal, and S. Shabtaie (1987), Ice Dynamics at the Mouth of Ice Stream B , Antarctica, *Journal of Geophysical Research*, *92*(B9), 8885–8894.

Blankenship, D. D., C. R. Bentley, S. T. Rooney, and R. B. Alley (1986), Seismic measurements reveal a saturated porous layer beneath an active Antarctic ice stream, *Nature*, *322*, 54–57.

Blankenship, D. D., S. Anandakrishnan, J. L. Kempf, and C. R. Bentley (1987), Microearthquakes under and alongside ice stream B, Antarctica, detected by a new passive seismic array, *Annals of Glaciology*, *9*, 30–34.

Boulton, G. S., and C. D. Clarke (1990), A highly mobile Laurentide ice sheet revealed by satellite images of glacial lineations, *Nature*, *346*, 813–816.

Brune, J. N. (1970), Tectonic stress and the spectra of seismic shear waves from earthquakes, *Journal of Geophysical Research*, *75*(26), 4997–5009.

Chamberlain, C. J., C. M. Boese, and J. Townend (2017), Cross-correlation-based detection and characterisation of microseismicity adjacent to the locked, late-interseismic Alpine Fault, South Westland, New Zealand, *Earth and Planetary Science Letters*, *457*, 63–72, doi: 10.1016/j.epsl.2016.09.061.

Chen, K. H., R. Bürgmann, R. M. Nadeau, T. Chen, and N. Lapusta (2010), Postseismic variations in seismic moment and recurrence interval of repeating earthquakes, *Earth and Planetary Science Letters*, *299*, 118–125, doi: 10.1016/j.epsl.2010.08.027.

Chen, T., and N. Lapusta (2009), Scaling of small repeating earthquakes explained by interaction of seismic and aseismic slip in a rate and state fault model, *Journal of Geophysical Research: Solid Earth*, *114*(B01311), doi: 10.1029/2008JB005749.

CReSIS (2018), 2013_Antarctica_Basler Data, Lawrence, Kansas, USA. Digital Media. http://data.cresis.ku.edu/.

Cuffey, K., and W. S. B. Paterson (2010), *The Physics of Glaciers*, 4th ed., Elsevier, Amsterdam, Netherlands.

Eshelby, J. D. (1957), The determination of the elastic field of an ellipsoidal inclusion, and related problems, *Proceedings of the Royal Society of London, Series A.*, *241*, 376–396.

Eyles, N., N. Putkinen, S. Sookhan, and L. Arbelaez-Moreno (2016), Erosional origin of drumlins and megaridges, *Sedimentary Geology*, *338*, 2–23, doi: 10.1016/j.sedgeo.2016.01.006.

Fisher, A. T., K. D. Mankoff, S. M. Tulaczyk, S. W. Tyler, N. Foley, and WISSARD (2015), High geothermal heat flux measured below the West Antarctic Ice Sheet, *Science Advances*, *1*(6), doi: 10.1126/sciadv.1500093.

Frank, W. B., and N. M. Shapiro (2014), Automatic detection of low-frequency earthquakes (LFEs) based on a beamformed network response, *Geophysical Journal International*, *197*(2), 1215–1223, doi: 10.1093/gji/ggu058.

Fretwell, P., H. D. Pritchard, D. G. Vaughan, J. L. Bamber, N. E. Barrand, R. Bell, C. Bianchi, R. G. Bingham, D. D. Blankenship, G. Casassa, G. Catania, D. Callens, H. Conway, a. J. Cook, H. F. J. Corr, D. Damaske, V. Damm, F. Ferraccioli, R. Forsberg, S. Fujita, Y. Gim, P. Gogineni, J. a. Griggs, R. C. a. Hindmarsh, P. Holmlund, J. W. Holt, R. W. Jacobel, a. Jenkins, W. Jokat, T. Jordan, E. C. King, J. Kohler, W. Krabill, M. Riger-Kusk, K. a. Langley, G. Leitchenkov, C. Leuschen, B. P. Luyendyk, K. Matsuoka, J. Mouginot, F. O. Nitsche, Y. Nogi, O. a. Nost, S. V. Popov, E. Rignot, D. M. Rippin, a. Rivera, J. Roberts, N. Ross, M. J. Siegert, a. M. Smith, D. Steinhage, M. Studinger, B. Sun, B. K. Tinto, B. C. Welch, D. Wilson, D. a. Young, C. Xiangbin, and a. Zirizzotti (2013), Bedmap2: Improved ice bed, surface and thickness datasets for Antarctica, *Cryosphere*, *7*, 375–393, doi: 10.5194/tc-7-375-2013.

Fricker, H. A., and T. Scambos (2009), Connected subglacial lake activity on lower Mercer and Whillans Ice Streams, West Antarctica, 2003-2008, *Journal of Glaciology*, *55*(190), 303–315, doi: 10.3189/002214309788608813.

Ghosh, A., J. E. Vidale, J. R. Sweet, K. C. Creager, A. G. Wech, H. Houston, and E. E. Brodsky (2010), Rapid, continuous streaking of tremor in Cascadia, *Geochemistry, Geophysics, Geosystems*, *11*(12), doi: 10.1029/2010GC003305.

Greene, C. A., D. E. Gwyther, and D. D. Blankenship (2017), Antarctic Mapping Tools for MATLAB, *Computers and Geosciences*, *104*, 151–157, doi: 10.1016/j.cageo.2016.08.003.

Halberstadt, A. R. W., L. M. Simkins, S. L. Greenwood, and J. B. Anderson (2016), Past ice-sheet behaviour: retreat scenarios and changing controls in the Ross Sea, Antarctica, *The Cryosphere*, *10*, 1003–1020, doi: 10.5194/tc-10-1003-2016.

Hanks, T. C., and H. Kanamori (1979), A moment magnitude scale, *Journal of Geophysical Research*, *84*(B5), 2348–2350, doi: 10.1029/JB084iB05p02348.

Harland, S., J.-M. Kendall, G. Stuart, G. Lloyd, a.F. Baird, a.M. Smith, H. Pritchard, and a.M. Brisbourne (2013), Deformation in Rutford Ice Stream, West Antarctica: measuring shear-wave anisotropy from icequakes, *Annals of Glaciology*, *54*(64), 105–114, doi: 10.3189/2013AoG64A033.

Herring, T. A., R. W. King, M. A. Floyd, and S. C. Mcclusky (2015), GAMIT Reference Manual: GPS Analysis at MIT, Release 10.6, 16 July, 2015.

Hodson, T. O., R. D. Powell, S. A. Brachfeld, S. Tulaczyk, R. P. Scherer, and W. S. Team (2016), Physical processes in Subglacial Lake Whillans, West Antarctica: Inferences from sediment cores, *Earth and Planetary Science Letters*, *444*, 56–63, doi: 10.1016/j.epsl.2016.03.036.

Horgan, H. J. (2011), Firn and ice thickness at Subglacial Lake Whillans, *Tech. rep.*

Igarashi, T., T. Matsuzawa, and A. Hasegawa (2003), Repeating earthquakes and interplate aseismic slip in the northeastern Japan subduction zone, *Journal of Geophysical Research: Solid Earth*, *108*(B5, 2449), doi: 10.1029/2002JB001920.

Ikari, M. J., C. Marone, D. M. Saffer, and A. J. Kopf (2013), Slip weakening as a mechanism for slow earthquakes, *Nature Geoscience*, *6*, 468–472, doi: 10.1038/ngeo1818.

Ito, Y., and M. J. Ikari (2015), Velocity- and slip-dependent weakening in simulated fault gouge: Implications for multimode fault slip, *Geophysical Research Letters*, *42*, 9247–9254, doi: 10.1002/2015GL065829.

Iverson, N. R. (2010), Shear resistance and continuity of subglacial till : hydrology rules, *Journal of Glaciology*, *56*(200), 1104–1114.

Iverson, N. R., and L. K. Zoet (2015), Experiments on the dynamics and sedimentary products of glacier slip, *Geomorphology*, *244*, 121–134, doi: 10.1016/j.geomorph.2015.03.027.

Iverson, N. R., T. S. Hoover, and R. W. Baker (1998), Ring-shear studies of till deformation: Coulomb-plastic behavior and distributed strain in glacier beds, *Journal of Glaciology*, *44*(148), 634–642.

Jeffreys, M., and K. Been (2015), *Soil Liquefaction: A Critical State Approach*, 2nd ed., CRC Press, Boca Raton, FL.

Joughin, I., S. Tulaczyk, R. Bindschadler, and S. F. Price (2002), Changes in west Antarctic ice stream velocities: Observation and analysis, *Journal of Geophysical Research*, *107*(B11), doi: 10.1029/2001JB001029.

Joughin, I., S. Tulaczyk, D. R. MacAyeal, and H. Engelhardt (2004), Melting and freezing beneath the Ross ice streams, Antarctica, *Journal of Glaciology*, *50*(168), 96–108, doi: 10.3189/172756504781830295.

Joughin, I., R. A. Bindschadler, M. A. King, D. Voigt, R. B. Alley, S. Anandakrishnan, H. Horgan, L. Peters, P. Winberry, S. B. Das, and G. Catania (2005), Continued deceleration of Whillans Ice Stream, West Antarctica, *Geophysical Research Letters*, *32*(L22501), doi: 10.1029/2005GL024319.

Joughin, I. R., S. Tulaczyk, and H. F. Engelhardt (2003), Basal melt beneath Whillans Ice Stream and Ice Streams A and C, West Antarctica, *Annals of Glaciology*, *36*, 257–262.

Kamb, B. (1991), Rheological nonlinearity and flow instability in the deforming bed mechanism of ice stream motion, *Journal of Geophysical Research*, *96*(B10), 16,585–16,595, doi: 10.1029/91JB00946.

Kamb, B. (2001), Basal zone of the West Antarctic ice streams and its role in lubrication of their rapid motion, in *The West Antarctic Ice Sheet, behavior and environment: American Geophysical Union Antarctic Research Series Volume 77,*, edited by R. Alley and R. Bindschadler, pp. 157–199.

King, E. C., R. C. A. Hindmarsh, and C. R. Stokes (2009), Formation of mega-scale glacial lineations observed beneath a West Antarctic ice stream, *Nature Geoscience*, *2*, 585–588, doi: 10.1038/ngeo581.

Kohnen, H. (1974), The Temperature Dependence of Seismic Waves in Ice, *Journal of Glaciology*, *13*(67), 144–147.

Krischer, L., T. Megies, R. Barsch, M. Beyreuther, T. Lecocq, C. Caudron, and J. Wassermann (2015), ObsPy: A bridge for seismology into the scientific Python ecosystem, *Computational Science and Discovery*, *8*, doi: 10.1088/1749-4699/8/1/014003.

Larson, K. M., A. R. Lowry, V. Kostoglodov, W. Hutton, O. Sánchez, K. Hudnut, and G. Suárez (2004), Crustal deformation measurements in Guerrero , Mexico, *Journal of Geophysical Research*, *109*(B04409), doi: 10.1029/2003JB002843.

Lipovsky, B. P., and E. M. Dunham (2016), Tremor during ice-stream stick slip, *The Cryosphere*, *10*, 385–399, doi: 10.5194/tc-10-385-2016.

Lipovsky, B. P., and E. M. Dunham (2017), Slow-slip events on the Whillans Ice Plain, Antarctica, described using rate-and-state friction as an ice stream sliding law, *Journal of Geophysical Research: Earth Surface*, *122*(4), 973–1003, doi: 10.1002/2016JF004183.

Luthra, T., S. Anandakrishnan, J. P. Winberry, R. B. Alley, and N. Holschuh (2016), Basal characteristics of the main sticky spot on the ice plain of Whillans Ice Stream, Antarctica, *Earth and Planetary Science Letters*, *440*, 12–19, doi: 10.1016/j.epsl.2016.01.035.

Madariaga, R. (1976), Dynamics of an expanding circular fault, *Bulletin of the Seismological Society of America*, *66*(3), 639–666.

Marone, C., J. E. Vidale, and W. L. Ellsworth (1995), Fault healing inferred from time dependent variations in source properties of repeating earthquakes, *Geophysical Research Letters*, *22*(22), 3095–3098.

Matoza, R. S., P. M. Shearer, G. Lin, C. J. Wolfe, and P. G. Okubo (2013), Systematic relocation of seismicity on Hawaii Island from 1992 to 2009 using waveform cross correlation and cluster analysis, *Journal of Geophysical Research: Solid Earth*, *118*, 2275–2288, doi: 10.1002/jgrb.50189.

Matsuzawa, T., N. Uchida, T. Igarashi, T. Okada, and A. Hasegawa (2004), Repeating earthquakes and quasi-static slip on the plate boundary east off northern Honshu, Japan, *Earth, Planets and Space*, *56*, 803–811.

Mclaskey, G. C., A. M. Thomas, S. D. Glaser, and R. M. Nadeau (2012), Fault healing promotes high-frequency earthquakes in laboratory experiments and on natural faults, *Nature*, *491*, 101–104, doi: 10.1038/nature11512.

Megies, T., M. Beyreuther, R. Barsch, L. Krischer, and J. Wassermann (2011), ObsPy - What can it do for data centers and observatories?, *Annals of Geophysics*, *54*(1), 47–58, doi: 10.4401/ag-4838.

Meyer, C. R., A. S. Downey, and A. W. Rempel (2018), Freeze-on limits bed strength beneath sliding glaciers, *Nature Communications*, *9*, doi: 10.1038/s41467-018-05716-1.

Moore, P. L., and N. R. Iverson (2002), Slow episodic shear of granular materials regulated by dilatant strengthening, *Geology*, *30*(9), 843–846, doi: 10.1130/0091-7613(2002)030<0843:SESOGM>2.0.CO;2.

Nadeau, R. M., and L. R. Johnson (1998), Seismological Studies at Parkfield VI: Moment Release Rates and Estimates of Source Parameters for Small Repeating Earthquakes, *Bulletin of the Seismological Society of America*, *88*(3), 790–814.

Nadeau, R. M., and T. V. McEvilly (2004), Periodic Pulsing of Characteristic Microearthquakes on the San Andreas Fault, *Science*, *303*, 220–223.

Obara, K., and Y. Ito (2005), Very low frequency earthquakes excited by the 2004 off the Kii peninsula earthquakes: A dynamic deformation process in the large accretionary prism, *Earth, Planets and Space*, *57*, 321–326, doi: 10.1186/BF03352570.

Okada, T., T. Matsuzawa, and A. Hasegawa (2003), Comparison of source areas of M4.8 +/- 0.1 repeating earthquakes off Kamaishi, NE Japan: are asperities persistent features?, *Earth and Planetary Science Letters*, *213*, 361–374, doi: 10.1016/S0012-821X(03)00299-1.

Peng, Z., J. E. Vidale, C. Marone, and A. Rubin (2005), Systematic variations in recurrence interval and moment of repeating aftershocks, *Geophysical Research Letters*, *32*(L15301), doi: 10.1029/2005GL022626.

Podolskiy, E. A., and F. Walter (2016), Cryoseismology, *Reviews of Geophysics*, *54*, 708–758, doi: 10.1002/2016RG000526.

Pratt, M. J., J. P. Winberry, D. A. Wiens, S. Anandakrishnan, and R. B. Alley (2014), Seismic and geodetic evidence for grounding-line control of Whillans Ice Stream stick-slip events, *Journal of Geophysical Research: Earth Surface*, *119*, 333–348, doi: 10.1002/2013JF002842.

Rathbun, A. P., C. Marone, R. B. Alley, and S. Anandakrishnan (2008), Laboratory study of the frictional rheology of sheared till, *Journal of Geophysical Research*, *113*(F2), F02,020, doi: 10.1029/2007JF000815.

Retzlaff, R., and C. R. Bentley (1993), Timing of stagnation of Ice Stream C , West Antarctica , from short-pulse radar studies of buried surface crevasses, *Journal of Glaciology*, *39*(133), 553–561.

Roeoesli, C., A. Helmstetter, F. Walter, and E. Kissling (2016), Meltwater influences on deep stick-slip icequakes near the base of the Greenland Ice Sheet, *Journal of Geophysical Research: Earth Surface*, *121*, 223–240, doi: 10.1002/2015JF003601.

Rooney, S. T., D. D. Blankenship, R. B. Alley, and C. R. Bentley (1987), Till Beneath Ice Stream B 2. Structure and Continuity, *Journal of Geophysical Research*, *92*(B9), 8913–8920.

Rubin, A. M., D. Gillard, and J. L. Got (1999), Streaks of microearthquakes along creeping faults, *Nature*, *400*, 635–641, doi: 10.1038/23196.

Schaff, D. P., G. C. Beroza, and B. E. Shaw (1998), Postseismic response of repeating aftershocks, *Geophysical Research Letters*, *25*(24), 4549–4552.

Scholz, C. H. (1998), Earthquakes and friction laws, *Nature*, *391*, 37–42.

Scholz, C. H. (2002), *The Mechanics of Earthquakes and Faulting*, 2nd ed., Cambridge University Press, Cambridge, United Kingdom.

Siegfried, M. R., H. A. Fricker, S. P. Carter, and S. Tulaczyk (2016), Episodic ice velocity fluctuations triggered by a subglacial flood in West Antarctica, *Geophysical Research Letters*, *43*, 2640–2648, doi: 10.1002/2016GL067758.

Smith, A. (2006), Microearthquakes and subglacial conditions, *Geophysical research letters*, *33*(24), L24,501, doi: 10.1029/2006GL028207.

Smith, A., T. Murray, K. Nicholls, K. Makinson, G. Adalgeirsdóttir, A. Behar, and D. Vaughan (2007), Rapid erosion, drumlin formation, and changing hydrology beneath an Antarctic ice stream, *Geology*, *35*(2), 127–130, doi: 10.1130/G23036A.1.

Smith, A. M. (1997), Basal conditions on Rutford Ice Stream, West Antarctica, from seismic observations, *Journal of Geophysical Research*, *102*(B1), 543–552.

Smith, A. M., and T. Murray (2009), Bedform topography and basal conditions beneath a fast-flowing West Antarctic ice stream, *Quaternary Science Reviews*, *28*, 584–596, doi: 10.1016/j.quascirev.2008.05.010.

Smith, E. C., A. M. Smith, R. S. White, A. M. Brisbourne, and H. D. Pritchard (2015), Mapping the ice-bed interface characteristics of Rutford Ice Stream, West Antarctica, using microseismicity, *Journal of Geophysical Research: Earth Surface*, *120*, 1881–1894, doi: 10.1002/2015JF003587.

Smith, E. C., A. F. Baird, J. M. Kendall, C. Martín, R. S. White, A. M. Brisbourne, and A. M. Smith (2017), Ice fabric in an Antarctic ice stream interpreted from seismic anisotropy, *Geophysical Research Letters*, *44*(8), 3710–3718, doi: 10.1002/2016GL072093.

Spagnolo, M., C. D. Clark, J. C. Ely, C. R. Stokes, J. B. Anderson, K. Andreassen, A. G. Graham, and E. C. King (2014), Size, shape and spatial arrangement of mega-scale glacial lineations from a large and diverse dataset, *Earth Surface Processes and Landforms*, *39*, 1432–1448, doi: 10.1002/esp.3532.

Stokes, C. R. (2018), Geomorphology under ice streams : Moving from form to process, *Earth Surface Processes and Landforms*, *43*, 85–123, doi: 10.1002/esp.4259.

Stokes, C. R., C. D. Clark, O. B. Lian, and S. Tulaczyk (2007), Ice stream sticky spots: a review of their identification and influence beneath contemporary and palaeo-ice streams., *Earth-Science Reviews*, *81*, 217–249.

Taira, T.-a., R. Bürgmann, R. M. Nadeau, and D. S. Dreger (2014), Variability of fault slip behavior along the San Andreas Fault in the San Juan Bautista Region, *Journal of Geophysical Research: Solid Earth*, *119*, 8827–8844, doi: 10.1002/2014JB011427.

Thomason, J. F., and N. R. Iverson (2008), A laboratory study of particle ploughing and pore-pressure feedback: a velocity-weakening mechanism for soft glacier beds, *Journal of Glaciology*, *54*(184), 169–181, doi: 10.3189/002214308784409008.

Tulaczyk, S., B. Kamb, and H. Engelhardt (2000), Basal mechanics of Ice Stream B, west Antarctica: 1. Till mechanics, *Journal of Geophysical Research*, *105*(B1), 463–481.

Tulaczyk, S., B. Kamb, and H. F. Engelhardt (2001), Estimates of effective stress beneath a modern West Antarctic ice stream from till preconsolidation and void ratio, *Boreas*, *30*(2), 101–114, doi: 10.1111/j.1502-3885.2001.tb01216.x.

Tulaczyk, S., J. a. Mikucki, M. R. Siegfried, J. C. Priscu, C. G. Barcheck, L. H. Beem, A. Behar, J. Burnett, B. C. Christner, A. T. Fisher, H. a. Fricker, K. D. Mankoff, R. D. Powell, F. Rack, D. Sampson, R. P. Scherer, and S. Y. Schwartz (2014), WISSARD at Subglacial Lake Whillans, West Antarctica: scientific operations and initial observations, *Annals of Glaciology*, *55*(65), 51–58, doi: 10.3189/2014AoG65A009.

Turner, R. C., M. Shirzaei, R. M. Nadeau, and R. Bürgmann (2015), Slow and Go: Pulsing slip rates on the creeping section of the San Andreas Fault, *Journal of Geophysical Research: Solid Earth*, *120*, 5940–5951, doi: 10.1002/2015JB011998.

Uchida, N., T. Matsuzawa, A. Hasegawa, and T. Igarashi (2003), Interplate quasi-static slip off Sanriku, NE Japan, estimated from repeating earthquakes, *Geophysical Research Letters*, *30*(15), doi: 10.1029/2003GL017452.

Vidale, J. E., W. L. Elisworth, A. Cole, and C. Marone (1994), Variations in rupture process with recurrence interval in a repeated small earthquake, *Nature*, *368*, 624–626, doi: 10.1038/368624a0.

Waldhauser, F., and W. L. Ellsworth (2000), A Double-Difference Earthquake Location Algorithm: Method and Application to the Northern Hayward Fault, California, *Bulletin of the Seismological Society of America*, *90*(6), 1353–1368.

Waldhauser, F., and W. L. Ellsworth (2002), Fault structure and mechanics of the Hayward Fault, California, from double-difference earthquake locations, *Journal of Geophysical Research*, *107*(B3,2054), doi: 10.1029/2000JB000084.

Waldhauser, F., W. L. Ellsworth, D. P. Schaff, and A. Cole (2004), Streaks, multiplets, and holes: High-resolution spatio-temporal behavior of Parkfield seismicity, *Geophysical Research Letters*, *31*(L18608), doi: 10.1029/2004GL020649.

Walter, F., J. F. Clinton, N. Deichmann, D. S. Dreger, S. E. Minson, and M. Funk (2009), Moment Tensor Inversions of Icequakes on Gornergletscher , Switzerland, *Bulletin of the Seismological Society of America*, *99*(2A), 852–870, doi: 10.1785/0120080110.

Walter, J. I., E. E. Brodsky, S. Tulaczyk, S. Y. Schwartz, and R. Pettersson (2011), Transient slip events from near-field seismic and geodetic data on a glacier fault, Whillans Ice Plain, West Antarctica, *Journal of Geophysical Research*, *116*(F01021), doi: 10.1029/2010JF001754.

Walter, J. I., S. Y. Schwartz, M. Protti, and V. Gonzalez (2013), The synchronous occurrence of shallow tremor and very low frequency earthquakes offshore of the Nicoya Peninsula, Costa Rica, *Geophysical Research Letters*, *40*, 1517–1522, doi: doi:10.1002/grl.50213.

Walter, J. I., I. Svetlizky, J. Fineberg, E. E. Brodsky, S. Tulaczyk, C. G. Barcheck, and S. P. Carter (2015), Rupture speed dependence on initial stress profiles: Insights from glacier and laboratory stick-slip, *Earth and Planetary Science Letters*, *411*, 112–120, doi: 10.1016/j.epsl.2014.11.025.

Whillans, I. M., C. R. Bentley, and C. J. V. D. Veen (2001), Ice Streams B and C, *The West Antarctic Ice Sheet: Behavior and Environment, in Antarctic Research Series*, *77*, 257–281.

Wiens, D. a., S. Anandakrishnan, J. P. Winberry, and M. a. King (2008), Simultaneous teleseismic and geodetic observations of the stick-slip motion of an Antarctic ice stream., *Nature*, *453*(7196), 770–4, doi: 10.1038/nature06990.

Winberry, J., S. Anandakrishnan, and R. Alley (2009a), Seismic observations of transient subglacial water-flow beneath MacAyeal Ice Stream, west Antarctica, *Geophys. Res. Lett*, *36*(11), doi: 10.1029/2009GL037730.

Winberry, J. P., S. Anandakrishnan, R. B. Alley, R. A. Bindschadler, and M. A. King (2009b), Basal mechanics of ice streams: Insights from the stick-slip motion of Whillans Ice Stream, West Antarctica, *Journal of Geophysical Research*, *114*(F01016), doi: 10.1029/2008JF001035.

Winberry, J. P., S. Anandakrishnan, D. a. Wiens, R. B. Alley, and K. Christianson (2011), Dynamics of stick-slip motion, Whillans Ice Stream, Antarctica, *Earth and Planetary Science Letters*, *305*(3-4), 283–289, doi: 10.1016/j.epsl.2011.02.052.

Winberry, J. P., S. Anandakrishnan, D. A. Wiens, and R. B. Alley (2013), Nucleation and seismic tremor associated with the glacial earthquakes of Whillans Ice Stream, Antarctica, *Geophysical Research Letters*, *40*, 312–315, doi: 10.1002/grl.50130.

Winberry, J. P., S. Anandakrishnan, R. B. Alley, D. a. Wiens, and M. J. Pratt (2014), Tidal pacing, skipped slips and the slowdown of Whillans Ice Stream, Antarctica, *Journal of Glaciology*, *60*(222), 795–807, doi: 10.3189/2014JoG14J038.

Zoet, L. K., and N. R. Iverson (2018), A healing mechanism for stick-slip of glaciers, *Geology*, *46*(9), 807–810, doi: 10.1130/G45099.1.

Zoet, L. K., S. Anandakrishnan, R. B. Alley, A. a. Nyblade, and D. a. Wiens (2012), Motion of an Antarctic glacier by repeated tidally modulated earthquakes, *Nature Geoscience*, *5*(9), 623–626, doi: 10.1038/ngeo1555.

Zoet, L. K., R. B. Alley, S. Anandakrishnan, and K. Christianson (2013a), Accelerated subglacial erosion in response to stick-slip motion, *Geology*, *41*(2), 159–162, doi: 10.1130/G33624.1.

Zoet, L. K., B. Carpenter, M. Scuderi, R. B. Alley, S. Anandakrishnan, C. Marone, and M. Jackson (2013b), The effects of entrained debris on the basal sliding stability of a glacier, *Journal of Geophysical Research: Earth Surface*, *118*, 656–666, doi: 10.1002/jgrf.20052.

Zumberge, J. F., M. B. Heftin, D. C. Jefferson, M. M. Watkins, and F. H. Webb (1997), Precise point positioning for the efficient and robust analysis of GPS data from large networks, *Journal of Geophysical Research*, *102*(B3), 5005–5017.